# Chapter 1

# Introduction

## 1.1 Motivation

GPS consists of 27 satellites (24 operational satellites and 3 active spares). These satellites are distributed over 6 orbit planes separated by $60°$ with an inclination of $55°$. The period of the GPS satellite to travel around the earth is near 12 hours with an altitude of about 20200 km. Each GPS is equipped with the high-accuracy atomic clock. GPS signals derived from the fundamental frequency ($f_0$=10.23MHz) of satellite's oscillator include the code and carrier phase, which are mainly used for positioning. Two carrier phases are modulated with the codes and navigation messages to L1 ($f_1$= 1575.42 MHz, $\lambda_1$=19.05 cm) and L2 ($f_2$= 1227.60 MHz, $\lambda_2$= 24.45 cm). Over the past decade, GPS has been widely used for the positioning of moving objects, including LEO. Since the TOPEX/Poseidon altimeter mission, GPS has been used for attitude determination, time-synchronization, and orbit determination of LEOs. One of well-known receivers, BlackJack, is widely used in the geodetic study (Wu et al. 2005; Schreiner, 2005; Montenbruck et al. 2006). The BlackJack receiver was developed by JPL and was used in the CHAMP and GRACE satellite missions.

F3/C (Fong et al. 2008) is a joint Taiwan-US satellite mission lunched on April 15, 2006, and deployed 6 micro-satellites at altitudes ranging from 750 to 800 km and at an inclination of 72° in the final mission phase. The expected lifetime is 5 years. The acronym COSMIC stands for Constellation Observing System for Meteorology, Ionosphere and Climate and hereafter, F3/C will be used to represent FORMOSAT-3/COSMIC. Each satellite was equipped with the BlackJack GPS receiver for collecting the high accuracy GPS data and it was installed with four

antennas on the front and back faces of the satellite main frame (Fig. 1-1). Two signal-patch antennas for POD were mounted on the upper part of the main body and the other two antennas for atmospheric occultation research were mounted on the lower part. A more detailed information of GPS payload for F3/C can be found in Wu et al. (2005).

A F3/C special issue of Terrestrial, Atmospheric and Oceanic Sciences (Lee et al. 2000) documents the scientific objectives and anticipated results of F3/C. Useful information about the status and data acquisition is available on the web site of Taiwan's NSPO: http://www.nspo.org.tw/2005e/projects/project3/research.htm. The earliest research on the geodetic applications of F3/C using GPS data was given by Švehla and Rothacher (2006).
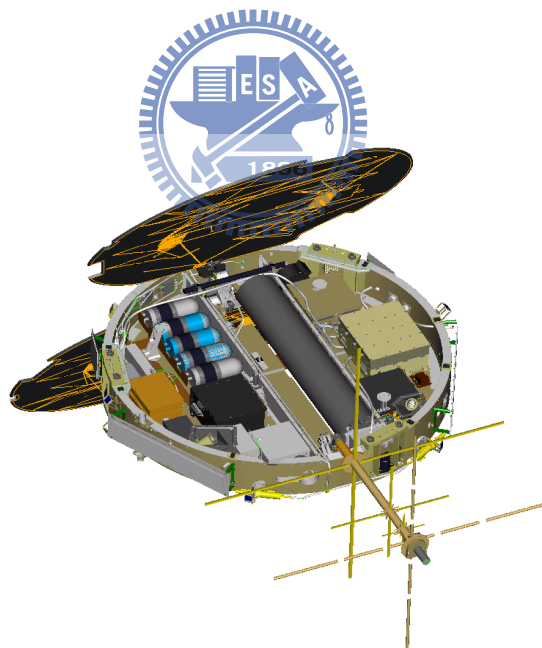


Fig. 1-1: F3/C spacecraft

## 1.2 Review of recent LEO missions

## 1.2.1 CHAMP satellite mission

CHAMP, launched on July 15, 2000, is a German satellite mission for the scientific applications, e.g., the determination of the earth gravity field and geomagnetic field (Reigber, et al. 1996). The altitude of CHAMP is about 500 km and the orbit with an inclination of $87°$ is nearly circular. CHAMP is equipped with a BlackJack receiver for tracking GPS satellites and a star camera for attitude control, as well as an accelerometer for measuring the non-gravitational effects, such as air drag, solar radiation pressure and the earth albedo radiation. Fig. 1-2 shows CHAMP satellite body and the POD antenna is mounted on the zenith direction of the main body. The accelerometer is helpful to generate the dynamic orbit of CHAMP for the earth gravity recovery without modeling any non-conservative force. Fig. 1-3 and 1-4 show the gravity anomaly and geoid from the EIGEN-CHAMP03S model. EIGEN-CHAMP03S is a CHAMP-only gravity field model derived from a homogeneous reprocessing of all normal equations including the improved parameterization of the accelerometer data.

Aside from above mentioned scientific instruments, CHAMP was also equipped with a laser retro-reflector for SLR, which can be used for an independent validation of POD result. However, F3/C satellites do not have a SLR reflector. A more detailed information of CHAMP mission can be found at http://op.gfz-potsdam.de/champ/index_CHAMP.html.

Fig. 1-2: CHAMP satellite body (http://www.pcrf.org/images/champ2a.jpg)
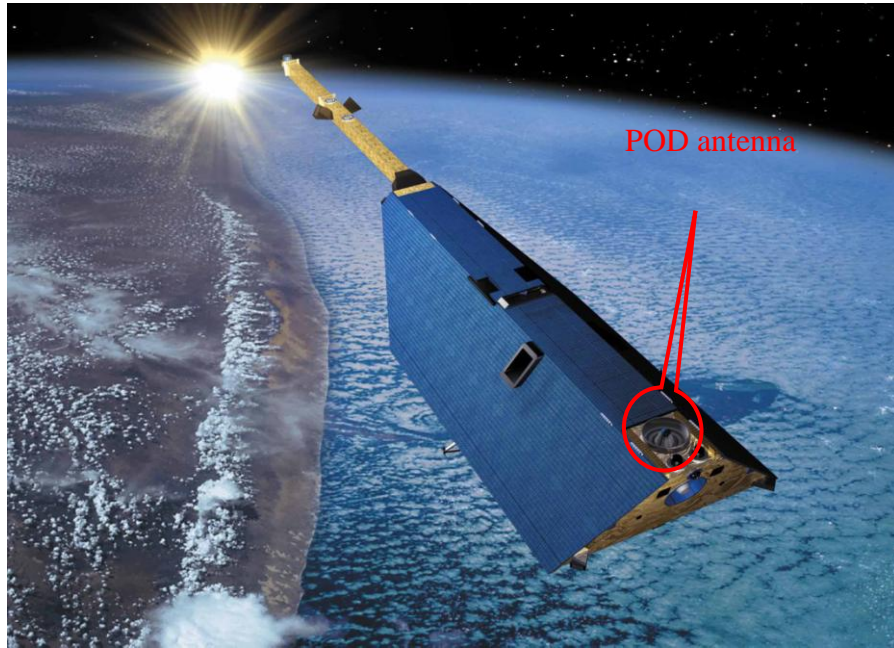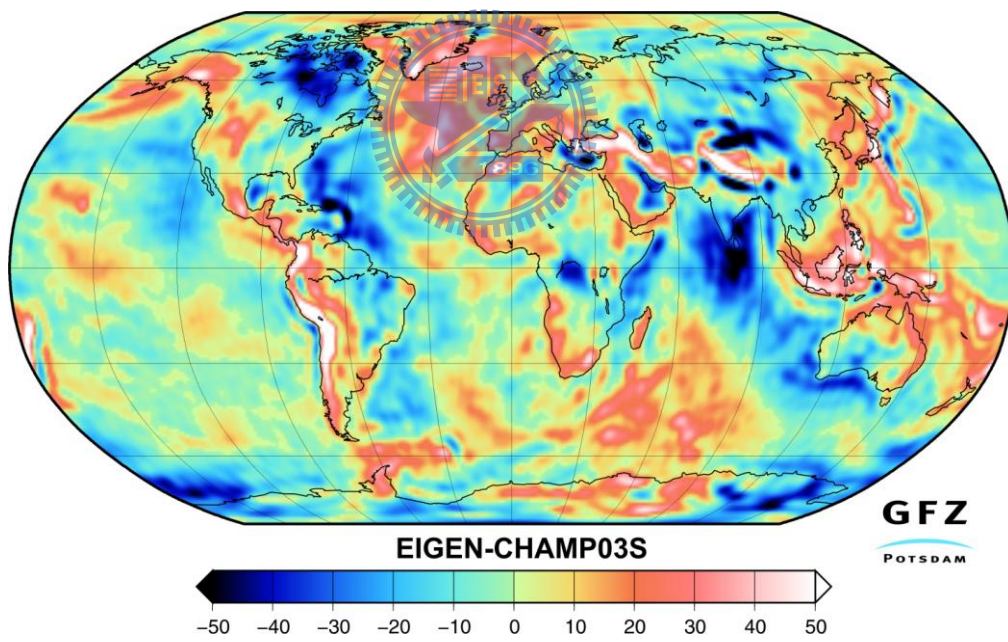


Fig. 1-3: EIGEN-CHAMP03S Gravity Anomalies in mgal
(http://op.gfz-potsdam.de/champ/index_CHAMP.html)
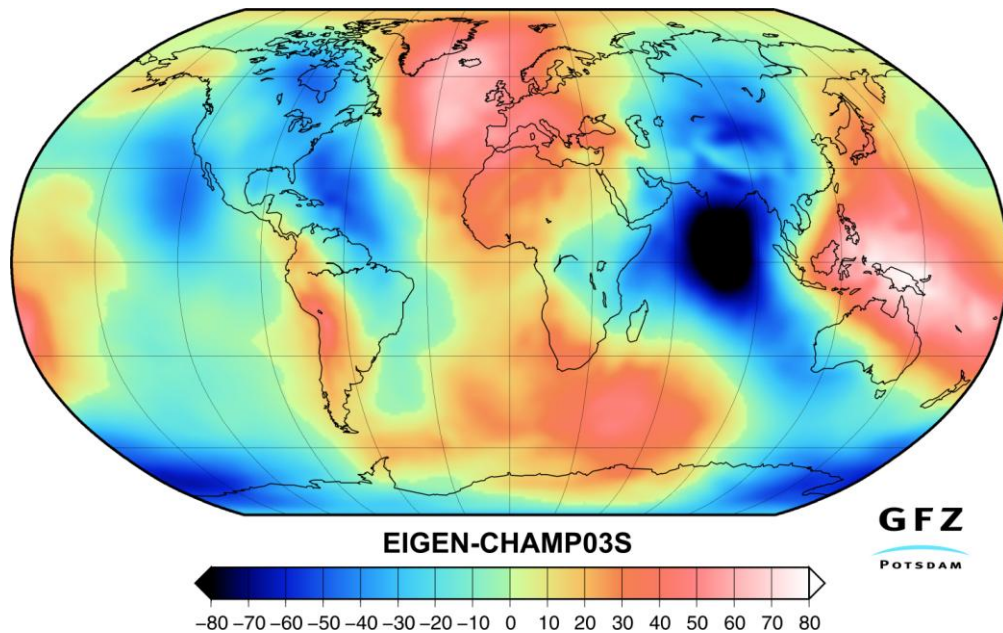
Fig. 1-4: EIGEN-CHAMP03S Geoid in meter
(http://op.gfz-potsdam.de/champ/index_CHAMP.html)

**1.2.2 GRACE satellite mission**

GRACE satellite mission was launched on March 17, 2002. GRACE mission consists of two satellites deployed at a height of approximately 500 km with an inclination of $89°$. The distance between two separated satellites is about 220 km, which is precisely measured by the KBR system with an accuracy of 10 μm at 1Hz data sampling rate. Scientific instruments equipped in GRACE satellites are nearly the same as those in CHAMP satellite, except for KBR. Fig. 1-5 shows GRACE satellite body and the POD antenna is mounted on the zenith direction of the main body. The main goal of GRACE mission is to observe time-varying gravity fields, with a higher accuracy than that derived by CHAMP. Fig. 1-6 and 1-7 show gravity anomaly and geoid from GRACE KBR measurements over 110 days. A more detailed information of GRACE mission can be found at http://www-app2.gfz-potsdam.de/pb1/op/grace/results/index_RESULTS.html .
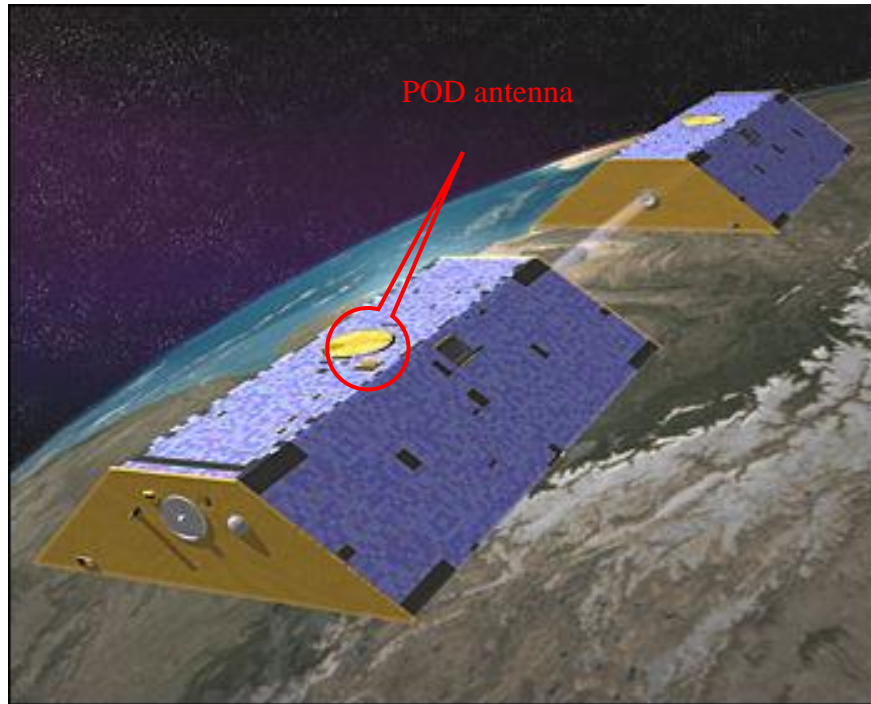
Fig. 1-5: GRACE satellite body

(http://earthobservatory.nasa.gov/Features/ESE/Images/grace_satellite.jpg)
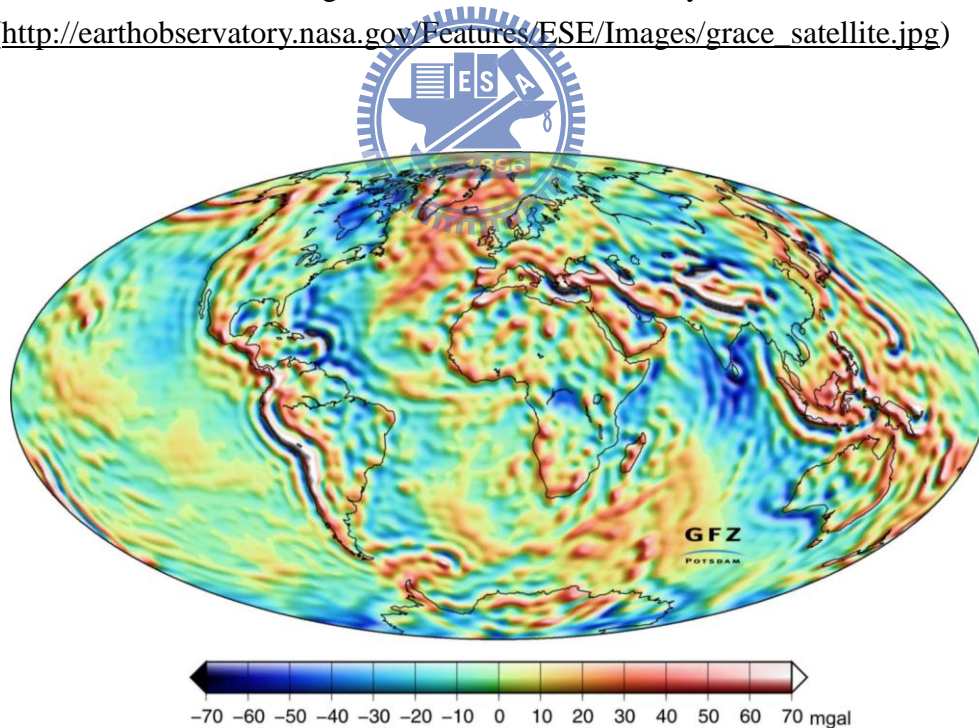


Fig. 1-6: EIGEN-GRACE02S Gravity Anomalies

(http://www-app2.gfz-potsdam.de/pb1/op/grace/results/index_RESULTS.html)
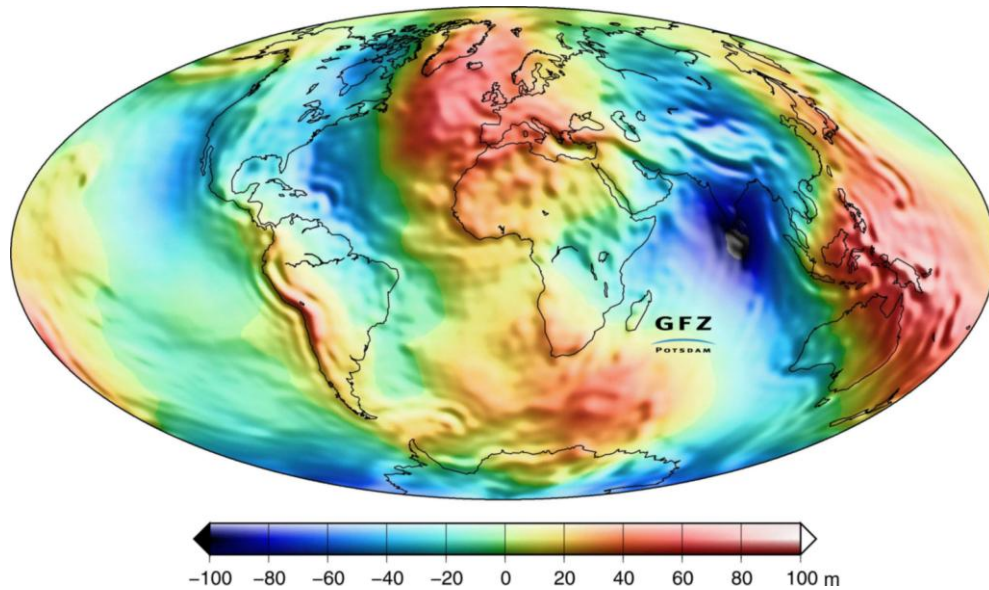
Fig. 1-7: EIGEN-GRACE02S Geoid model
(http://www-app2.gfz-potsdam.de/pb1/op/grace/results/index_RESULTS.html)

### 1.2.3 GOCE satellite mission

GOCE was developed by ESA and was launched on March 17, 2009. GOCE is deployed at an orbit of 250 km with an inclination of $96.7°$. The scientific objective of GOCE mission is to determine the earth gravity field with an extremely high accuracy and spatial resolution. GOCE was equipped with a POD GPS antenna for the precise positioning and a 3-axis gradiometer for measuring the tiny variation of the earth gravity field. Fig. 1-8 shows GOCE satellite body, and the POD antenna is mounted on the zenith direction of the main body. Earlier studies of GOCE based on simulated data can be found in Visser and Van den IJssel (2000) and Bock et al, (2007).

Fig. 1-8: GOCE satellite body (http://esamultimedia.esa.int/docs/BR209web.pdf)
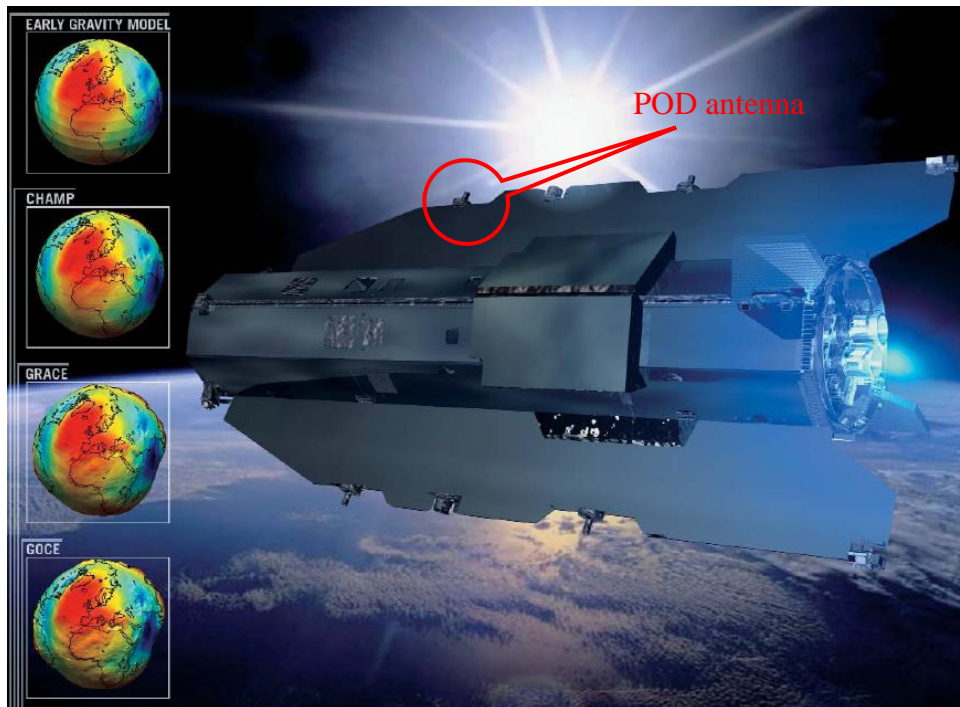
Note that the POD antennas mounted in the zenith direction of CHAMP, GRACE and GOCE are to prevent the GPS POD data from multipath and excessive ionospheric delay. On the other hand, the patch antennas of F3/C potentially will result in large noises and systematic errors in GPS phase data, because the two solar panels may (1) deflect the GPS signals and (2) block some of the GPS signals. Additionally, the orbit accuracy at a centimeter level for the above satellite missions can be used for a potential application of the earth gravity field recovery. The use of kinematic orbits of a LEO satellite for gravity field determination was demonstrated for the first time by Gerlach et al. (2003). Parallel to this, several alternative methods were developed, e.g.: Reubelt et al. (2004), Mayer-Gürr et al. (2005), and Ditmar et al. (2006).

## 1.3 Literature Review

The reduced dynamic method and the kinematic method (Švehla and Rothacher 2003; Jäggi et al. 2006 and 2007; Hwang et al. 2009) are implemented in the software Bernese version 5.0 (Dach et al. 2007). Hwang et al. (2009) demonstrated that six F3/C satellite orbits were determined with a proper data selection and processing, and an accuracy of 2-3 cm was achieved using the overlap analysis. Precise orbits of F3/C satellites can be used in many applications. For instance, the kinematic orbits can be regarded as three-dimensional ranging data to recover the long wavelength temporal variation of the earth gravity field (Hwang et al. 2008). Chao et al. (2000) and Hwang (2001) showed that GPS-derived kinematic orbits of F3/C can be used to recover the earth's static and temporal gravity fields.

The gravity signatures from a combined F3/C-GRACE gravity solution were enhanced over those from the GRACE-only solution. However, the percentage of usable kinematic orbits of F3/C for gravity determination can be as low as 30% (Hwang et al. 2008). This suggests that a relatively large portion of F3/C GPS data (both code and phase) are degraded by such factors as multipath effects, cycle slips, excessive IOD and low number of visible GPS satellites that typically contribute to a poor positioning accuracy (Leick 2004).

In general, the orbit accuracy is associated with the quality of F3/C GPS data, which is inversely proportional to the magnitudes of multipath effects, IODs and the residuals of GPS observables. However, a large multipath and IOD might result in a cycle slip, which can be an indicator of GPS data quality. Furthermore, phase residuals are associated with the satellite orbit determination and can be used to detect outliers in the data processing. Subsequently, phase residuals can be used to compute the a posteriori unit weight deviation. Such deviation also serves as an alternative indicator of the GPS data quality and an overall fitness of the stochastic and

mathematical model in orbit determination.

Several F3/C studies are given by Hwang et al. (2008, 2009, 2010) and in the special issue of IEEE Transactions on Geoscience and Remote Sensing (Volume 46 2008). The objective of this study is to use F3/C GPS data to assess the achievable orbit accuracy and GPS data quality, and to quantify attitude error. The quality assessment in this study was based on F3/C data and GRACE data (for comparison) and the outputs in connection to satellite orbit determination. Due to the large amount of F3/C orbital data, selected epochs and selected F3/C satellites will be used to show problems and solutions in the POD experiment. For convenience, FM1-FM6 will be used to present the six F3/C satellites, following the convention of NSPO.

## 1.4 Outline of Thesis

Chapter 2 shortly reviews the GPS observables used in this essay, such as the ionosphere-free linear combination, geometry-free linear combination and the multipath equation. Such equations are used for the orbit determination and the assessment of GPS data quality.

Chapter 3 focuses on the description of the structure and payload of F3/C satellite body and discusses about the effects of satellite body, satellite center of mass and variation, phase center offset and variation of antenna, and cable delay on orbit determination.

Chapter 4 uses the linear combination of GPS observables mentioned in Chapter 2 to assess GPS data quality and compares the data quality of F3/C with GRACE satellite.

Chapter 5 describes the definition and principle of attitude control system for F3/C mission in a various space environments. An analysis of attitude control system is given in the end of Chapter 5.

Chapter 6 focuses on the introduction of reduced-dynamic and kinematic strategies and the assessment of F3/C orbit quality.

Chapter 7 analyzes the quantification of attitude error based on orbit determination. The GPS-derived baselines between POD antenna phase center and satellite's center of mass are compared with those given by NSPO. Such differences reflect attitude error and positioning accuracy.

The conclusions, future work and suggestions are presented in the final Chapter.
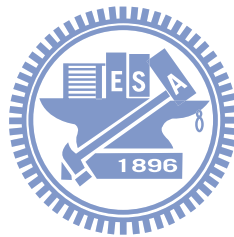
# Chapter 2

# GPS observables for orbit determination

## 2.1 Observation types

### 2.1.1 Code pseudorange

A pseudorange observation between the GPS and the receiver is measured by GPS PRN code. The oscillator of a GPS receiver will internally generate a duplicate signal to analogously compare with a raw one from a GPS until the highest correlation is achieved. As a result, the time shift between the receiver and the GPS can be estimated. Meanwhile, the ionospheric delay, clock errors, hardware delays, multipath and noise effects are taken into account. Thus, the code pseudorange observation of LEO satellite can be expressed as (Leick 2004)

$$P_{k,i}^{p} = \rho_{k}^{p} - cdt_{k} + cdt^{p} + I_{k,i,P}^{p} + \delta_{k,i,P}^{p} + \varepsilon_{i,P} \tag{2.1}$$
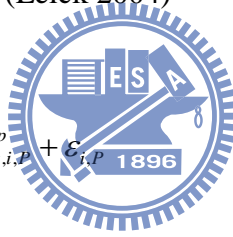
with

$$\rho_{k}^{p} = \sqrt{(x^{p} - x_{k})^{2} + (y^{p} - y_{k})^{2} + (z^{p} - z_{k})} \tag{2.2}$$

$\rho_{k}^{p}$ : Geometry distance from the coordinate of GPS satellite $p$ to the coordinate of the receiver $k$

$P_{k,i}^{p}$ : Code pseudorange on Li (i=1,2)

$I_{k,i,P}^{p}$ : P-code Ionospheric delay at Li (i=1,2).

$t_{k}$ : The time in the receiver clock at the epoch that the code entered the antenna and

the receiver clock error is $dt_k$

$t^p$: The time in the satellite clock at the epoch that the code transmitted from the antenna and the satellite clock error is $dt^p$

$\delta^p_{k,i,P}$: Hardware delay (i=1,2)

$\varepsilon_{i,P}$: Pseudorange measurement noise, including the multipath (i=1,2)

Eq. (2.1) is a general form, but it does not take into account all effects. The relativistic effect between GPS clock and receiver clock is not involved in Eq. (2.1), since such effect for LEO satellite is relatively small as compared to GPS satellite. However, such effect will be absorbed by the receiver clock correction estimated in the procedure of the least square adjustment (Bock 2003). Furthermore, the ionosphere-free linear combination of P code (see Eq. (2.7)) is used to determine a priori orbit and detect outliers in the POD procedure. Table 2-1 shows the RMS (root mean square) of the difference between reduced-dynamic and kinematic orbits (see Chapter 6) for FM1 in year 2008 using raw and smoothed code observations in the earth-fixed frame. Table 2-1 addresses that no large discrepancy in orbit solutions using raw and smoothed codes. Note that the poor solution of the finial orbit determination is not influenced by a priori orbit from poor code solution, even the use of the smoothed code solution with a measuring accuracy of decimeter. That is because the quality of the final orbit solution only depends on the quality of GPS phase observations. Here, smoothed code measurements take the mean of 'code minus phase' measurements. Additionally, the raw GPS code measurement is replaced by the corresponding phase measurement shifted by such mean difference. Meanwhile, the ionospheric delay is taken into account in the procedure of creating the smoothed code observation. That is so-called the smoothed code (Dach et al. 2007).

Table 2-1: RMS of the differences between reduced-dynamic and kinematic orbits
using raw and smoothed code observations in the earth-fixed frame

|              | X (cm) | Y (cm) | Z (cm) |
|--------------|--------|--------|--------|
| Raw code     | 5.97   | 5.62   | 5.87   |
| Smooth code  | 5.80   | 5.60   | 5.92   |

### 2.1.2 Phase pseudorange

For the high-accuracy requirement in geodesy, most GPS receivers provide GPS carrier phase to precisely measure the distance between GPS satellite and receiver. In unit of cycles, the equation for the carrier phase can be written as (Leick 2004)

$$\varphi_{k,i}^p = \frac{f_i}{c}\rho_k^p - f_i dt_k + f_i dt^p + I_{k,i,\varphi}^p + \delta_{k,i,\varphi}^p + N_{k,i}^p + m_{i,\varphi} \tag{2.3}$$

$\varphi_{k,i}^p$ : Phase pseudorange (i =1,2)

$N_k^p$ : Integer ambiguity of Li (i =1,2)

$I_{k,i,\varphi}^p$ : Ionospheric Li carrier phase advance (i=1,2).

$\delta_{k,i,\varphi}^p$ : Hardware delay (i=1,2)

$m_{i,\varphi}$ : Li phase measurement noise, including the multipath (i=1,2)

The carrier phase can be scaled to unit of length by multiplying with $\lambda_1 = \frac{c}{f_1}$ . Thus, (2.4) becomes

$$\Phi_{k,i}^p = \rho_k^p - cdt_k + cdt^p + I_{k,i,\varphi}^p + \delta_{k,i,\varphi}^p + \lambda_i N_{k,i}^p + m_{i,\varphi} \tag{2.4}$$

Eq. (2.4) differs from Eq. (2.1) because introducing the high-accuracy GPS carrier phase and the unknown integer ambiguity. Additionally, the ionosphere distributes about from the height 50 km to 1000 km above the earth surface and is filled with ionized particles and plasmas resulting in the refraction of GPS signal. However, the refracted signal depends on the frequency of the microwave emitted from GPS. Thus, when GPS signal propagates through the ionosphere, the effects of TEC for phase and code observations can be expressed as below (Leick 2004)

$$\Delta_{ph}^{Iono} = -\frac{40.3}{f^2}\text{TEC} \qquad \Delta_{c}^{Iono} = \frac{40.3}{f^2}\text{TEC} \qquad (2.5)$$

where $\Delta_{ph}^{Iono}$ is for carrier phase advance and $\Delta_{c}^{Iono}$ is for code delay. It is difficult to model the TEC due to the various time dependent environments. Furthermore, since the velocity of LEO is about 7 km/s resulting in the rapid variation of the ionosphere, the best method to eliminate the ionospheric delay is to use the linear combination of two different frequencies (see the following section). The ambiguity parameter in Eq. (2.4) is the only non-epoch parameter. For handling the ambiguity term, Bock (2003) demonstrated that an alternative PPP approach was based on forming the relative difference between two successive phase observations in order to eliminate the ambiguity and a priori orbit from the code solution was introduced as an absolute position.

Additionally, Švehla and Rothacher (2005b) demonstrated that LEO orbit solutions from the double-difference observations formed between ground IGS stations and the LEO satellite were not significantly improved. The time of tracking a GPS arc in a LEO and a ground IGS station is different. For a ground station, the arc

lasts several hours to track a GPS satellite, but for a LEO satellite, the arc may lasts 15-25 minutes. Thus, if the double-difference observations are involved into the LEO orbit determination, a large number of ambiguity parameters must be solved and very long baselines (LEO - IGS station) will be estimated. As a result, PPP can be an efficient strategy to determine LEO orbit by means of introducing the GPS orbit and HRC products (Bock 2003).

## 2.2 Linear combination of observations

### 2.2.1 Ionosphere-free linear combination

In order to eliminate the ionosphere effect the ionosphere-free linear combination is used in this study, as expressed (Dach et al. 2007)

$$L_C^3 = \frac{1}{f_1^2 - f_2^2}\left(f_1^2 L1 - f_2^2 L2\right) \tag{2.6}$$
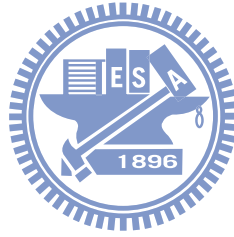
$$P_C^3 = \frac{1}{f_1^2 - f_2^2}\left(f_1^2 P1 - f_2^2 P2\right) \tag{2.7}$$

where $L_C^3$ and $P_C^3$ is the so-called ionosphere-free linear combination for the phase and code, respectively. When the same propagating path of both phase and code observations with respect to the same GPS satellite is considered, the same effect can be eliminated by forming $P_C^3 - L_C^3$, except for multipath (see the following section). Additionally, the phase multipath can be ignored because the value is relatively small as compared to code multipath. Hence, the $P_C^3 - L_C^3$ value presents the performance of multipath effect (Hofmann-Wellenhof et al. 2001). Moreover, the user-specified RMS value of $P_C^3 - L_C^3$ in Bernese will be served as a threshold of the outlier

detection with respect to each tracked GPS arc.

**2.2.2 Geometry-free linear combination**

    The geometry-free linear combination can be expressed as (Dach et al. 2007)

$$L_C^4 = L1 - L2 \qquad\qquad (2.8)$$

Eq. (2.8) eliminates the receiver clock error, GPS satellite clock error and the geometry distance. Only the ionospheric delay and the initial ambiguity are remained in Eq. (2.8), which may be used for the estimation of the ionosphere model. In the study, this linear combination is used to observe the conduct of excessive phase data and to detect cycle slips or outliers in the GPS data analysis (see Chapter 4).

**2.2.3 Multipath equation**

    Multipath effect is caused by non line-of-sight (between the GPS satellite and the LEO receiver) GPS signal propagation (Hofmann-Wellenhof et al. 2001; Leick 2004). This effect can be estimated by using the combination of code and phase measurements based on the same influence of clock errors, the tropospheric delay and the relativistic effect during the tracking period. Eq. (2.1) and (2.4) are used to form Pi-Li (i=1, 2). The multipath equations for pseudorange P1 (MP1) and P2 (MP2) can be expressed as (Estey and Meertens, 1999)

$$MP1 = \varepsilon_{1,P} - (1 + \frac{2}{\alpha-1})N_1\lambda_1 + (\frac{2}{\alpha-1})N_2\lambda_2 - (1 + \frac{2}{\alpha-1})m_1 + (\frac{2}{\alpha-1})m_2 \qquad (2.9)$$

$$MP2 = \varepsilon_{2,P} - (\frac{2\alpha}{\alpha - 1})N_1\lambda_1 + (\frac{2\alpha}{\alpha - 1} - 1)N_2\lambda_2 - (\frac{2\alpha}{\alpha - 1})m_1 + (\frac{2\alpha}{\alpha - 1} - 1)m_2 \qquad (2.10)$$

where $\alpha$ is ratio between the squared frequencies of L1 and L2, i.e., $f_1^2 / f_2^2$. The maximum multipath on phase is about 1/4 of the wavelength and the noise level of phase is about 0.2 to 5 mm (Comp and Axelrad 1998; Hofmann-Wellenhof et al. 2001, p. 92), so these values are relatively small as compared to code multipath and noise. As such, the phase multipath and noise are ignored when estimating MP1 and MP2 with Eqs. (2.9) and (2.10). If the P1 is not available, the C/A code will be used instead (Estey and Meertens 1999).
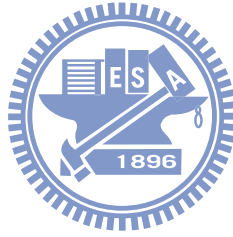
# Chapter 3

# The F3/C spacecrafts and GPS payloads

## 3.1 Spacecraft geometry

Fig. 3-1 shows the geometry and dimension of a F3/C satellite. The mass of each F3/C satellite is 62 kg with a full propellant and the origin of the spacecraft coordinate frame is the same as the geometric center of the ring. Each of F3/C satellites is equipped with a GOX receiver, a TIP built by NRL and a TBB, also provided by NRL. The purpose of TIP is to monitor the ionospheric electron density with an operating wavelength of 135.6 nm (Coker et al. 2002), while TBB is used for studies of tomography and ionospheric scintillation. A more detailed description of the TIP and TBB can be found in Syndergaard et al. (2006).

The GOX GPS receiver, BlackJack (IGOR version) is designed by JPL and manufactured by BRE. The IGOR receiver was experienced in F3/C mission for the first time. It can simultaneously process GPS signals from two POD antennas and two occultation antennas. 24 individual channels of the receiver are allocated to 4 antennas, of which 12 channels are allocated to two patch POD antennas and the others are allocated to two occultation antennas. A more detailed description of the IGOR receiver can be found in Montenbruck et al. (2006). Table 3-1 shows the coordinates of the two POD antenna centers of F3/C satellites in the spacecraft coordinate frame. The coordinates for the F3/C satellites differ from a few mm. Table 3-2 shows the boresight vector of the two POD antennas in the spacecraft frame. The boresight vector points toward the zenith direction of POD antennas and is helpful to realize the relative orientation between LEO and tracked GPS satellites. The angle between the line of coordinate origin-physical center of POD antenna and the +X or -X axis is about $30°$. The angle between the normal to the POD antenna and the X

axis is about 15° (Fig. 3-2(a)). This design also enables ionospheric occultation sounding using the two POD antennas. For comparison, the GPS antenna of GRACE (http://www.csr.utexas.edu/grace/) is mounted 0.45 m above the COM along the radial direction (Fig. 3-2(b)), and it will view more GPS satellites than any one of the two antennas of a F3/C satellite and is less affected by the multipath effect as well as the ionospheric delay.
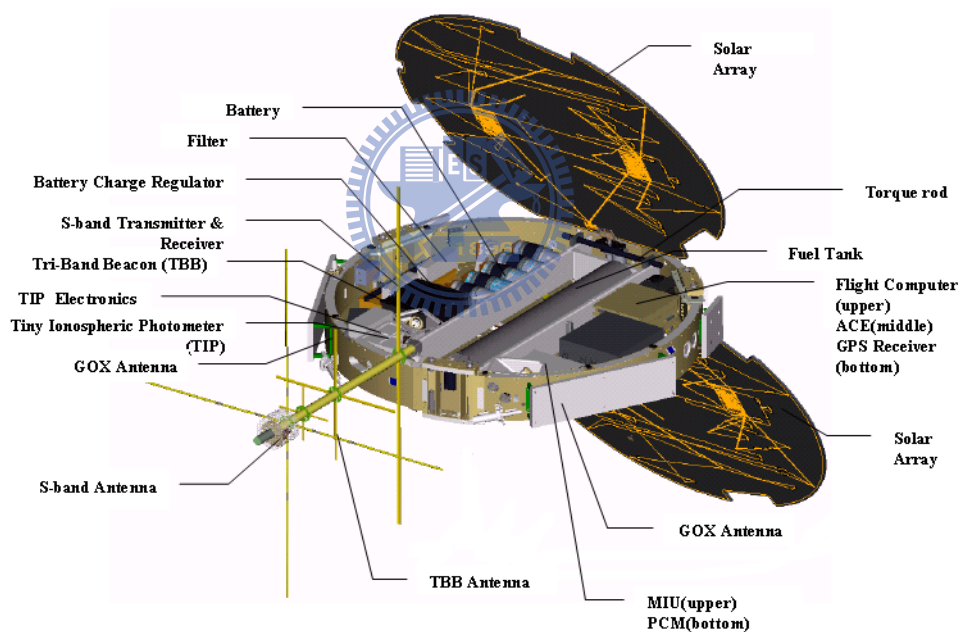


Fig. 3-1: F3/C spacecraft and its payloads

Table 3-1: Coordinates of the two POD antennas (in m) in the spacecraft coordinate frame for F3/C

| Coordinates | POD +X (x/y/z) | POD –X (x/y/z) |
|---|---|---|
| FM1 | 0.468/0.005/-0.257 | -0.474/0.005/-0.261 |
| FM2 | 0.469/0.005/-0.256 | -0.474/0.005/-0.260 |
| FM3 | 0.468/0.005/-0.255 | -0.474/0.004/-0.260 |
| FM4 | 0.468/0.005/-0.255 | -0.475/0.005/-0.260 |
| FM5 | 0.468/0.005/-0.256 | -0.475/0.005/-0.260 |
| FM6 | 0.468/0.004/-0.256 | -0.474/0.005/-0.261 |

Table 3-2: Boresight vector of the two POD antennas (in m) in the spacecraft coordinate frame for F3/C

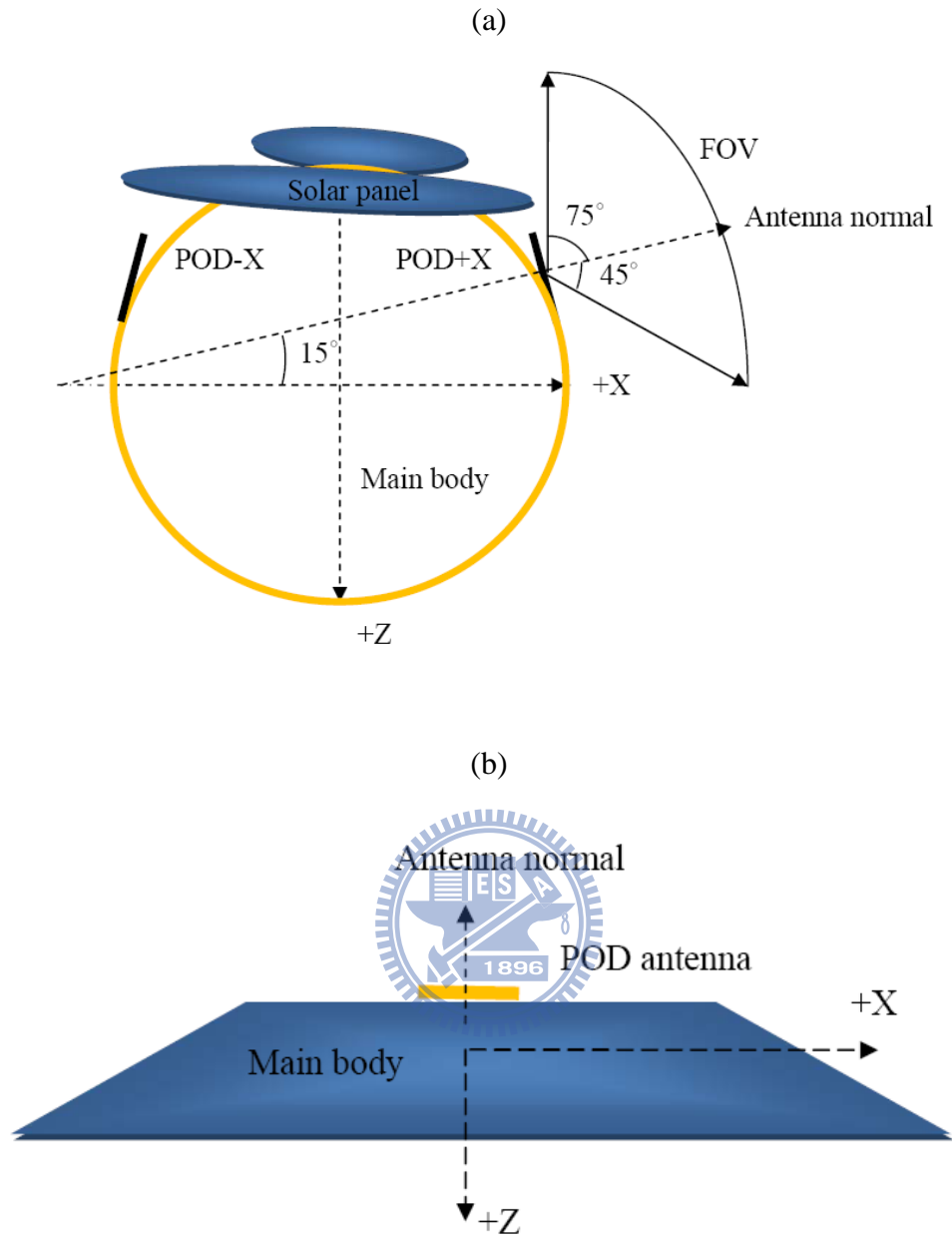| Coordinates | POD +X (x/y/z) | POD –X (x/y/z) |
|---|---|---|
| FM1 | 0.9666/0.0000/-0.2561 | -0.9652/0.0000/-0.2615 |
| FM2 | 0.9721/0.0000/-0.2346 | -0.9590/0.0000/-0.2833 |
| FM3 | 0.9669/0.0000/-0.2553 | -0.9643/0.0000/-0.2649 |
| FM4 | 0.9661/0.0000/-0.2583 | -0.9659/0.0000/-0.2588 |
| FM5 | 0.9664/0.0000/-0.2571 | -0.9661/0.0000/-0.2583 |
| FM6 | 0.9669/0.0000/-0.2553 | -0.9662/0.0000/-0.2576 |

(a)



(b)



Fig. 3-2: Side view of satellites (a) F3/C and (b) GRACE, showing the normal (central axis of boresight) of the GPS antenna for each

## 3.2 Satellite center of mass and variation

All force models included in the equations of motion of a satellite must refer to the satellite COM. Thus, the pre-calibration of COMs for six satellites with stowed solar panels have been done in the NSPO laboratory with and without propellant fuels prior to launch. However, the incorrect exertion of thruster forces to the satellites caused by inaccurate COMs will lead to the difficulty in maneuvering the spacecraft.

Thus, the COMs and moments of inertia of all satellites are re-computed using refined measurements of masses of all satellite components. Also, the new determination is based on the case that the solar panels are deployed. Table 3-3 shows the coordinates of the COMs for different propellant masses from the post-launch determination. The standard errors of estimated COMs are at sub-mm level. The COMs vary with masses of propellant from a few mm to one cm.

For any given propellant mass, the COM coordinates in Table 3-3 are linearly interpolated. However, the rotation of the solar panels only affects COM at a sub-mm level, so it is negligible. The propellant will be partly consumed before the satellite reaches the final, operational orbit at about 800 km. Besides, the attitude control does not consume propellants, so the COM at the operational orbit will keep the same mass in the remaining mission lifetime.
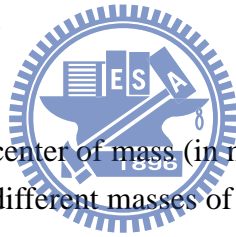
Table 3-3: Coordinates of center of mass (in mm) in the spacecraft coordinate frame at different masses of propellant

| Mass of propellant, kg | 6.65 | 3 | 2 | 0 |
|---|---|---|---|---|
| FM1 | 4 / -4 / -33[1] | -3 / -4 / -34 | -4 / -4 / -35 | -8 / -4 / -36 |
| FM2 | 4 / -4 / -34 | -2 / -4 / -35 | -4 / -4 / -35 | -8 / -4 / -36 |
| FM3 | 4 / -7 / -35 | -2 / -7 / -36 | -4 / -7 / -36 | -8 / -7 / -37 |
| FM4 | 4 / -8 / -34 | -2 / -7 / -36 | -4 / -7 / -36 | -8 / -7 / -37 |
| FM5 | 4 / -4 / -34 | -2 / -4 / -36 | -4 / -4 / -36 | -8 / -4 / -37 |
| FM6 | 4 / -4 / -33 | -2 / -4 / -35 | -4 / -4 / -35 | -8 / -4 / -36 |

[1]$x$, $y$ and $z$ components in the spacecraft coordinate frame

**3.3 Gain pattern, phase center offset and variation of antenna**

Most satellite missions are equipped with the BlackJack GPS receiver for geodetic purposes, e.g. CHAMP and GRACE mission or with the follow-on version IGOR, e.g. TerraSAR-X and F3/C missions. The IGOR receiver shows the perfect noise level of 1 mm for L1 and L2, even 3 mm for the ionosphere-free linear combination (Montenbruck et al. 2006). In order to obtain a better orbit accuracy of F3/C, a precise model of PCO and PCV, therefore, are required. This is especially designed for the kinematic solution due to the lack of any constraint imposed on the reduced-dynamic solution (see Chapter 6). Montenbruck et al. (2009) demonstrated the improvement in RMS values of the post-fit residual and the orbit overlap using the absolute phase pattern for the GRACE-B satellite. Jäggi et al. (2009) further demonstrated the improvement of GRACE orbits were based on the different phase pattern models. An empirical phase pattern was derived from in-flight phase residuals and an alternative approach is to directly estimating the correction map. The above approaches are in connection with the reduced-dynamic orbit determination. Furthermore, Schmid et al. (2005, 2007) demonstrated the improvement of both GPS orbit and clock products were based on the absolute phase pattern corresponding to the calibrated antenna in the GPS-processing procedure of IGS.

In this study, the pre-flight calibration of gain pattern, PCO and PCV of the two POD antennas, were achieved in an anechoic chamber using a mockup satellite of F3/C built by UCAR (Schreiner 2005).

### 3.3.1 Gain pattern

The mockup of F3/C used for the pre-flight calibration was placed in the electromagnetic environment, which is similar to the ionosphere, as shown in Fig. 3-3. Fig. 3-4 shows the absolute gain patterns for the POD antenna at L1 and L2 with a SAD orientation of $0°$. The dB value is proportional to the strength of GPS signal. As expected, the central amplitude of the phase gain pattern has a bigger dB value, in which the GPS signal has the better quality than that of the edge. Fig. 3-5 shows L1 and L2 with the maximum and minimum gain values at a field of view (FOV) of $120°$. The maximum amplitude values, 7.07 dB for L1 and 7.28 dB for L2, occur at the SAD angle of $270°$. The difference between maximum and minimum gains is about 12 dB, which roughly agrees with the value given by Montenbruck et al (2006).
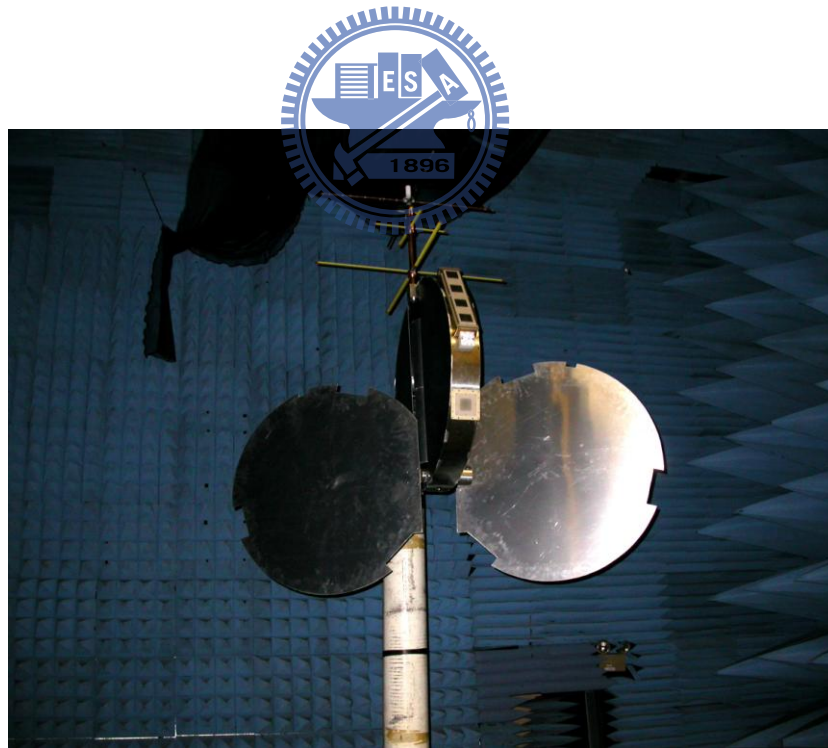


Fig. 3-3: Picture of F3/C spacecraft mockup mounted upside down in the anechoic chamber the solar arrays are oriented at 90 degrees. (courtesy of UCAR)
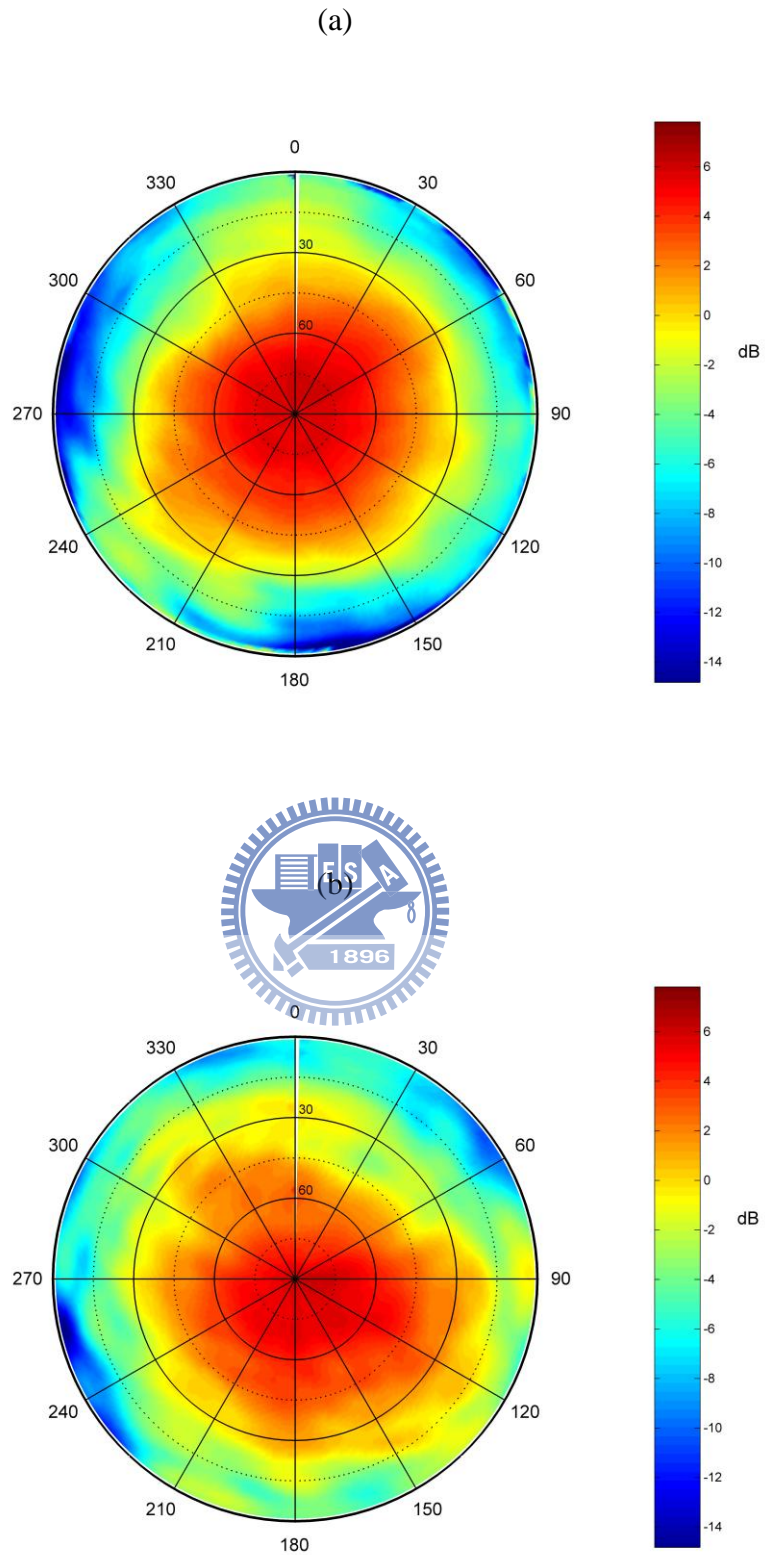
(a)



(b)



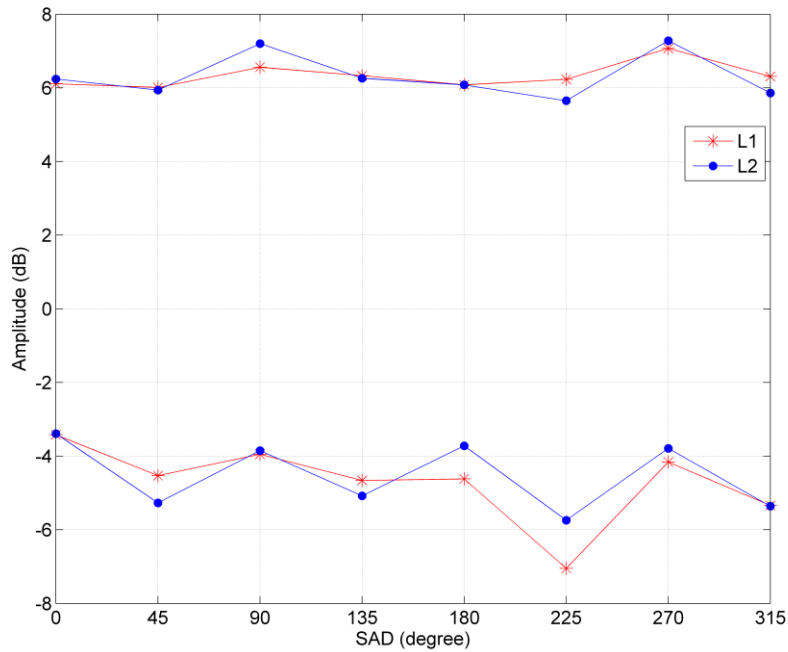Fig. 3-4: Gain patterns for (a) L1 and (b) L2 with the SAD angle of 0°

Fig. 3-5: Maximum and minimum gains for L1 and L2 within FOV of 120° from boresight

### 3.3.2 Phase center offset and variation of antenna

The phase centers of L1 and L2 were estimated with 8 different SAD angles. Table 3-4 shows the average absolute phase center offsets of L1 and L2. As expected, the largest offset lies in the zenith direction. Fig. 3-6 shows the PCV of L3 as a function of azimuth angle and zenith angle for an SAD angle of 0 degree (i.e. edge on to velocity vector). The large PCV value of ± 60 mm lies at azimuths from 120° to 210° and from 240° to 360° with the elevation lower than 30°. Obviously, the PCV in Fig. 3-6 is associated with the small amplitude of L1 gain pattern (-14 dB) in Fig. 3-4. Table 3-5 shows the maximum PCVs of L3 for different SAD angles. On average, the PCVs are small at small zenith angles. The largest PCV (absolute values) occur at azimuths of 140°-165° and 290°-350° and at large zenith angles (>80°). Fig. 3-7 shows the PCV as a function of zenith angle for L1 and L2 frequencies (averaged over azimuths and SAD angle = zero). The PCV varies smoothly with zenith angle, and

27

ranges from few mm (high zenith angle) to less than 2 cm (low zenith angle). In general, the PCV of L1 is larger than that of L2 at higher zenith angles (> 60°). The PCV of L3 is also important for the occultation research because ionosphere-free excess phase is required when processing occultation data.

Table 3-4: Antenna phase center offsets (in mm) from the anechoic chamber test (Hwang et al. 2009)

| Frequency | North | East | Up |
|-----------|-------|------|-----|
| L1 | -34.5/ -29.9[1] | -1.6/1.9 | 59.8/59.8 |
| L2 | -39.7/ -35.1 | 4.2/-3.9 | 71.3/71.4 |

[1]POD+X/POD-X
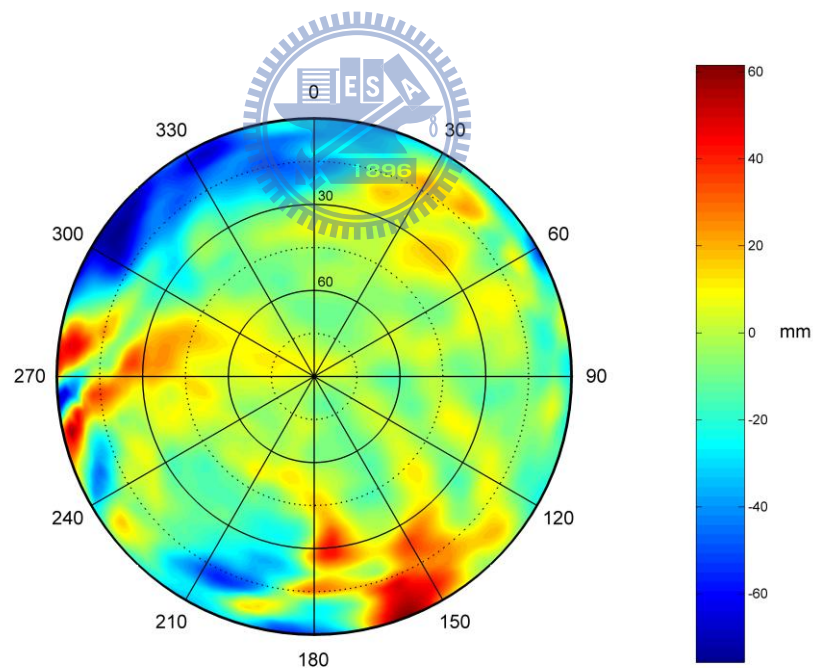


Fig. 3-6: Phase center variations of L3 as a function of azimuth (0°-360°) and zenith angle (0°-90°). The zenith angle is 0° at the center and 90° at the edge

Table 3-5: Maximum PCV of L3 for different solar array drive (SAD) angles (Hwang et al. 2009)

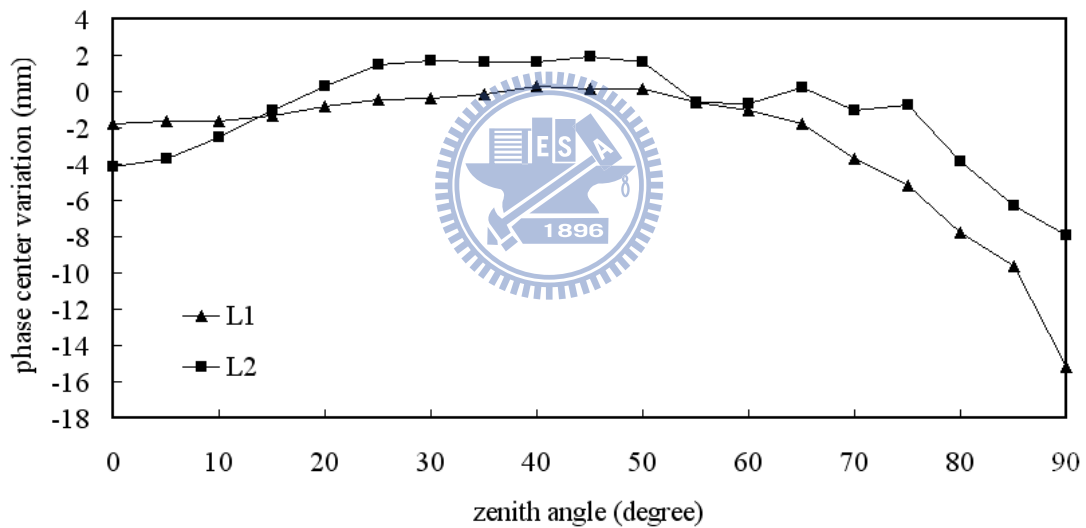| SAD angle (deg) | Maximum PCV (cm) |
|---|---|
| 0 | 6.37 |
| 45 | 6.24 |
| 90 | 4.91 |
| 135 | 6.90 |
| 180 | 5.29 |
| 225 | 12.06 |
| 270 | 5.70 |
| 315 | 6.93 |



Fig. 3-7: Average phase center variations of a POD antenna for L1 and L2 from the anechoic chamber test (Hwang et al. 2009)

## 3.4 Cable delay difference between two GPS antennas

According to Wu et al. (2005), a 2-ns signal delay will occur due to the cable difference between the two cables connecting the POD+X and –X antennas to the GOX receiver. Such effect of the cable delay have to be taken into account when the

GPS data from POD+X and −X are used simultaneously for the orbit determation. One method to remove this delay is to solve for two receiver clock corrections, instead of just one, in the F3/C orbit determination. As an example, Fig. 3-8 shows the differences between the two clock corrections estimated for the two antennas for FM5, Day 216, 2006 (based on the reduced-dynamic method). The differences in Fig. 3-8 have a RMS value of 2.89 ns, which roughly agrees with the value (2 ns) given by Wu et al. (2005) based on a laboratory test. Some of the large differences in Fig. 3-8 are due to estimation errors and low numbers of visible GPS satellites in one of the two POD antennas. At any epoch, the estimation of receiver clock corrections for two antennas can individually absorb the cable delay. Since data from the single GPS-antenna were used for POD in this study (see Chapter 4), the effect of the cable delay can be ignored. However, if data from the two POD antennas are combined and the cable delay is also properly taken into account, the GPS observations used in the POD will increase considerably. As a result, such a two-antenna solution will improve the accuracy of kinematic POD.
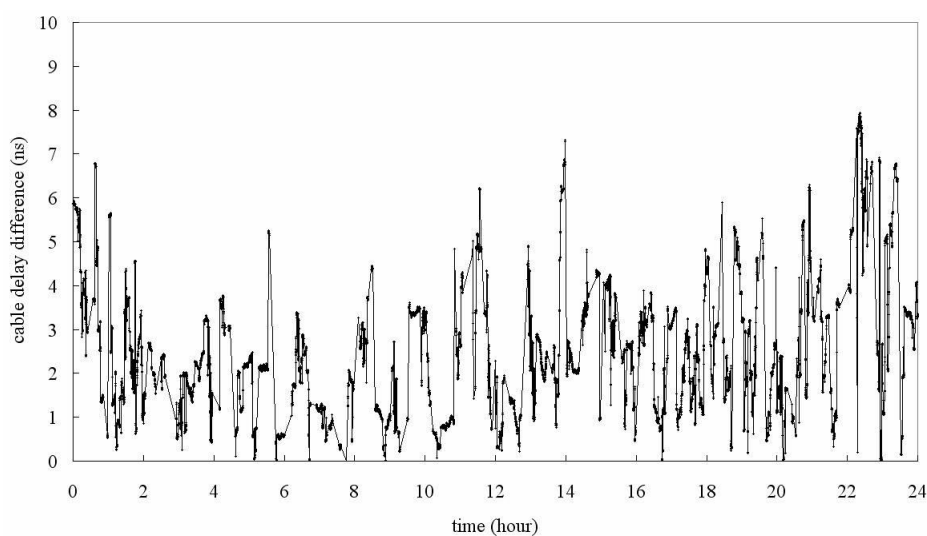


Fig. 3-8: Differences between clock corrections for the POD+X and -X antennas of FM5, Day 216, 2006 (Hwang et al. 2009)

# Сhapter 4

# Quality analysis of GPS POD data

## 4.1 Status and acquisition of F3/C GPS POD data

Fig. 4-1 shows the orbit maneuver schedule for the F3/C mission. Some of the
F3/C satellites stayed at a lower altitude of 525 km for as long as 520 days before
being raised to the final altitude of 711 km (FM3) and 800 km (others). At present, six
F3/C LEOs are at the final altitude of 800 km, except for FM3 (at 711 km). A
combination of low (525 km) and high (711 to 800 km) orbits can be used for gravity
recovery. A satellite with a lower orbit will be more sensitive to the higher frequency
gravity signal than the one with a higher orbit, but the former will suffer from a
relatively large air drag that might degrade gravity solutions if air drag is not properly
modeled. Also, during the first 13 months, FM3 and FM 4 formed a tandem flight
separated by about 80 km at an altitude of 525 km, possibly producing GRACE-like
range observables (but the accuracy inferior to that of GRACE) using kinematic GPS
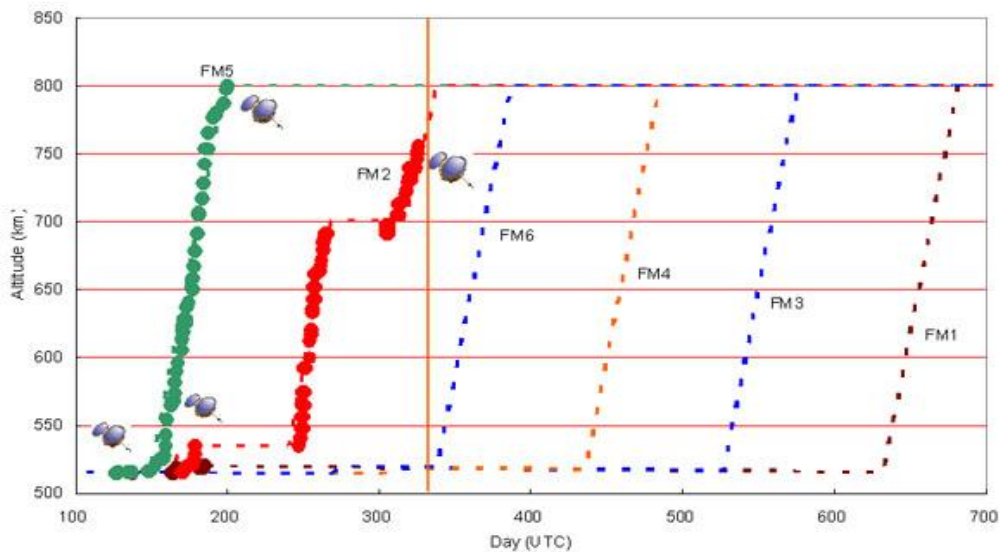baseline solutions.

Fig. 4-1: Orbit maneuver schedule of F3/C. The day is counted since January 1, 2006 (courtesy of NSPO)

Due to the GOX receiver software design, the numbers of tracked GPS satellites at POD+X and POD-X are not equal. Fig 4-2 shows the numbers of tracked GPS satellites at the two POD antennas for satellite FM2 and FM4 on Day 178, 2008. The two patch POD antennas of the F3/C receiver can receive up to 12 channels of GPS signals, of which 9 channels are allocated to the default antenna and 3 channels to another (Hwang et al. 2009). In this study, only the GPS signals collected by the default antenna will be used in POD and quality assessment. The non-default antenna viewing less than three GPS satellites cannot be used for sufficient kinematic orbit determination and cannot form double-differenced observables between POD-X and POD+X.

The GPS POD and attitude data are available on the TAAC web site of Central Weather Bureau of Taiwan (http://tacc.cwb.gov.tw/cdaac/index.html). The sampling interval of GPS POD carrier-phase and code observables is 10s. Real-time data are usually available within a few hours. Requests of F3/C GPS data should be sent to NSPO using the contact information at the NSPO web site.
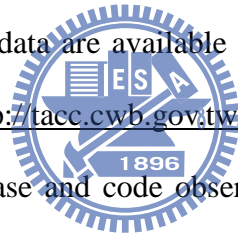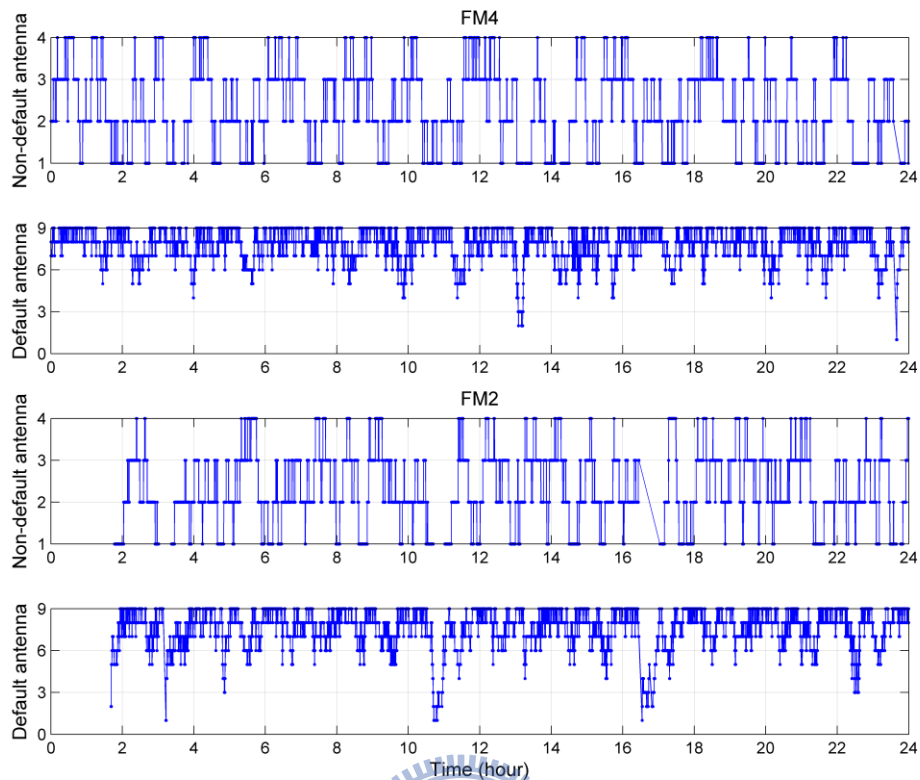
Fig. 4-2: The numbers of tracked GPS satellites at the two POD antennas for satellite FM2 and FM4 on Day 178, 2008

As mentioned before, the two patch antennas are not mounted in the zenith direction of the F3/C satellite. Since the FOV of F3/C POD antenna is restricted to 120° (Fig. 3-2 (a)), the geometry of tracked GPS satellites for F3/C is weaker than that for GRACE (Fig. 3-2(b)). Fig. 4-3 shows the sky plots of the default antenna for F3/C and GRACE-A satellites. The sky plot frame refers to a local antenna frame, with the zero-zenith direction pointing to the normal of the patch antenna and the zero-azimuth direction pointing to the −Z direction. Since the different FOVs (GRACE:180°) for F3/C and GRACE missions, the GPS satellite visibility of GRACE-A is larger than that of F3/C. The tracks in the sky plot of GRACE-A are smooth, meaning that the GPS signals are stably collected by the GRACE POD antenna. However, the tracks in the sky plot of F3/C are not smooth, and this might be associated with unstable

attitude control (see Chapter 5) due to F3/C's light weight of 62 kg and air-drag disturbance.
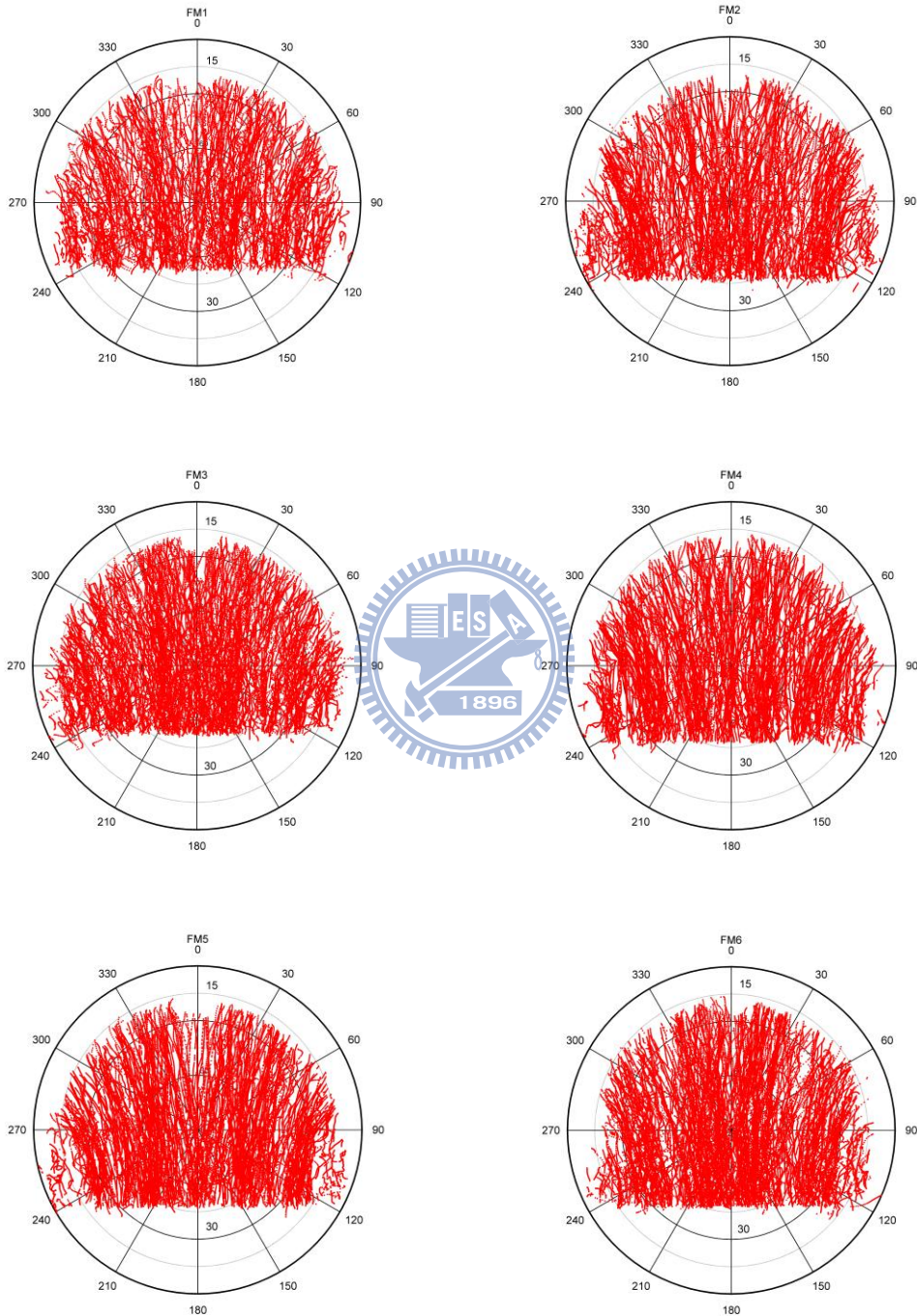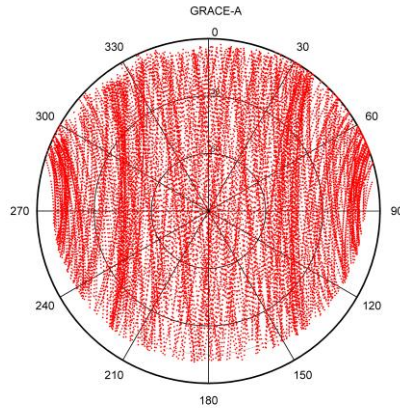
Fig. 4-3: Example of sky plots of the default antenna for F3/C and GRACE-A

## 4.2 Code multipath

GPS code measurements were used to obtain a priori orbit, and such orbit was used to detect outliers in data pre-processing prior to the final POD (Bock 2004, Hwang et al. 2009). The multipath effect of code may be severe for F3/C due to the way the solar panels are deployed and the use of patch antennas. The code multipath on F3/C and GRACE are determined using the software TEQC (Estey and Meertens 1999, Ogaja and Hedfors 2007). TEQC is designed for quality analysis of GPS/GLONASS data and has the following functions http://facility.unavco.org/software/teqc/teqc.html: (1) translation of GPS data from a binary format to a RINEX format (Gurtner 1994), (2) editing GPS observations, including data selection, metadata extraction and the title revision, and (3) QC of GPS observations. In this study, the QC function of TEQC was mainly used to form the linear combinations of pseudorange and carrier phase observations, which were used to compute (1) MP1 and MP2 (see Eqs. (2.9) and (2.10)), and (2) ionospheric delay (IODs) of carrier phases. A summary report of QC includes cycle slips of GPS carrier phases, MP1 and MP2, and other statistics.
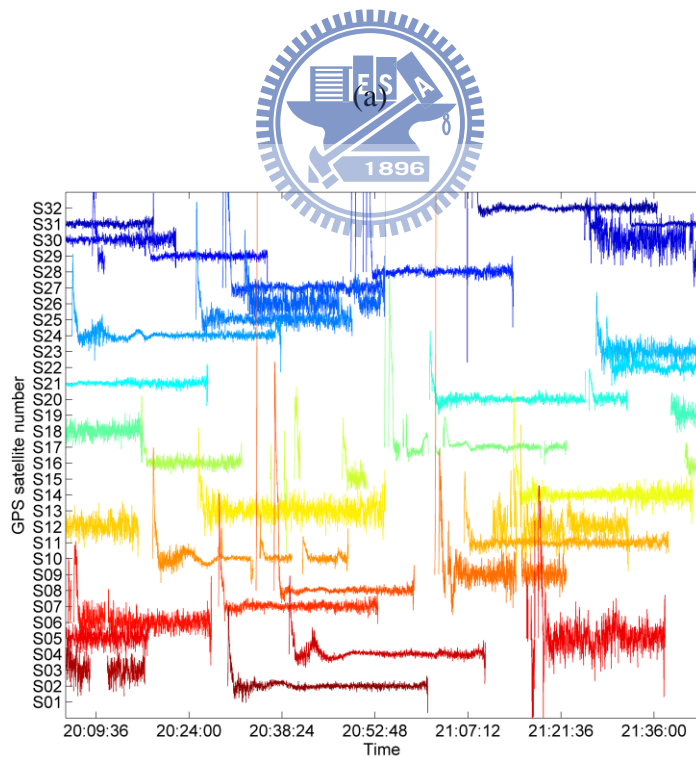
As a case study, the MP1 and MP2 of FM3 and GRACE-A on DOY 201, 2008

35

were investigated using TEQC. The F3/C GPS data were obtained from the Taiwan Analysis Center for F3/C and GRACE data was obtained from ftp://podaac.jpl.nasa.gov/pub/grace/data (LEVEL 1B product). Fig. 4-4 shows the patterns of MP1 and MP2 for FM3 (sampling rate: 1 Hz) and GRACE-A (sampling rate: 0.1 Hz) for each GPS satellite. In Fig. 4-4, the interval between two consecutive satellites along the vertical axis is 1 m and the symbol 'S' stands for the GPS satellite number and one color is associated with one GPS satellite. In general, the multipath of FM3 is larger than that of GRACE-A, and this is most likely caused by FM3's solar panels and antenna location. In some cases, the multipath effect can be very large - up to 23 m for S09 on FM3. Compared to the FM3 satellite, the GRACE-A experiences smaller multipath effects, but there are still relatively large multipath effects for some of the GPS satellites, e.g. S14, S23 and S30. Additionally, the pattern of MP2 for GRACE is worse than that of MP1. In one extreme case, the multipath effect of GRACE-A reaches 4 m for S23, which is caused by the unstable C/N0 in the last part of the arc, as shown in Fig. 4-5. Here C/N0 is defined as

$$C/N0 = 20 \cdot \log_{10}\left(\frac{SNR}{\sqrt{2}}\right) \qquad\qquad (4.1)$$

where SNR is GPS signal-to-noise ratio. In Fig. 4-5, the C/N0 of L1 is associated with the MP1 on S23, and the unstable C/N0 values of L1 appear in the last part of the arc. As a result, a large multipath will result in an unstable C/N0 value. Montenbruck and Kroes (2003) and Dickman et al. (2009) also pointed out that the variation of C/N0 can be an indicator of the code noise or the multipath effect. For most GPS signals collected by FM3, the multipath effects oscillate rapidly, while for GRACE-A the oscillations are relatively smaller. Fig. 4-6 shows the relationship between mean

elevation angle and the RMS values of MP1 and MP2 for FM3 and GRACE-A in a period of 1.5 hours on DOY 201, 2008. The elevation angle in Fig. 4-6 (and in TEQC) is based on a reference ellipsoid of WGS84 (GRS80). For GRACE-A, the elevation angles are always larger than zero, while for FM3 the elevation angles range from negative values to values <25°(except S22). Since the multipath effect of GRACE-A is smaller than that of FM3, it is expected that the a priori orbit of GRACE-A will outperform F3/C satellite orbits. In fact, examinations of multipath effects over some selected arcs of F3/C satellites and GRACE-A resulted in more or less the same conclusions as here on the pattern and magnitude of multipath effects. Therefore, the examples given in Figs. 4-4, 4-5 and 4-6 are representative of the features of multipath effects on the GPS observations of F3/C and GRACE-A satellite.



(a)

(b)
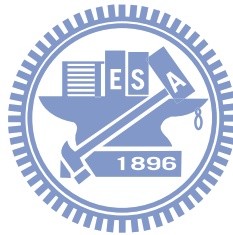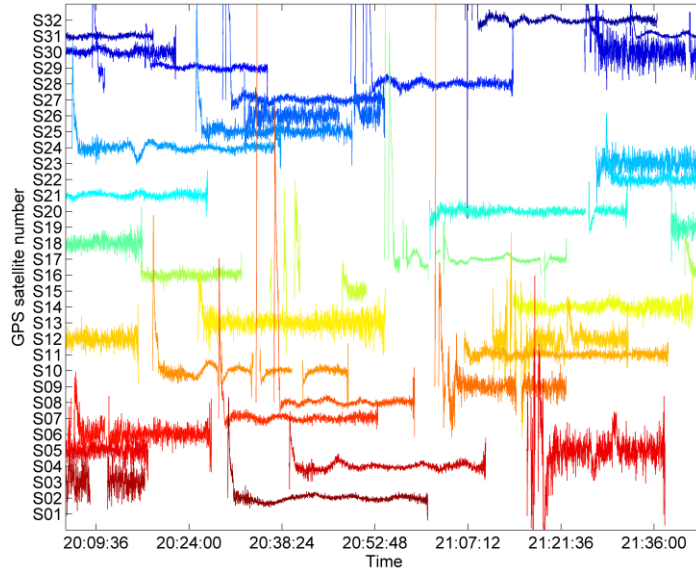


(c)
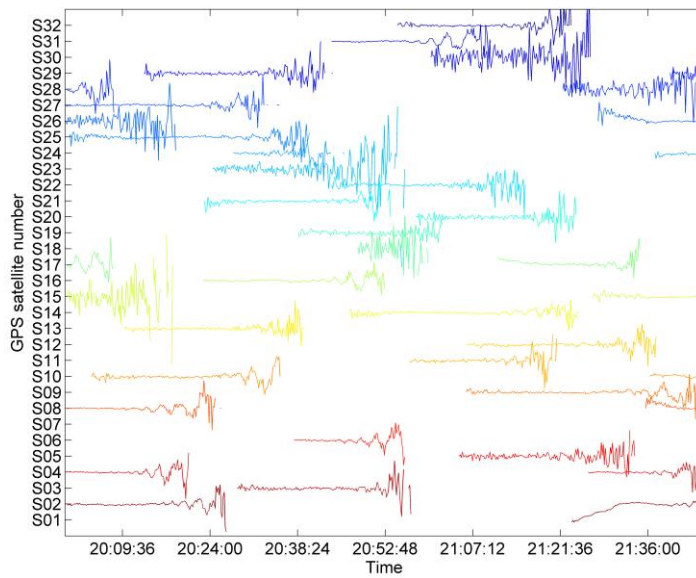
(d)



Fig. 4-4: (a) MP1 of FM3; (b) MP2 of FM3; (c) MP1 of GRACE-A (d) MP2 of GRACE-A (in m)



Fig. 4-5: C/N0 values for S23 associated with Fig. 4-4 (c) (d)

(a)
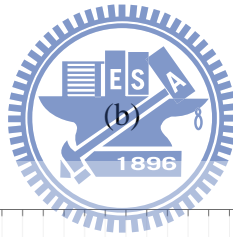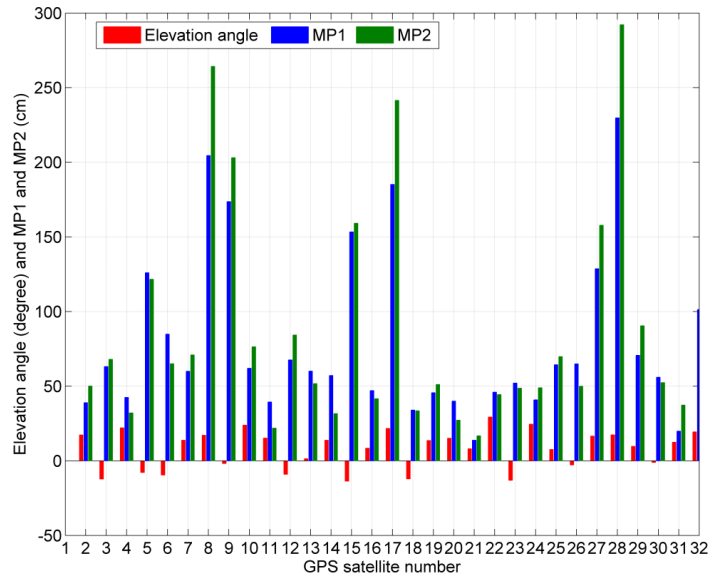


(b)
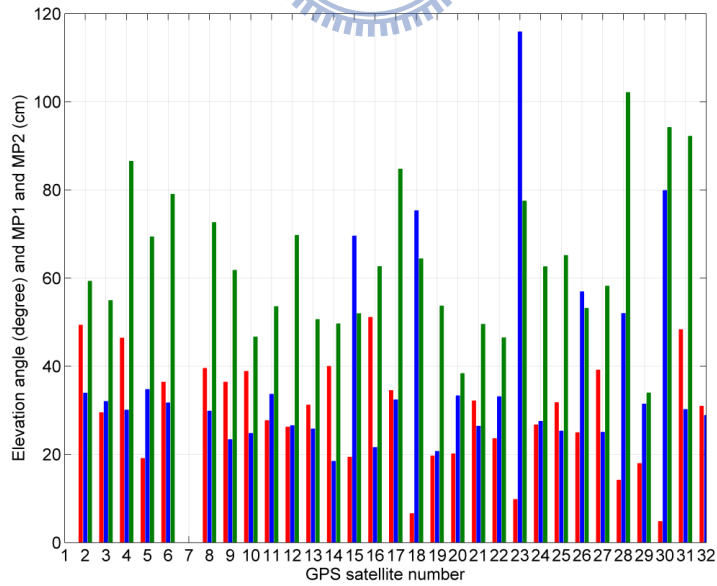


Fig. 4-6: Mean elevation angle and RMS values of MP1 and MP2 for (a) FM3 and (b) GRACE-A

40

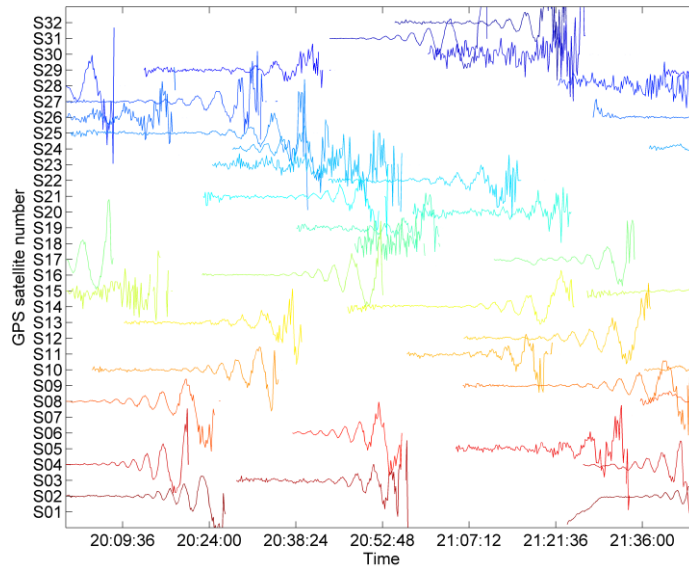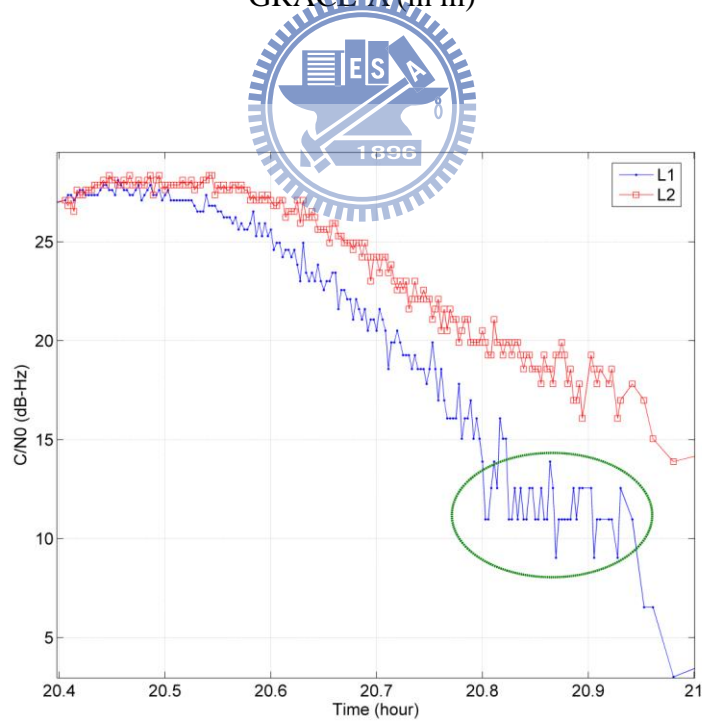Figs. 4-7 and 4-8 show the MP1 and MP2 of F3/C and GRACE satellites (with different scale in the vertical axis) over 126 days since DOY 240, 2008. The multipath effect in GRACE-B (average: 0.3 m) is much smaller than that in other LEOs presented in Figures. Furthermore, Fig. 4-9 shows the daily mean elevation angles of F3/C and GRACE satellites. The elevations of both GRACE satellites are more than 30°, while only three of F3/C satellites, FM1, FM3 and FM6, can occasionally reach 20° during this period. However, the elevations more than 50° for F3/C might be caused by GPS satellites passing from the horizon to the zenith of satellite body. The negative elevations appearing in FM5 is due to the location of POD antenna, which differs from GRACE POD antenna location. Fig. 4-10 shows the number of daily observations for F3/C and GRACE satellites with each data span of near 24 hours. The number of observations of GRACE-A is larger than that of the observations of other LEOs. However, FM4 shows a more stable tracking capability than other FMs, thanks to the good quality of attitude control. The gaps occurring in all F3/C data set are caused by the short data span(less than 24 hours) and bad attitude control in our selected F3/C data (see, Chapter 5).
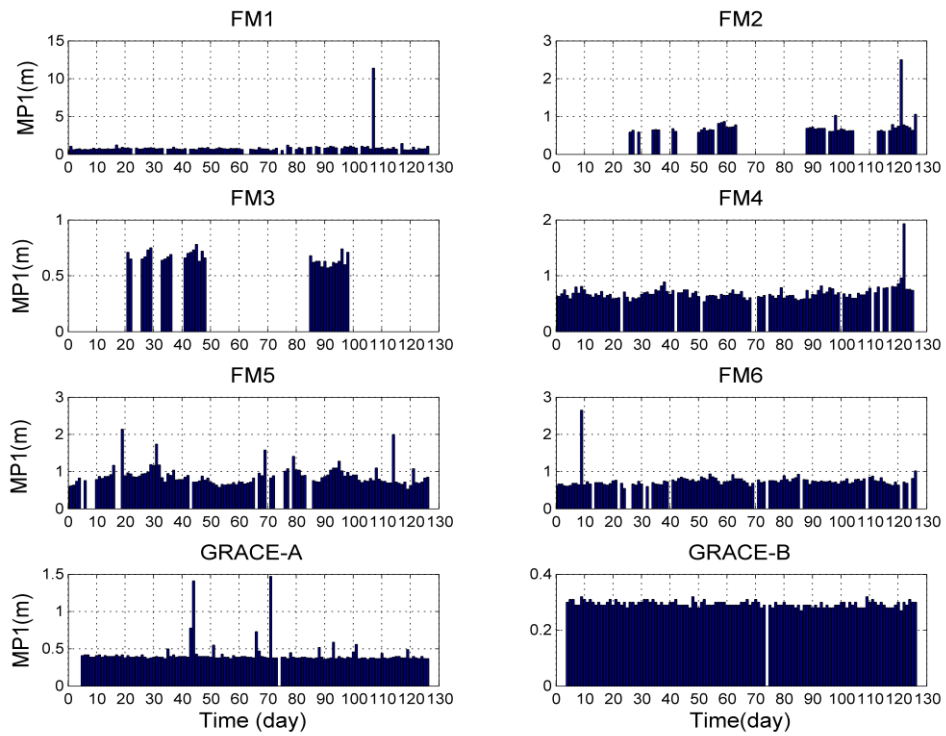
Fig. 4-7: MP1 of F3/C and GRACE satellites
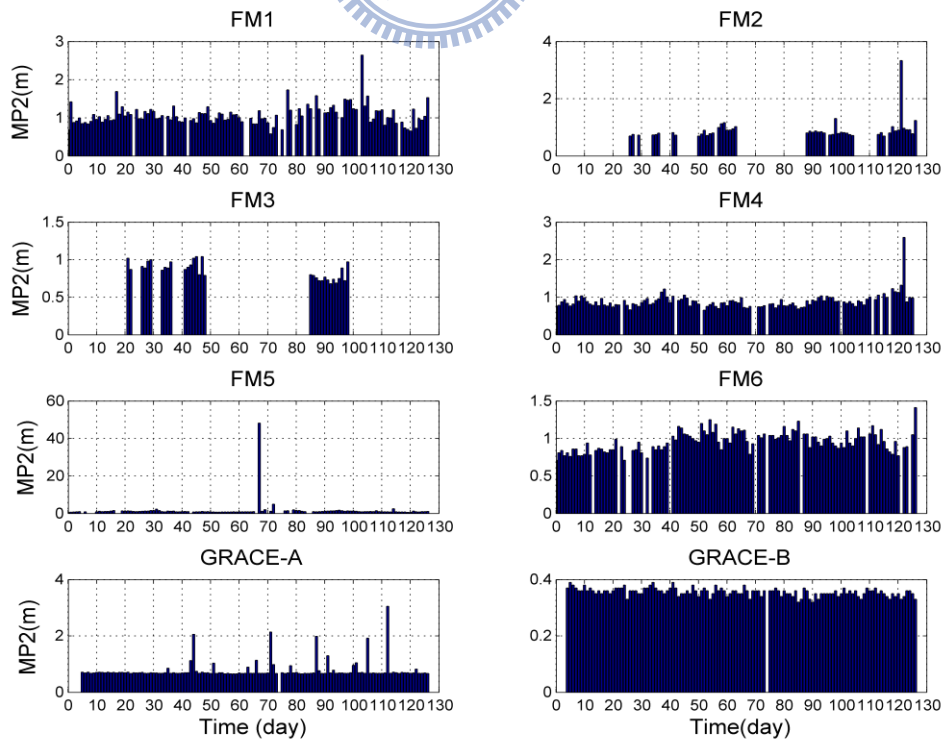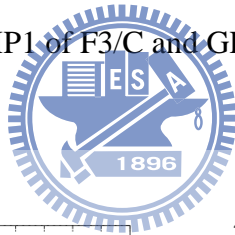


Fig. 4-8: MP2 of F3/C and GRACE satellites
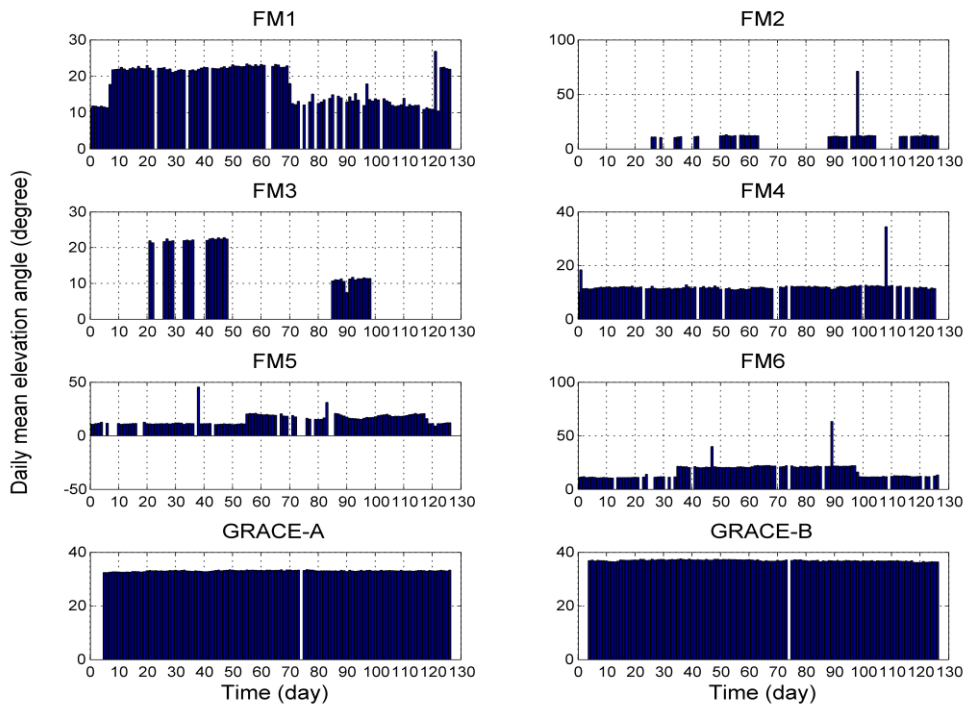
Fig. 4-9: Daily mean elevation angle of F3/C and GRACE satellites
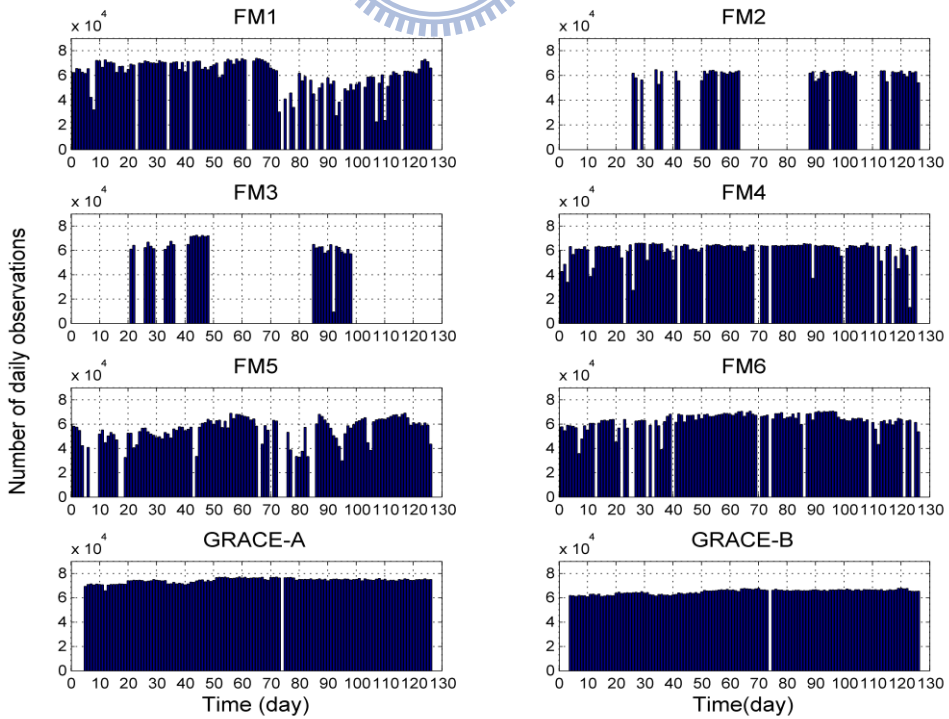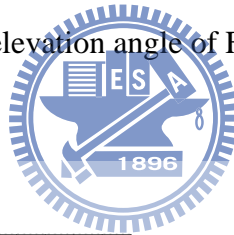


Fig. 4-10: Number of daily observations of F3/C and GRACE satellites

Table 4-1 summarizes the report of TEQC on the GPS data used over 126 days since DOY 240, 2008. The acceptance ratio in Table 4-1 is defined as the ratio between the total number of visible GPS satellites and the expected ones within 24 hours. On average, the total number of visible GPS satellites of all F3/C satellites is about 61057 less than that of two GRACE (69690) satellites, and the multipath effect of F3/C is 40 cm larger. The low number of visible GPS satellites of F3/C is due to the location of the patch antenna. For all F3/C satellites, MP2 is 30 cm larger than MP1. For two GRACE-A satellites, MP2 is 36 cm larger than MP1. However, for GRACE-B, MP2 is just 0.07 cm larger than MP1. On average, during this period, 7 GPS satellites per epoch are collected by all LEOs, except for GRACE-A (8 GPS satellites). A large difference between the mean elevation angles of F3/C and GRACE (15.5° vs. 35.0°, Table 4-1) will naturally lead to different qualities of GPS data from these two missions: a low or even negative elevation angle will experience a larger ionospheric effect in the space.

Table 4-1: A summary report of TEQC for FMs and GRACE-A based on GPS data over 126 days since DOY 240, 2008

| | MP1 (m) | MP2 (m) | Mean elev. (°) | Ave. Obs. | Ave. span (hour) | Num/epoch (0.1 Hz) |
|---|---|---|---|---|---|---|
| FM1 | 0.90 | 1.08 | 18.1 | 62100 | 23.0 | 7.5 |
| FM2 | 0.73 | 0.91 | 13.0 | 61420 | 23.8 | 7.2 |
| FM3 | 0.66 | 0.86 | 17.2 | 62750 | 23.8 | 7.3 |
| FM4 | 0.69 | 0.90 | 12.1 | 60660 | 23.7 | 7.1 |
| FM5 | 0.87 | 1.62 | 15.1 | 55920 | 23.5 | 6.6 |
| FM6 | 0.76 | 0.96 | 17.2 | 63490 | 23.5 | 7.5 |
| GRACE-A | 0.42 | 0.78 | 33.1 | 74310 | 24 | 8.6 |
| GRACE-B | 0.29 | 0.36 | 36.9 | 65070 | 24 | 7.5 |

## 4.3 Ionospheric delay and cycle slip

The geometry-free linear combination of L1 and L2, abbreviated with $L_C^4$, were used to detect the IOD and cycle slip on GPS carrier phase. $L_C^4$ can eliminate the receiver clock error and GPS satellite clock error, and can be expressed as

$$L_C^4 = \frac{1-\alpha}{\alpha} I_1 + \lambda_1 N_1 - \lambda_2 N_2 + m_1 - m_2 \qquad (4.2)$$

where $I_1$ is IOD of L1 and all denotations in Eq. (4.2) are the same as in Chapter 2. The difference between two consecutive $L_C^4$ values is

$$D_k = L_{C,k+1}^4 - L_{C,k}^4$$
$$= \frac{1-\alpha}{\alpha} [I_1^{k+1} - I_1^k] + (\Delta m_{12}^{k+1} - \Delta m_{12}^k) \qquad (4.3)$$

where $k$ is epoch number and $\Delta m_{12} = m_1 - m_2$. If no multipath and cycle slip occur, the variation of $D_k$ in Eq. (4.3) will be just due to the variation of IOD ($I_1$), and such a variation is expected to be smooth over time. The noise of GPS phase observables for F3/C can be estimated using

$$\sigma_{L1-LA} = \sqrt{\sigma_{L1}^2 + \sigma_{LA}^2} \qquad (4.4)$$

where $\sigma_{LA}$ is the noise of C/A code. Fig. 4-11 shows that the noise level of the carrier phase observation for FM4 is about 1.8 mm on DOY 27, 2008. This outcome agrees with the result of Montenbruck and Kroes (2003). Fig. 4-12 shows the

time-variations of $D_k$ and C/N0 for FM4 on DOY 27, 2008. Both variations are faster than normal at the later part of the arc, where the elevation angle approaches zero. Thus, the major cause of the fast variations of $D_k$ and C/N0 is the low elevation angle (Montenbruck and Kroes 2003).
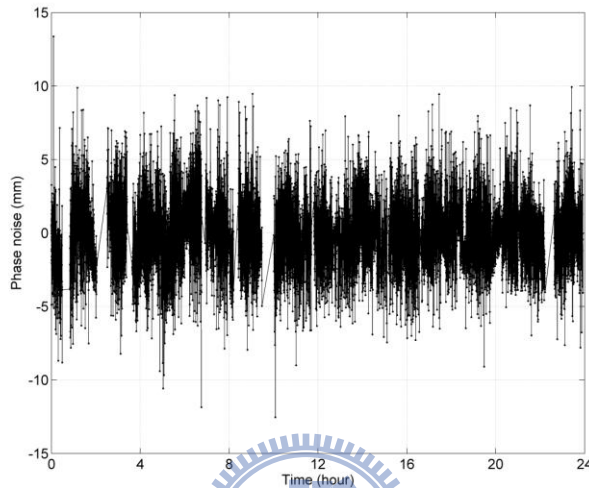


Fig. 4-11: Noises of GPS phase observations for FM4 on DOY 27, 2008
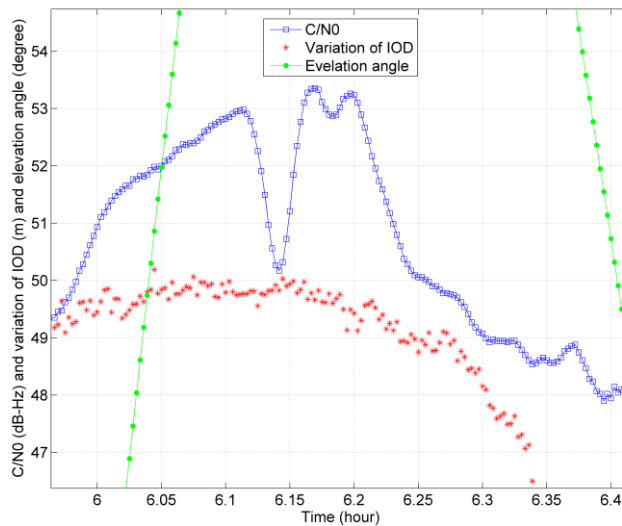


Fig. 4-12: Variations of IOD (shifted by 50 m) and C/N0 and elevation angle in the antenna frame for S20 on DOY 27, 2008

Any high-frequency oscillations in $D_k$ with amplitudes exceeding few millimeters are likely caused by multipath effects, and a sudden, large jump in $D_k$ is caused by cycle slip. The time-derivative of $D_k$ can be approximated by

$$\dot{D}_k = \frac{D_k}{\Delta t} \tag{4.5}$$

where $\Delta t = t_{k+1} - t_k$. Fig. 4-13 shows $\dot{D}_k$ of FM3 and GRACE-A at selected satellite arcs. In Fig. 4-13(a) and (b), a cycle slip is associated with a discontinuity in $\dot{D}_k$. A gap in $\dot{D}_k$ is most likely caused by bad attitude control or low SNR. A sudden change in $\dot{D}_k$ might be caused by a cycle slip or an outlier (Bock 2004), so Bernese uses a criterion based on differences between two successive observables of L1, L2 or $L_C^3$ to distinguish cycle slips from outliers in the data preprocessing (Dach et al. 2007). The $\dot{D}_k$ values (shown in brown to blue colors in Fig. 4-13) in the later part of each arc were caused by discontinuities in the phase data. For FM3, the occurrence frequency of cycle slip is relatively large in the GPS signals from S03, S05, S06, S09, S12, S18, S23 and S26. In the case of S06 for FM3, the cycle slip was associated with the low SNR of L2 (no SNR of L1 in the RINEX file), see Fig. 4-13(c). For GRACE-A, a relatively large number of cycle slips occur in the GPS signals from S23, S28 and S29. No IOD effect was found by GRACE-A. In Fig. 4-13, 147 cycle slips in FM3 were detected, compared to 67 cycle slips in GRACE-A. On average, the occurrence percentages of cycle slip for FM3 and GRACE-A are 1/29 and 1/84, respectively. Also, at the ending section of a FM3 arc, the variation of $\dot{D}_k$

is relatively large due to the negative elevation angles that give rise to a large IOD variation. For GRACE-A, such a fast variation of $\dot{D}_k$ did not occur because the elevation angles are always larger than zero. Again, large IOD and low C/N0 are mostly associated with low elevation angle. Fig. 4-14 shows the number of daily cycle slips and outliers for F3/C and GRACE over 126 days. Table 4-2 shows the statistic of Fig. 4-14. GRACE-B has the less cycle slips and outliers than other LEOs. During this period, GRACE-B has an excellent quality of GPS data due to the lower number of cycle slips and outliers (38), and the GPS data qualities of FM4 and FM2 are closed to that of GRACE-A. For other FMs, the cycle slips and outliers more than 1000 most likely are caused by multipath effect and the solar panel might block some GPS signals, as mention previously. It is not clear why the cycle slips and outliers in GRACE-A are much more than those in GRACE-B.

(a)
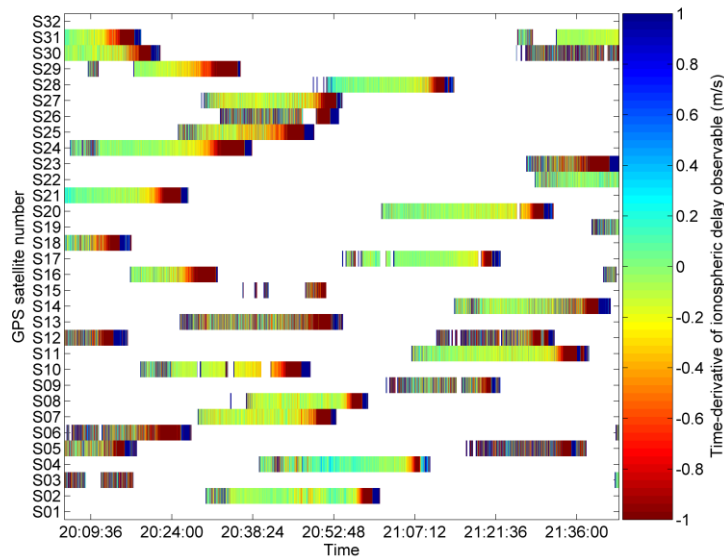
(b)
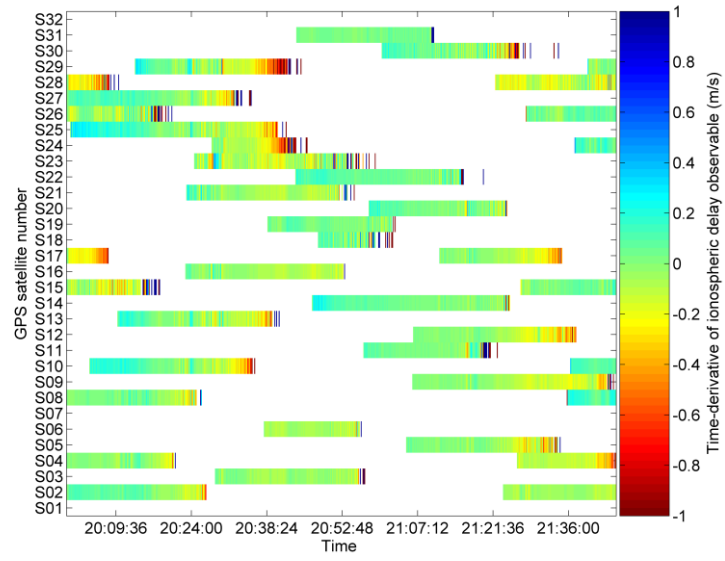


(c)
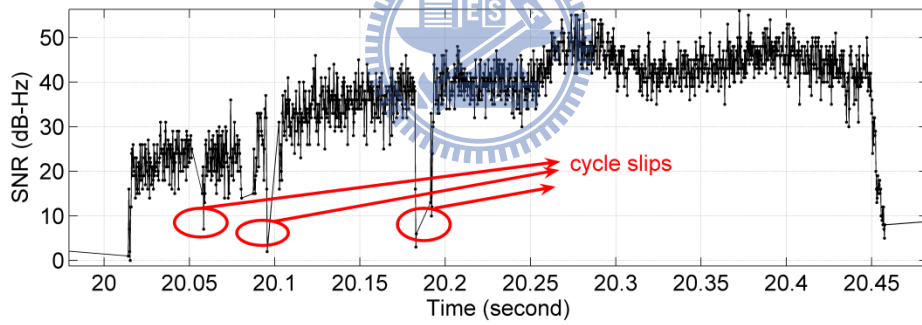


Fig. 4-13: Time-derivative of IOD for (a) FM3 and (b) GRACE-A and (c) SNR of S06 for FM3 associated with Fig 4-13(a) on DOY 201, 2008

50
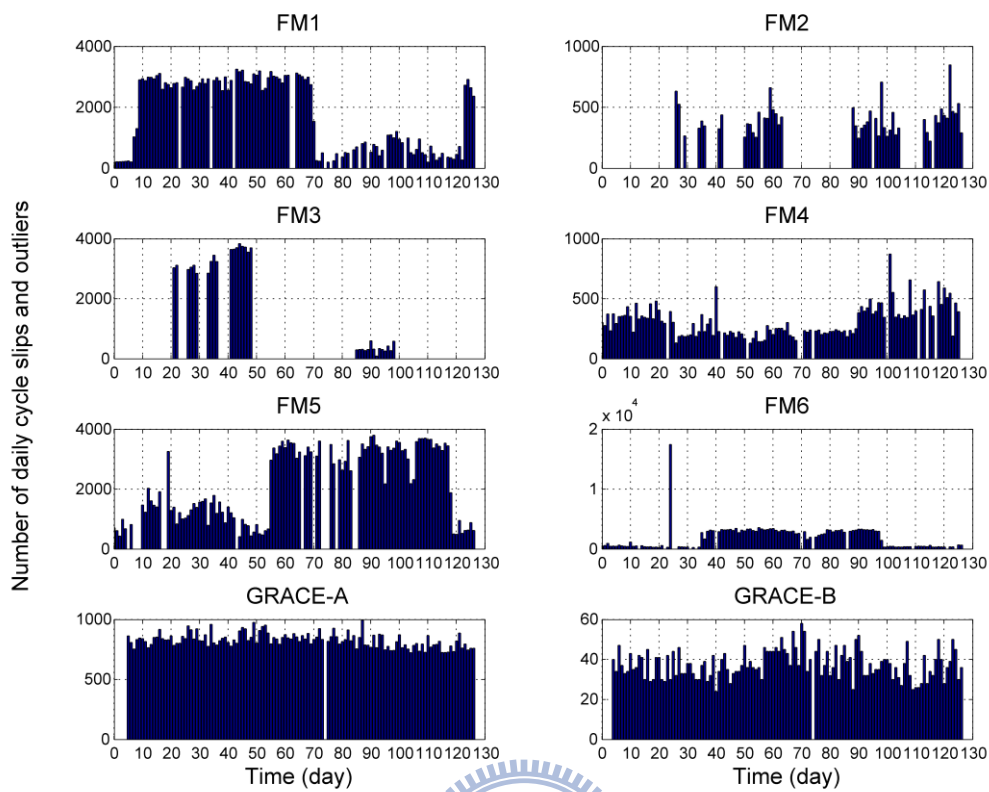
Fig. 4-14: Number of daily cycle slips and outliers of F3/C and GRACE satellites

Table 4-2: Number of daily cycle slips and outliers of F3/C and GRACE satellites
over 126 days since DOY 240, 2008

|  | FM1 | FM2 | FM3 | FM4 | FM5 | FM6 | GRACE-A | GRACE-B |
|---|---|---|---|---|---|---|---|---|
| Cycle slips and outliers | 1804 | 402 | 2030 | 314 | 2179 | 1939 | 828 | 38 |

Fig. 4-15(a) and (b) shows the daily numbers of GPS observation epochs and daily numbers of ambiguity parameters for satellites FM3, FM4 and GRACE-A over 300 days starting from DOY 100, 2007. A large number of cycle slips will result in a substantial reduction of degree of freedom and degraded orbit accuracy. To save the

51

computing time, we used a sampling rate of 0.1 Hz for both F3/C and GRACE-A. Over the time span in Fig. 4-15, the average daily number of effective observation epochs for FM3 and FM4 is under 8640 (an effective observation epoch means an epoch with at least one GPS signal). This suggests that tracking of GPS signals by FM3 and FM4 are not stable. The number of daily ambiguity parameters for FM3 or FM4 varies rapidly, but is a uniform for GRACE-A (about 400 daily). FM3 is the worst in terms of stability of GPS signal. The low number of ambiguity parameters of FM3 is simply due to the low number of effective observation epochs. Table 4-3 shows the average daily ambiguity parameters for F3/C and GRACE-A over 300 days. Because the number of ambiguity parameters of FM4 is close to that of GRACE-A, the GPS signal of FM4 is less interrupted, as compared to other satellites of F3/C.

(a)
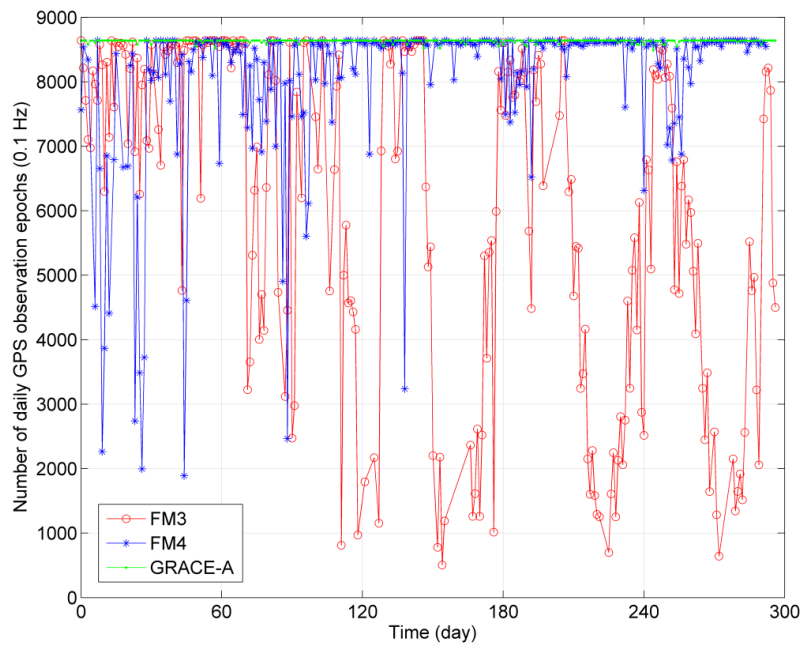
(b)
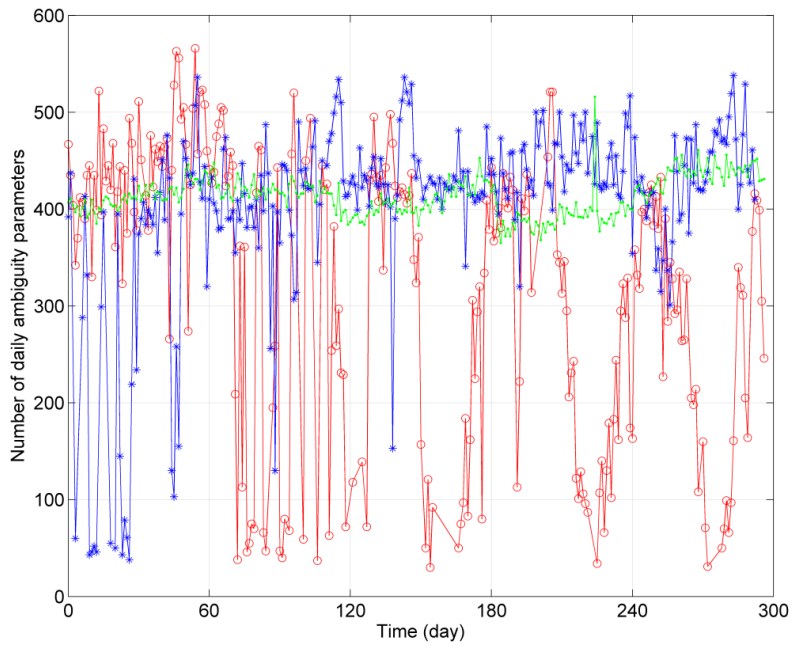


Fig. 4-15: (a) Number of daily GPS observation epochs and (b) number of daily ambiguity parameters for satellites FM3, FM4 and GRACE-A, since DOY 100, 2007

Table 4-3: Number of average daily GPS ambiguity parameters

|  | FM1 | FM2 | FM3 | FM4 | FM5 | FM6 | GRACE-A |
|---|---|---|---|---|---|---|---|
| Daily ambiguity | 198 | 253 | 286 | 406 | 212 | 158 | 413 |

# Chapter 5

# Attitude determination and control system for

# FORMOSAT-3/COSMIC

## 5.1 Spacecraft attitude definition

During the in-flight operation, ADCS is responsible for controlling the flight direction of a spacecraft and transforming satellite coordinates from the inertial frame to the spacecraft frame, especially for LEOs with the requirement of high accuracy orbits. Different missions require different accuracies of attitude control. Some general requirements for ADCS are listed as follows (Jan and Tsai 2005):

1. to provide the information for the orbit maneuver,
2. to stabilize the orientation of defined 3 axes based on the LVLH frame,
3. to transit the satellite from a post-launch separation to a stable status,
4. to stabilize the spacecraft from a tumbling status to a safe status autonomously.

In general, during the initial phase, the spacecraft is tumbling after the post-launch separation and no a priori attitude knowledge can be available. One useful method to solve this difficulty is to use a magnetic control system which will stabilize the spacecraft without a priori attitude information.

Let X, Y, Z denote a spacecraft frame. The +Z axis points to the nadir direction, the +X axis points to the velocity direction and the +Y axis is given by the right-hand rule. In the F3/C mission, the ADCS refers to a LVLH coordinate system, and the LVLH is defined by a spacecraft position and velocity, which are determined by the

navigation GPS system, as follows (Wertz 1991):

$$\mathbf{e_Z} = {-\mathbf{R_{SC}}} \Big/ {\|\mathbf{R_{SC}}\|} \tag{5.1}$$

$$\mathbf{e_Y} = {-(\mathbf{R_{SC}} \times \mathbf{V_{SC}})} \Big/ {\|\mathbf{R_{SC}} \times \mathbf{V_{SC}}\|} \tag{5.2}$$

$$\mathbf{e_X} = \mathbf{e_Y} \times \mathbf{e_Z} \tag{5.3}$$

where

$\mathbf{e_X}, \mathbf{e_Y}, \mathbf{e_Z}$     = the unit vectors of LVLH reference frame

$\mathbf{R_{SC}}, \mathbf{V_{SC}}$     = the spacecraft position and velocity vectors in an inertial frame

According to Euler's theorem; the rule that any finite rotation of a rigid body can be expressed as a rotation through a certain angle about a certain fixed axis and a rotating sequence 1-2-3 is used in this study (Wertz 1991). The Euler angles, roll ($\phi$), pitch ($\theta$) and yaw ($\psi$), are defined by the rotation around the basic vector $(\mathbf{e_X}, \mathbf{e_Y}, \mathbf{e_Z})$ of a spacecraft, as shown in Fig. 5-1. According to the rotating sequence 1-2-3, the attitude ATM can be expressed as (Wertz 1991)

$$\mathbf{A} = \begin{bmatrix} \cos\psi \cdot \cos\theta & \cos\psi \cdot \sin\theta \cdot \sin\phi + \sin\psi \cdot \cos\phi & -\cos\psi \cdot \sin\theta \cdot \cos\phi + \sin\psi \cdot \sin\phi \\ -\sin\psi \cdot \cos\theta & -\sin\psi \cdot \sin\theta \cdot \sin\phi + \cos\psi \cdot \cos\phi & \sin\psi \cdot \sin\theta \cdot \cos\phi + \cos\psi \cdot \sin\phi \\ \sin\theta & -\cos\theta \cdot \sin\phi & \cos\theta \cdot \cos\phi \end{bmatrix}$$

$$\tag{5.4}$$

Although Euler angles can be represented as a three-axis attitude, it involves the trigonometric function and suffers from singularities at some angles of pitch (see Eq.

(5.8)). For this reason, a quaternion (Euler systematic parameters) can be used for an alternative ATM instead of Euler angles and are defined by (Wertz 1991)

$$q_1 = |\mathbf{e_X}| \cdot \sin \frac{\Phi}{2}$$

$$q_2 = |\mathbf{e_Y}| \cdot \sin \frac{\Phi}{2}$$

$$q_3 = |\mathbf{e_Z}| \cdot \sin \frac{\Phi}{2} \tag{5.5}$$

$$q_4 = \cos \frac{\Phi}{2}$$

$\Phi$ = rotation angle around the Euler axis

$q_4$ = a scalar factor of the quaternion

The quaternion parameters satisfy the following constraint

$$q_1^2 + q_2^2 + q_3^2 + q_4^2 = 1 \tag{5.6}$$

The ATM can also be written as follows (Wertz 1991)

$$\mathbf{A} = \begin{bmatrix} q_1^2 - q_2^2 - q_3^2 + q_4^2 & 2(q_1q_2 + q_3q_4) & 2(q_1q_3 - q_2q_4) \\ 2(q_1q_2 - q_3q_4) & -q_1^2 + q_2^2 - q_3^2 + q_4^2 & 2(q_2q_3 + q_1q_4) \\ 2(q_1q_3 + q_2q_4) & 2(q_2q_3 - q_1q_4) & -q_1^2 - q_2^2 + q_3^2 + q_4^2 \end{bmatrix} = \left(A_{ij}\right) \tag{5.7}$$

A relationship can be established by Eqs. (5.4) and (5.7). If the quaternion is known, the Euler angles can be determined by (Wertz 1991)

$$\phi = \tan^{-1}\left(\frac{-A_{32}}{A_{33}}\right), \quad \theta = \sin^{-1}(A_{31}), \quad \psi = \tan^{-1}\left(\frac{-A_{21}}{A_{11}}\right) \tag{5.8}$$

In Eq. (5.8), a singularity occurs at $\theta = \pm 90°$ because $\phi$ and $\psi$ have the similar effects for this case. On the other hand, if the Euler angles are known, the quaternion can be determined by (Wertz 1991)

$$q_4 = \pm\frac{1}{2}\left(1 + A_{11} + A_{22} + A_{33}\right)^{1/2} \tag{5.9}$$

$$q_1 = \frac{1}{4q_4}\left(A_{23} - A_{32}\right) \tag{5.10}$$

$$q_2 = \frac{1}{4q_4}\left(A_{31} - A_{13}\right) \tag{5.11}$$

$$q_3 = \frac{1}{4q_4}\left(A_{12} - A_{21}\right) \tag{5.12}$$
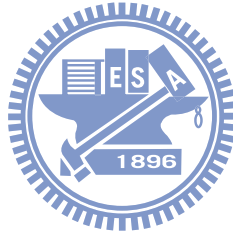
Quaternion provides a very convenient parameterization of attitude transformation since only four parameters are dominated without any singularity case. However, the disadvantage of quaternion is that cannot be explained with any obvious physical interpretation. Therefore, the Euler angles are usually used to present the operation of ACS during the in-flight operation.
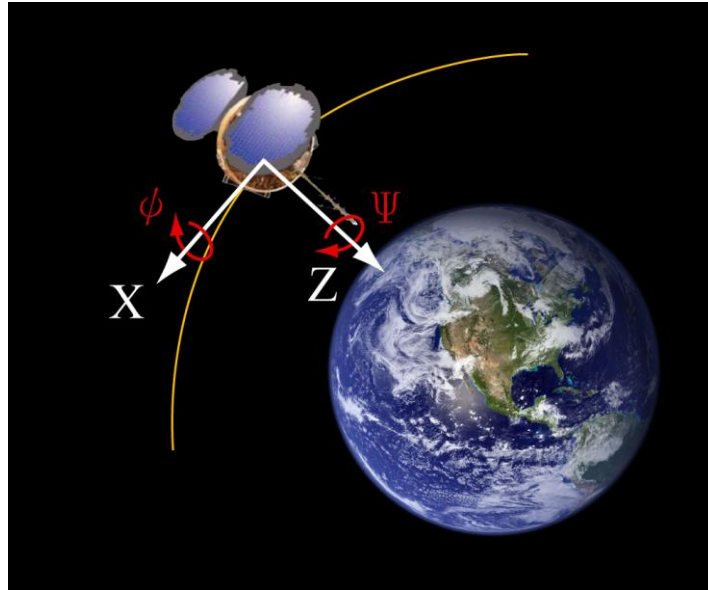
Fig. 5-1: Spacecraft coordinate frame of a F3/C satellite, +X points to the direction of flight and +Z points to the nadir direction

## 5.2 Attitude determination and control system

The ADCS consists of two earth horizon sensors, a magnetometer, eight course sun sensors, and a navigation GPS system. The function of each sensor is listed as follows:

- Earth horizon sensor: determining directly the orientation of a spacecraft with respect to the Earth;

- 3-axial Magnetometer sensor: measuring the strength and the direction of the geomagnetic field;

- Coarse sun sensor: measuring the sun vector in the spacecraft frame and providing a reference for onboard attitude control;

- GPS: proving position and velocity in the inertial true-of-date frame.

Additionally, the ADCS is equipped with three torque rods, a reaction wheels, and four thrusters for the active attitude control of the spacecraft. The function of each actuator is listed as follows:

- Torque rod: generating a 3-axis torques to resist the perturbation from the space

environment;

- Reaction wheel: providing a yaw-axis precise maneuver by torques;

- Thruster: producing a thrust for the orbit transfer and attitude maneuver of the spacecraft.

Fig. 5-2 shows the ADCS Functional Block Diagram. The major estimator, ARS, primarily collects the data from the scientific sensors and environment models. Eventually, ARS calculates the reference attitude information for the controller sending the command to SAD and actuators. The following sections will describe mode transitions in the mode-logic block which dominates the ARS block under the different conditions, as shown in Fig. 5-3. The mode logic block supports six modes: launch, stabilized, safehold, nadir, nadir/yaw, and thrust. In this study, only stabilized, safehold, nadir and nadir/yaw modes were concerned, since F3/C satellites were already working in the space. Additionally, for a normal operation, the ARS will not enter the thrust mode and should always stay in nadir/yaw mode. However, once the F3/C suffers from anomalies, the ARS will again enter to safehold mode or stabilized mode in order to track the geomagnetic field or be reinitialized. In the mode logic block, the mode transitions depend on the status of the spacecraft in the space.
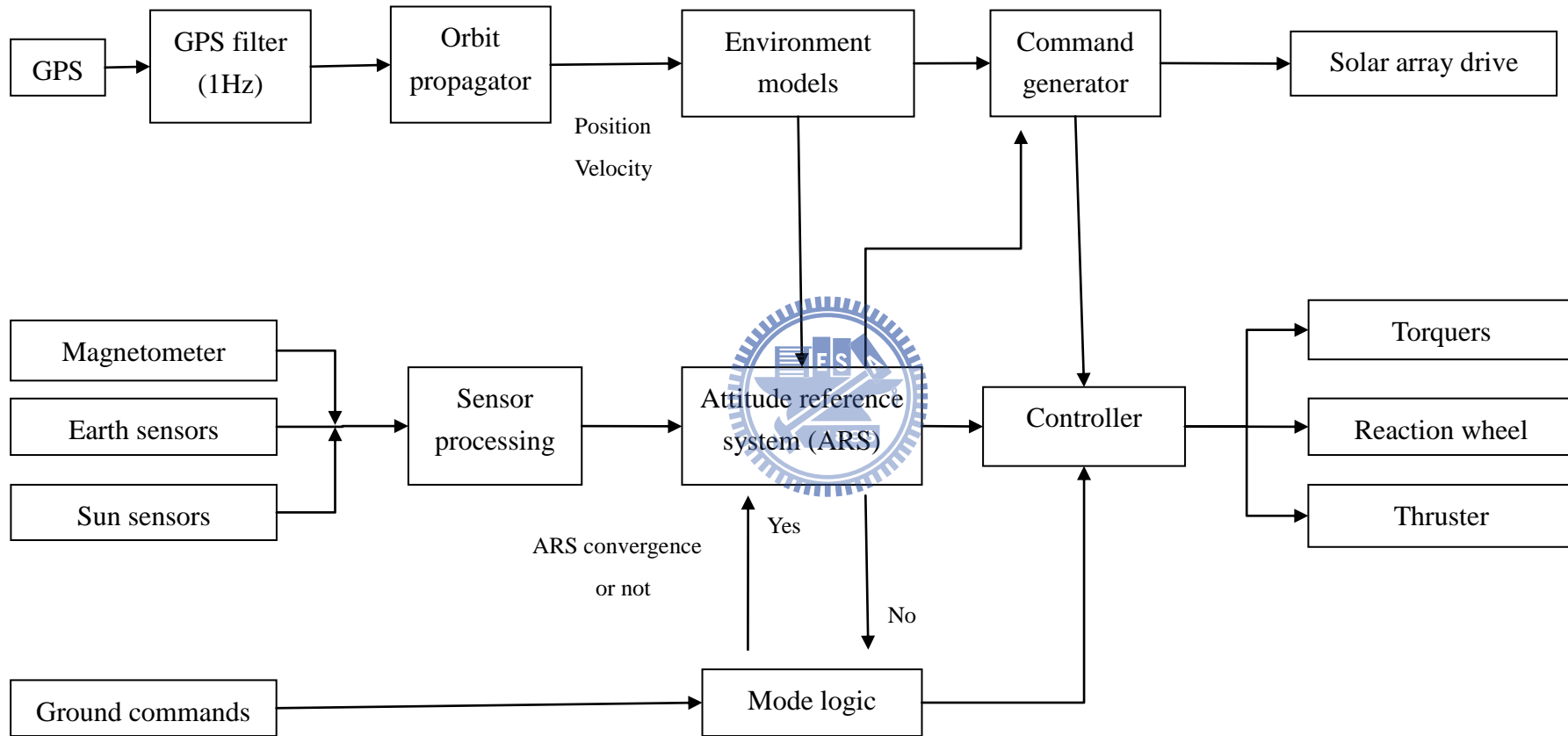
Fig. 5-2: ADCS functional block diagram
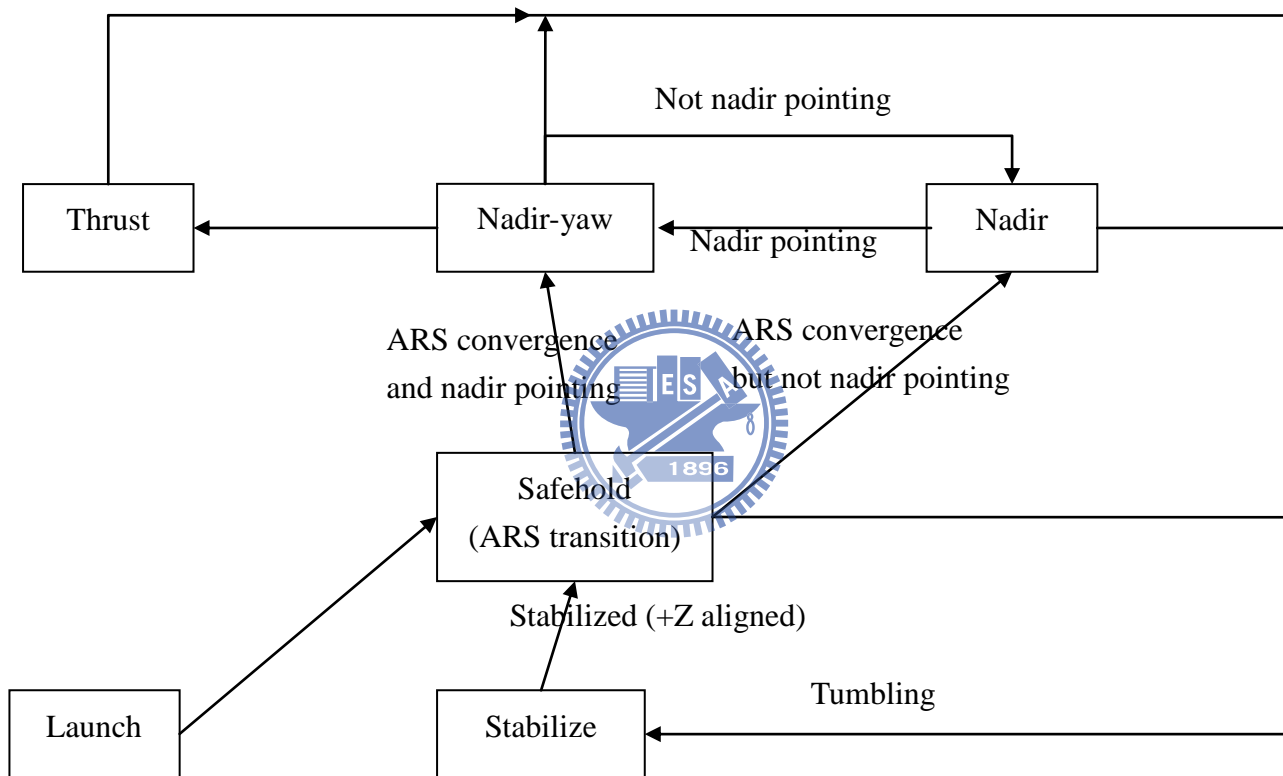
Fig. 5-3: Mode transition diagram of ADCS in the mode-logic block

## 5.3 Safehold/Stabilized mode in ARS

Safehold mode is a temporary and transitional mode among stabilized, nadir and nadir/yaw modes when launch mode is terminated. In this mode, ARS is forced to determine the attitude of F3/C using only the 3-axis magnetometer to measure the angle between the defined axis and the geomagnetic field vector. Subsequently, magnetic torquers are used to damp the spin rate resulting from the reaction wheel. In other words, safehold mode serves as an energy damper and attempts to reduce the residual rotational energy left by stabilized mode (discuss later). In the safehold mode, the solar array is commanded to face toward the Sun. However, the efficiency of the sun exposure is not sufficient due to lack of the yaw control knowledge (without entering the nadir-yaw mode, which will be discussed later). Besides, the safehold mode can also be switched on in ARS, even under a diverged condition or an unstable condition for the attitude estimation. In the safehold mode, the ARS will be switched on after an initialized period of 60 seconds, and then, the spacecraft will transit to nadir or nadir/yaw mode for a more stable attitude control.

The spacecraft may enter the stabilized mode when measuring high angular rates, tumbling, or even an anomalous thrust maneuver. From Fig. 5-3, ARS can directly execute the stabilized mode from other modes when F3/C suffers from anomalies. Under the stabilized mode, ARS also use the magnetometer to determine the F3/C attitude. Furthermore, the Z axis of F3/C is forced to align with the geomagnetic field vector (see Fig. 5-4) and torquers are used to dampen the disturbance of the spacecraft. If a high angular rate is detected in this mode, the spacecraft might have the bad quality of the GPS signal resulting in a weak POD stemming from poor ambiguity resolutions (Hwang et al. 2009). The stabilized mode is usually terminated near the north pole, where the acceptable attitude information is available. Once the spacecraft

is adequately aligned with the geomagnetic field vector, the ARS will transfer into the safehold mode (see Fig. 5-3).
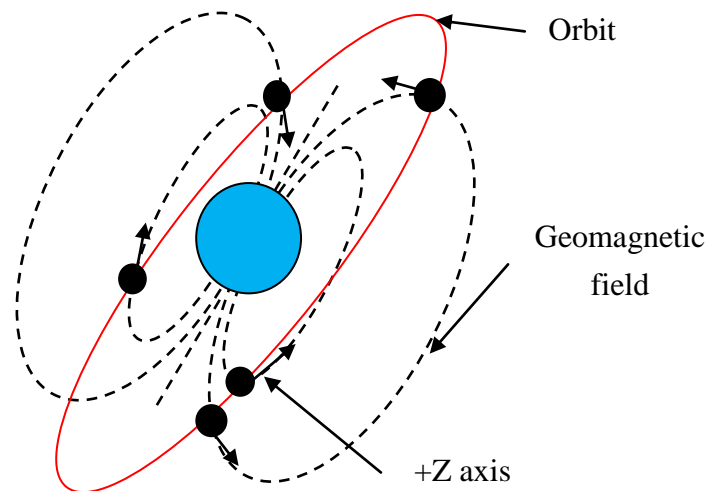


Fig. 5-4: F3/C in the safehold/stabilized mode

In stabilized, safehold and nadir modes, the 3-axis magnetic torquers are primarily used for the attitude control of F3/C. Here, the theory of magnetic torque will be addressed. When F3/C has a magnetic moment $\mathbf{M}$ obtained from the on-board magnetic torquer and an external geomagnetic field vector $\mathbf{B}$ obtained from the on-board magnetometer and the consequent moment $\mathbf{N}$ can be read as (Hughes 1986, p. 264),

$$\mathbf{N} = \mathbf{M} \times \mathbf{B} \tag{5.13}$$

The purpose of magnetic torquer is to align Z axis of F3/C with geomagnetic field direction and to damp the spin rate of F3/C satellite body. Thus, $\mathbf{M}$ can be

decomposed by $\mathbf{M}_{\mathbf{damp}}$ and $\mathbf{M}_{\mathbf{align}}$, as (Jan and Tsai 2005)

$$\mathbf{M} = \mathbf{M}_{\mathbf{damp}} + \mathbf{M}_{\mathbf{align}} = \mathbf{B_i} \times \left[ -K_{\dot{B}} \cdot \frac{d}{dt}\left( \frac{\mathbf{B_i} \times \mathbf{B_{i-1}}}{\|\mathbf{B_i}\|^2} \right) + K_{\theta} \cdot \left( \mathbf{Z_b} \times \mathbf{B_i} \right) \right] \qquad (5.14)$$

where $\mathbf{M}_{\mathbf{damp}}$ denotes the moment of damping the spin rate of satellite body; $\mathbf{M}_{\mathbf{align}}$ denotes the moment of aligning +Z axis with geomagnetic field vector; $\mathbf{B_i}$ and $\mathbf{B_{i-1}}$ denote the geomagnetic filed observed by the on-board magnetometer at epochs $i$ and $i$-1, respectively; $\mathbf{Z_b}$ denotes the unit vector of +Z axis of satellite body; $K_{\dot{B}}$ and $K_{\theta}$ is the control gain for damping and aligning, respectively.

For the angular rate reduction, $\dfrac{d}{dt}\left( \dfrac{\mathbf{B_i} \times \mathbf{B_{i-1}}}{\|\mathbf{B_i}\|^2} \right)$ can be approximated by the angular rate $\boldsymbol{\omega}$ of satellite. Thus (Jan and Tsai 2005),

$$\mathbf{M}_{\mathbf{damp}} = -\mathbf{B_i} \times \left\{ K_{\dot{B}} \cdot \frac{d}{dt}\left( \frac{\mathbf{B_i} \times \mathbf{B_{i-1}}}{\|\mathbf{B_i}\|^2} \right) \right\} = K_{\dot{B}} \cdot \left( \mathbf{B_i} \times \boldsymbol{\omega} \right) \qquad (5.15)$$

and the external magnetic torque $\mathbf{N}_{\mathbf{damp}}$ can be expressed as

$$\mathbf{N}_{\mathbf{damp}} = \mathbf{M}_{\mathbf{damp}} \times \mathbf{B_i} \qquad (5.16)$$

However, the variation of the magnetic field $\dot{\mathbf{B}}_{\mathbf{i}}$ can be expressed as

$$\dot{\mathbf{B}}_{\mathbf{i}} = \boldsymbol{\omega} \times \mathbf{B_i} \qquad (5.17)$$

Additionally, according to the formula of rotational kinetic energy $T$ with respect to time $t$ for an arbitrary body, it can be expressed for damping as (Jan and Tsai 2005)

$$\frac{d}{dt}(T) = \dot{T} = \mathbf{N_{damp}} \cdot \mathbf{\omega}$$  (5.18)

Therefore, according to Eq. (5.15) to (5.18), we can obtain (Jan and Tsai 2005)

$$\dot{T} = \dot{\mathbf{B}}_{\mathbf{i}} \cdot \mathbf{M_{damp}} = -K_{\dot{B}}\dot{\mathbf{B}}_{\mathbf{i}}^{2} = -K_{\dot{B}}\left|\mathbf{B_i} \times \mathbf{\omega}\right|^{2}$$  (5.19)

where the variation of $T$ is given with the negative energy standing for angular rate reduction.

For the torque of aligning +Z axis with geomagnetic field can be expressed as (Jan and Tsai 2005)

$$\mathbf{N_{align}} = \mathbf{M_{align}} \times \mathbf{B_i} = \left[\mathbf{B_i} \times K_{\theta} \cdot (\mathbf{Z_b} \times \mathbf{B_i})\right] \times \mathbf{B_i} = K_{\theta} \cdot \left\|\mathbf{B_i}\right\|^{2}\left(-B_y\mathbf{i} + B_x\mathbf{j}\right)$$  (5.20)

where the $B_x$ and $B_y$ is denoted as the components of the geomagnetic field along with $x$- and $y$-axis, which is measured by the on-board magnetometer. The unit vector of $x$- and $y$-axis is $\mathbf{i}$ and $\mathbf{j}$, respectively. Eq. (5.20) will be used to align +Z axis of F3/C with geomagnetic field.

## 5.4 Nadir mode in ARS

The purpose of nadir mode is to achieve nadir pointing regardless of the spacecraft current yaw orientation. When staying in a deterministic status or attitude

65

convergence, ARS will enter into the nadir mode. In addition, if the nadir-pointing error exceeds an user-specified value, ARS will again enter into the nadir mode.

## 5.5 Nadir-Yaw mode in ARS

The nadir-yaw mode is primarily used to maintain the +Z axis pointing to the nadir direction whenever the spacecraft travels around the earth. Under the nadir-yaw mode, ARS keeps the roll and pitch angle to 0° and yaw angle is commanded to a constant value. That is called the "Fixed-Yaw" sub-mode. However, the yaw angle constantly varies with beta angle (see the following section) in order to maximize the solar array efficiency. That is called the "Yaw-Steering" sub-mode, which provides a more stable power supplement environment as a default state in the nadir-yaw mode.

## 5.5.1 Nadir Yaw-Fixed
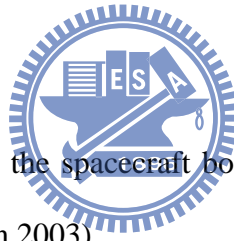
Yaw-fixed mode commands the spacecraft body frame to align with the LVLH frame according to Eq. (5.21) (Jan 2003)

$$
\begin{aligned}
\hat{z}_{cmd} &= \hat{z}_{LVLH} \\
\hat{y}_{cmd} &= \pm\hat{y}_{LVLH} \\
\hat{x}_{cmd} &= \pm\hat{x}_{LVLH}
\end{aligned}
\tag{5.21}
$$

The negative sign in $x$ and $y$ in Eq. (5.21) stands for the fixed yaw angle alternatively 0 or 180 degrees with respect to the z-axis. This is called "yaw-flip" which is periodical maneuver in response to the beta angle form the positive to negative or vice versa in order to keep the solar panels maximizing the sun exposure. The period is about 60 days and commands of the yaw-fixed are specified by

$$\phi_{cmd} = \theta_{cmd} = 0 \deg$$

$$\psi_{cmd} = 0 \text{ or } 180 \deg$$

To avoid large rotation in yaw angle during the period of yaw-flip maneuver, the commands of yaw angle are computed by (Jan 2003),

$$\dot{\psi}_{cmd}(n) = \pm\dot{\psi}_{max}$$
$$\psi_{cmd}(n) = \psi_{cmd}(n-1) \pm \dot{\psi}_{max}\Delta t$$

(5.22)

where $\dot{\psi}_{cmd}(n)$ and $\psi_{cmd}(n)$ denotes the yaw-command rate and angle at the $n_{th}$ control cycle, respectively; $\dot{\psi}_{max}$ is the maximum allowable yaw angular rate given by the ground control center, and $\Delta t$ is the ADCS control cycle interval between two consecutive control cycles. Eq. (5.22) is used to adjust the $n_{th}$ yaw command sufficiently closed to the desired yaw-fixed attitude. So, no oversize yaw angular rate exceeds the user-specified value (Jan 2003).

### 5.5.2 Nadir Yaw-Steering

Yaw-steering provides a more stable power supplement environment and manipulates the solar panel to maximize the sun exposure. The F3/C will be dominated by two sub-modes, "optimal" and "inverse" yaw steering, when performing the yaw-steering mode. They depend on the sun beta angle (β) which is the angle between the vector from the earth to the sun $\mathbf{S}$ and a vector normal to the orbit plane $\mathbf{N}$. The β is defined as (see Fig. 5-5)

$$\mathbf{N}\cdot\mathbf{S} = 1 \Rightarrow \beta = 90°$$
$$\mathbf{N}\cdot\mathbf{S} = 0 \Rightarrow \beta = 0°$$

(5.23)
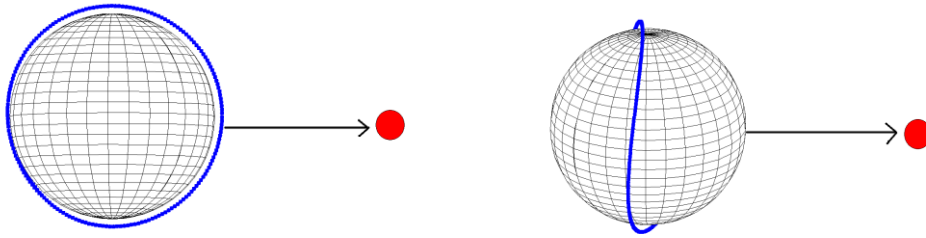
Fig. 5-5: β=0° (left) and β=90° (right)

Pitch and roll angles relative to the LVLH frame are always controlled to 0° as in the yaw-fixed sub-mode. The optimal yaw steering is implemented with a large β angle, whereas the inverse yaw steering is implemented with a small β angle. The transition point between the two steering modes occurs at β angle of 42° that implicitly means an unstable attitude control easily appears due to the shift of sensors.

### 5.5.2.1 Optimal Yaw-Steering

In optimal yaw-steering model, +X of the spacecraft is aligned with the velocity direction and the solar array illumination can be maximized for the power output. However, the error in yaw command will reduce the solar array illumination and a algorithm of computing yaw command is shown below:

$$\psi_{cmd}(n) \approx \tan^{-1}(\frac{\tan \beta}{\sin \nu}) \tag{5.24}$$

where $\nu$ is the angle between the vector **S** projected onto the orbit plane and the zenith direction of F3/C. In the case of high β, Eq. (5.24) is usually used to estimate

the yaw command in order to make the maximum sun illumination of the solar panel as much as possible. Fig. 5-6 shows the angle of the solar array for FM3 DOY 219, 2008. According to Fig. 5-5 (right), the sun is always at right hand side or left hand side with respect to the flight direction of F3/C. That means the angle of the solar array will keep a constant value around the Y axis. For negative β angles, the estimated yaw angle is presented by adding 180°.

The yaw rate command is computed by

$$\dot{\psi}_{cmd}(n) = \frac{\psi_{cmd}(n) - \psi_{cmd}(n-1)}{\Delta t} \tag{5.25}$$

Eq. (5.25) is used to implement the yaw-rate command until the $n_{th}$ yaw command is sufficiently close to the desired attitude. This way can prevent the occurrence of the oversize angle from the yaw manipulation during a transition from fixed-yaw to yaw-steering sub-modes.
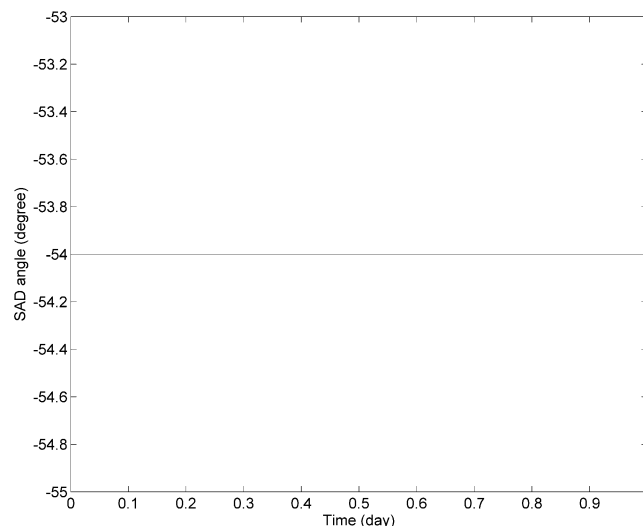


Fig. 5-6: The angle of the solar array at β=75.01°

**5.5.2.2 Inverse Yaw-Steering**

The transition point between the optimal and inverse sub-modes occurs at β angle of 42°. Fig. 5-7 shows the angle of SAD and yaw attitude at β=43° degrees for FM1 DOY 108, 2008. An anomaly attitude control usually occurs at β near the transition angle due to the shifts of scientific sensors. The following equation can be used for inverse yaw-steering algorithm:

$$\psi_{cmd}(n) \approx \beta \cdot \sin(\nu) \tag{5.26}$$

Fig. 5-8 shows the angle of SAD at β= 2.21° for FM4 DOY 148, 2008. According to Fig. 5-5 (left), as the sun transits, the spacecraft rotates the solar panel from a forward-looking to a backward-looking, so that the spacecraft can continue to track the sun. For negative β angles, the estimated yaw angle is presented by adding 180°. Fig. 5-9 shows the yaw angle of F3/C satellites at β near 0°.

(a)
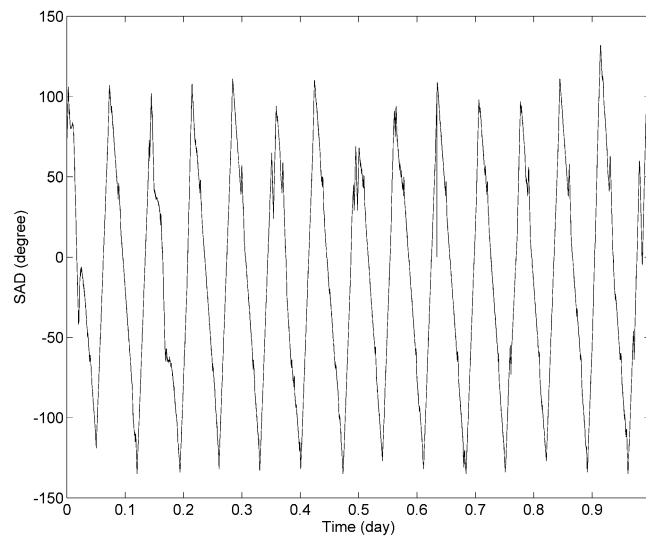
(b)
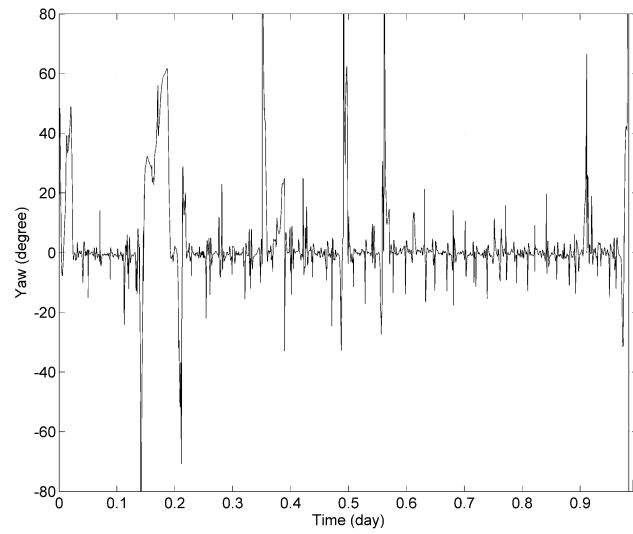


Fig. 5-7: (a) The SAD angle and (b) yaw attitude angle of F3/C at β=43° for FM1
DOY 108, 2008
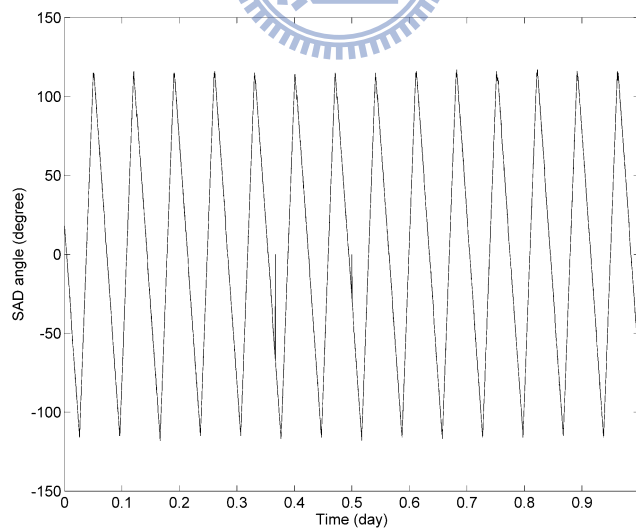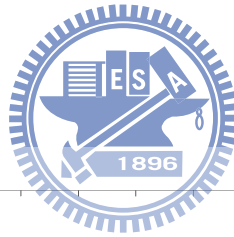


Fig. 5-8: angle of the solar array at β=2.21°

## 5.6 Analysis of attitude control

In this section, we assess formal errors due to attitude errors using a priori knowledge of the attitude accuracy of F3/C given by the F3/C mission center. The attitude determination of a F3/C satellite is based on a combination of outputs from a magnetometer, two earth sensors and eight sun sensors. Different weights are given to these sensors to obtain the optimal attitude of a F3/C satellite via the Kalman filter estimator. In general, the earth sensor has the largest weight, but it is less accurate at higher latitudes where the ice-covered surface may lead to an erroneous determination of attitude. The Euler angles, the position and velocity determined by an onboard GPS navigational receiver, are combined with those onboard sensor data to form the quaternion through an extended Kalman filter (EKF) method.

The quaternion is used for the coordinate frame transformation from the spacecraft frame to the inertial frame (Wertz, 1978). Table 5-1 shows the estimated errors of Euler angles at the altitudes of 550 and 800 km based on NSPO ground tests. Such errors will be introduced into the coordinate transformation. To estimate such errors, it is convenient to express transformation in Euler angles:

$$\mathbf{r_I} = \mathbf{A^T r_V} \tag{5.27}$$

where $\mathbf{r_I}, \mathbf{r_V}$ are coordinate vectors expressed in the inertial and spacecraft frames, respectively. $\mathbf{A}$ is the rotation matrix and is obtained from Eq. (5.4) using Euler angles (Long et al., 1989, p. 3-72). Matrix $\mathbf{A}$ can be expressed as

$$\mathbf{A} = \mathbf{R_1}(\phi)\mathbf{R_2}(-\theta)\mathbf{R_3}(\psi) \tag{5.28}$$

where $R_i$, $i = 1, 2, 3$, are rotation matrices about X, Y and Z (Seeber, 2003, p. 11). Let

vector $\mathbf{P} = (\phi, \theta, \psi)^{\mathrm{T}} = (p_i)^{\mathrm{T}}$ contain the Euler angels. The following differential

relationship holds:

$$d\mathbf{r_I} = \frac{\partial \mathbf{r_I}}{\partial \mathbf{p}^{\mathrm{T}}} d\mathbf{p} = \mathbf{B} d\mathbf{p} \tag{5.29}$$

and

$$\mathbf{B} = \frac{\partial \left( \mathbf{A}^{\mathrm{T}}(\mathbf{p}) \mathbf{r_V} \right)}{\partial \mathbf{p}^{\mathrm{T}}} = \sum_{i=1}^{3} \mathbf{e_i}^{\mathrm{T}} \otimes \left( \frac{\partial \mathbf{A}^{\mathrm{T}}}{\partial p_i} \mathbf{r_V} \right) \tag{5.30}$$

where $e_i$ is a $3 \times 1$ vector of all zeros, except for the $i$th element, and $\otimes$ is the

Kronecker product. Given the nominal standard errors of $\phi, \theta, \psi$ (Table 5-1) and the

coordinates of the two POD antennas (Table 3-1), the error covariance matrix of the

inertial coordinates are derived as

$$\sum_{\mathbf{r_I}} = \mathbf{B} \sum_{\mathbf{r_V}} \mathbf{B}^{\mathrm{T}} \tag{5.31}$$

Table 5-1 also shows the standard errors of the inertial coordinates caused by errors in

Euler angles at the altitudes of 550 and 800 km. The coordinate errors in Table 5-1 are

associated with typical Euler angles from F3/C and such errors at cm level will

propagate into the orbit determination. For comparison, the two GRACE satellites are

equipped with a star-camera for attitude control and the attitude accuracy of GRACE

satellites are controlled under less than 0.4°. Alternatively, "nominal" attitudes can be

used to replace observed attitudes and determined by the satellite's position and

velocity vectors (Neumayer et al., 2005). Kang et al. (2006) demonstrated that the mean orbit difference between the cases of using nominal and measured attitudes data was 0.1 mm for GRACE mission, which was significantly less than those given in Table 5-1 (for F3/C satellites). However, in the real POD data processing, Eq. (5.7) are truly used for the coordinate frame transformation due to no singularity is involved in the ATM.

Table 5-1: Attitude errors and attitude-induced coordinate errors (in *x*, *y*, *z*) in the inertial frame (Hwang et al. 2009)

| Altitude (km) | Attitude error in roll, pitch, yaw (degree) | Coordinate error, POD+X (mm) | Coordinate error, POD-X (mm) |
|---|---|---|---|
| 550 | 0.6/0.9/1.3 | 6.8/9.9/0.762 | 6.4/9.8/7.2 |
| 800 | 2.0/1.0/2.0 | 10.7/16.6/8.5 | 9.9/16.5/8.0 |

Additionally, the magnetometer and the earth horizon sensors are used to collect attitude data when F3/C enters the eclipse where the sun sensors are not involved. Fig. 5-9 shows the yaw variation in eclipse for FM4 DOY 178, 2008. The shift from one sensor to another before and after the eclipse will result in anomalous attitude observations (spikes). Such spikes might be mostly absorbed by the pseudo stochastic pulses (see Chapter 6) in the reduced-dynamic orbit determination, but not in the case of kinematic orbit determination.
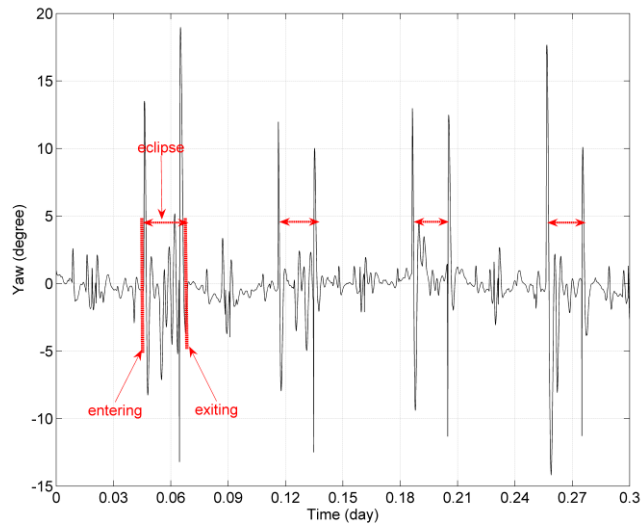
Fig. 5-9: The yaw variation in eclipse for FM4 DOY 178, 2008

The nadir-yaw-steering mode is implemented mainly depending on the β angle to keep the solar panel maximizing sun exposure and to obtain a better attitude control. Fig. 5-10 shows the daily attitude excursion of each F3/C in 2008. The spikes in Fig. 5-10 mostly occur at the transition angle but also at the non-transition angle. For FM6, the large attitude excursions in first 100 days compared to other days are due to some unexpected errors result from the in-flight software design (private communication: NSPO). Table 5-2 shows the daily mean attitude excursion associated with Fig. 5-10. For, FM6, if we removed the excursions of first 100 days, the value will be down to 4.42° that roughly agree with those given in other FMs, except for FM1. However, there is no clear reason for the large excursion (8.49°) in FM1, but it might be caused by poor attitude controls (private communication: NSPO). Furthermore, such effects will affect the orbit determination (see Chapter 6 and Chapter 7), especially for the kinematic approach.

(a)



(b)

(c)



(d)



77
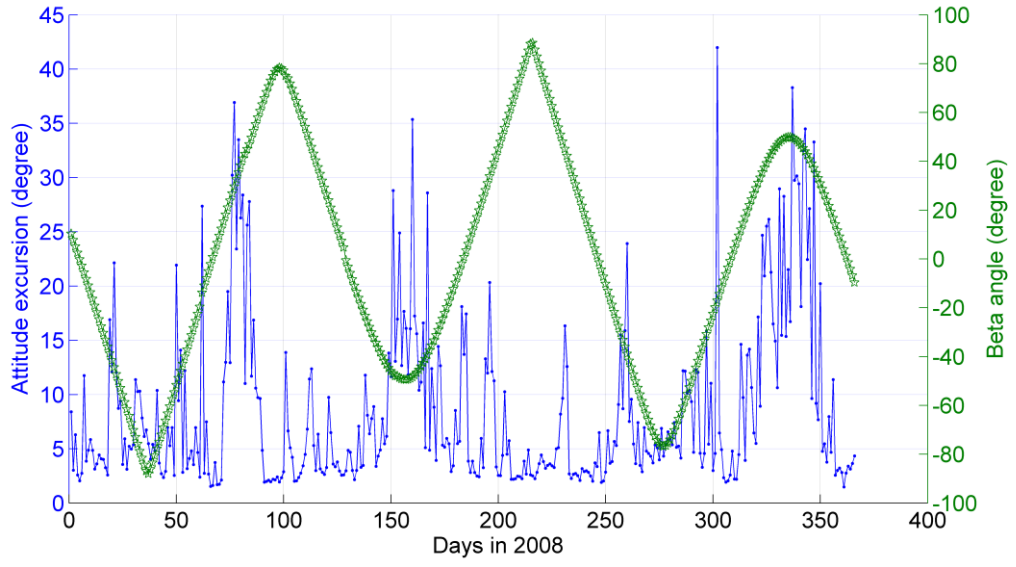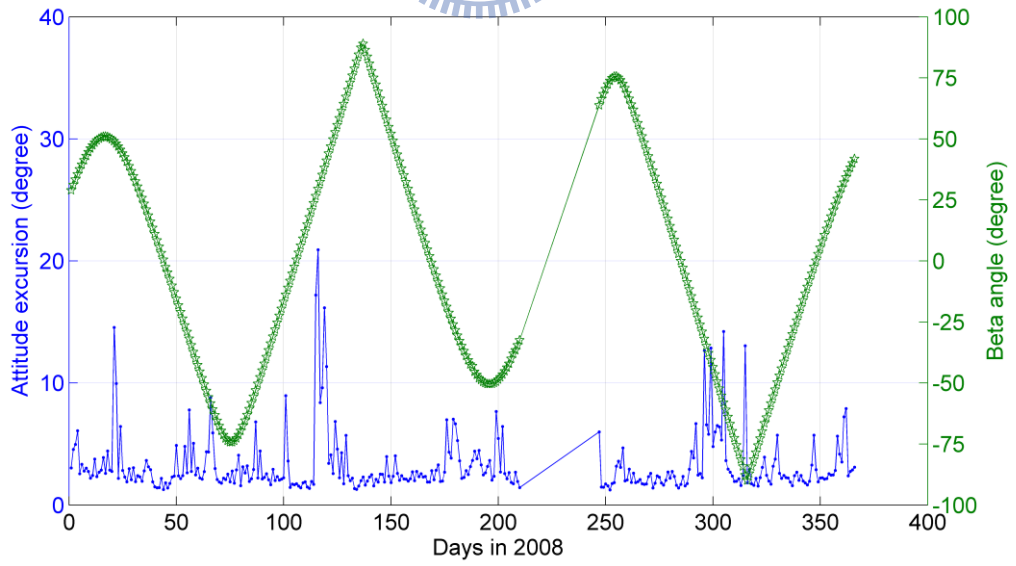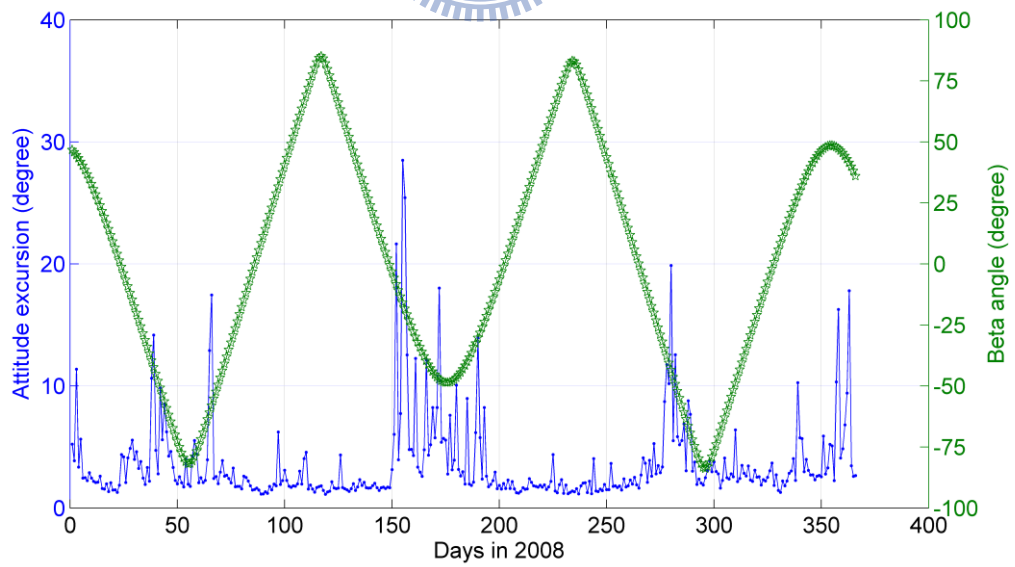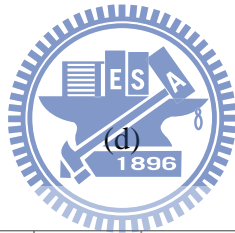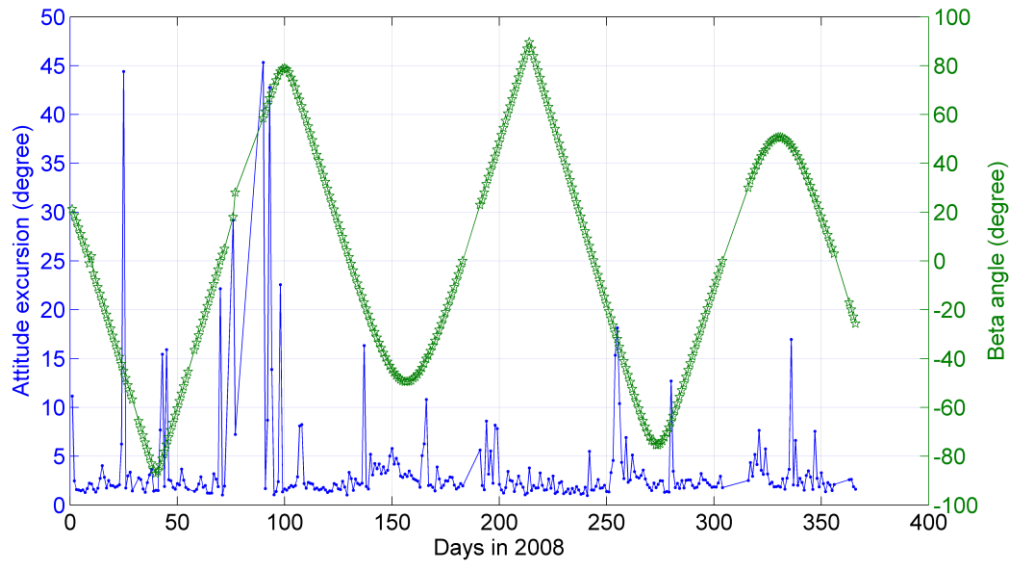
(e)
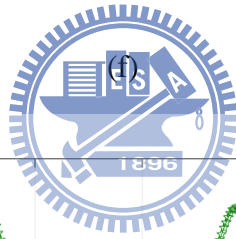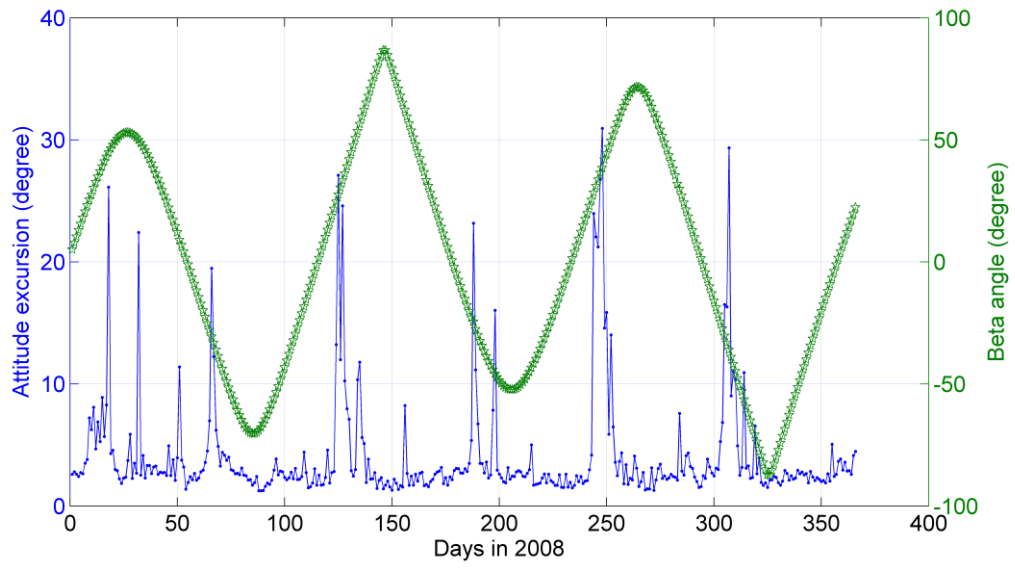


(f)
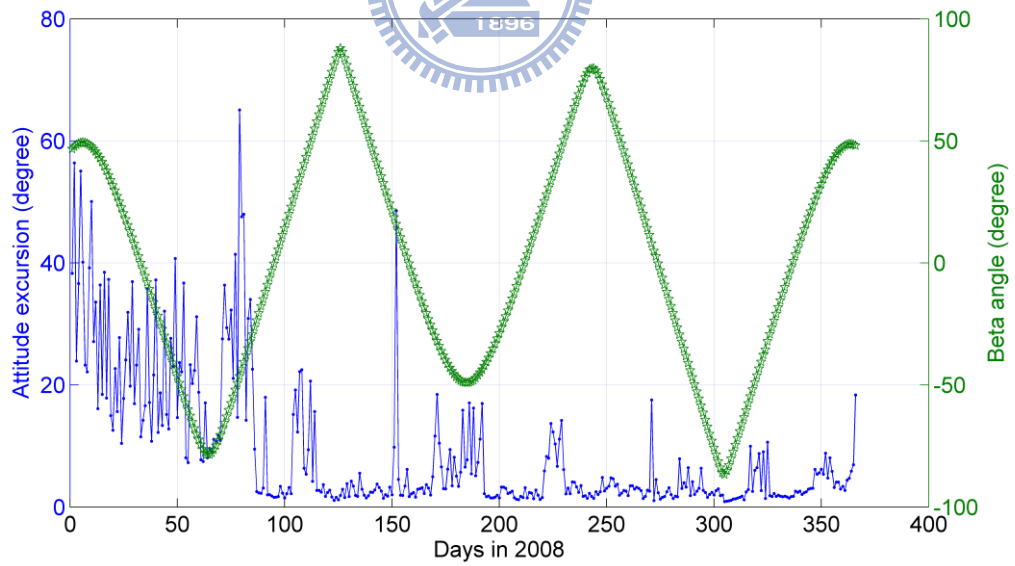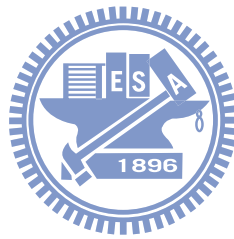


Fig. 5-10: Daily attitude excursion of each F3/C (a) FM1 (b) FM2 (c) FM3 (d) FM4 (e)

FM5 (f) FM6 in 2008

Table 5-2: The mean attitude excursion associated with Fig. 5-10

|  | FM1 | FM2 | FM3 | FM4 | FM5 | FM6 |
|---|---|---|---|---|---|---|
| Mean att. excursion | 8.49° | 3.24° | 3.56° | 3.60° | 4.09° | 9.10° |

# Сhapter 6

## Precise orbit determination for FORMOSAT-3/COSMIC

### 6.1 GPS ephemeris and clock correction products

In this section, we will demonstrate the POD of F3/C using PPP approach. Two approaches are available in Bernese 5.0 for POD with GPS: the reduced dynamic and kinematic approaches; see Švehla and Rothacher (2003) and Dach et al. (2007). We use undifferenced GPS phases for both approaches, which require high precision GPS satellite orbits and clocks (Bock et al. 2002 and 2004). Fig. 6-1 shows the flowchart of F3/C POD procedure. A priori orbit is first obtained using code observations, and such orbit is used for clock synchronization and outlier detection. Finally, the remaining observations are used for the orbit determination of F3/C. Hereafter, the reduced dynamic orbit is called the dynamic orbit.

---

**Input files**

GPS high-rate clock

GPS final orbit

Earth orientation parameter

LEO GPS observation

↓

Create of a priori orbit

Synchronize with GPS clock

Screen observation using a priori orbit

Detect outlier

↓

**Output**

Reduced dynamic orbit (6 Kelperian parameters and 9

dynamic parameter and pulses) or

Kinematic orbit

---
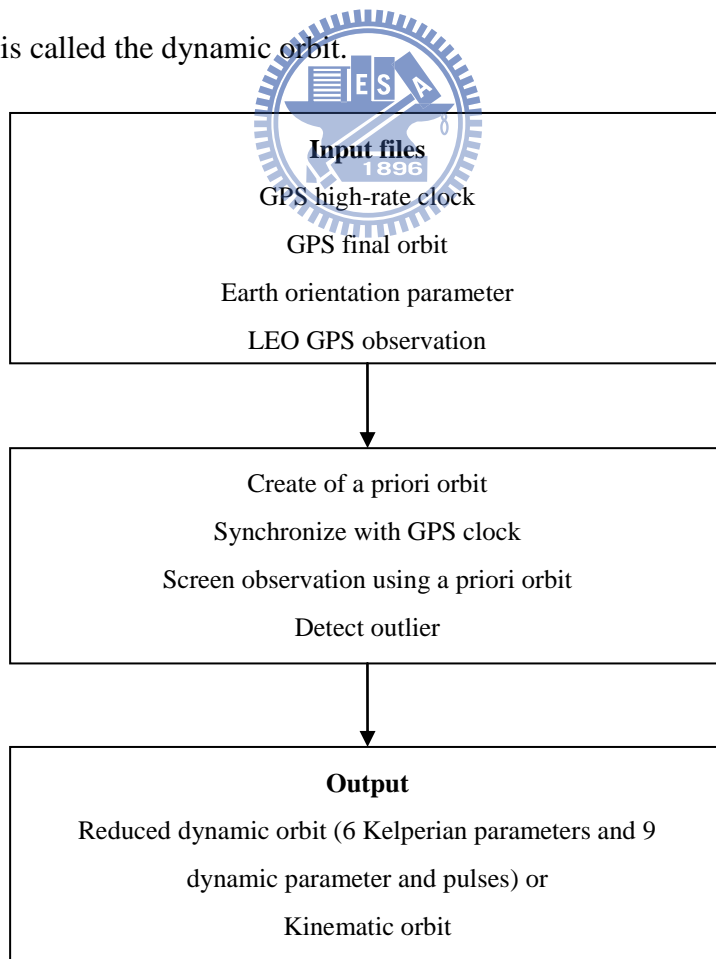
Fig. 6-1: Flowchart for POD procedure

The GPS ephemeris for the geodetic applications has been provided by IGS as early as 1994 (Kouba 2002). The various GPS orbit and HRC products from different analysis centers are combined into IGS final products using the weighting and quality control. The final GPS orbit is available about after 2 weeks and the position is presented with an accuracy of better than 5 cm at 15-minute interval in a SP3 format. The rapid product of GPS orbits can be available and reach an almost identical accuracy (< 5 cm) after 3 days. The GPS orbits in the final and rapid products are estimated for the central day of a 3-day long-arc analysis. However, for a NRT study, since 2004, IGS provides the product of ultra-rapid GPS orbit with 1 m prediction error. This orbit product contained the GPS clock with the code accuracy and the GPS orbit with an accuracy of 10 cm, which are updated four times per day within a latency of 3 hours (IGSCB 2004). Consequently, the ultra-rapid product is suggested for the application of differential positioning due to the insufficient accuracy of GPS clock correction (Montenbruck et al. 2005).

Currently, only four analysis centers are able to deliver the 30-s HRC, namely CODE, JPL, MIT and NRCan. As mentioned before, the products of CODE were used for POD of F3/C in this study and also in Švehla and Rothacher (2002), Jäggi et al. (2007) and Bock et al. (2009a). The products of CODE and IGS for GPS orbit and HRC are shown in Table 6-1 (Dach et al. 2007). The post-processing accuracy of LEO POD using PPP strategy primarily relies on the sampling interval of HRC. Montenbruck et al. (2005) demonstrated the use of the 5-minute HRC was not sufficient to achieve the high accuracy (cm level) POD of LEO with the 30-s GPS phase data. Additionally, CODE still provides another clock product, 5-s HRC, delivered since DOY 118, 2008. Bock et al. (2009b) demonstrated the significant improvement on the difference between dynamic and kinematic orbits for GRACE-A using 5-s HRC, compared with those using 30-s HRC. In order to be consistent with

the GPS data sampling interval, the linear interpolation of HRC is applied rather than a high-order polynomial interpolation due to the underlying random noise. The errors from the clock interpolation depend on the interval size of the consecutive clock data (Kouba 2002 and Zumberge and Gendt 2001). Fig. 6-2 shows the 1-day (DOY 209, 2008) residuals of FM6 using 30-s and 5-s HRC, respectively. The RMS value of the phase residuals is 1.74 cm using 30-s HRC, compared to 1.35 cm using 5-s HRC. A measurement error at a 4 mm level is introduced by the different HRC product for 1-day GPS data in this study case.

Table 6-1: A comparison of GPS orbit and clock products from CODE and IGS

| Orbit and clock types | Accuracy | Latency |
|---|---|---|
| CODE Ultra-rapid orbits | < 10 cm | Real-time |
| CODE Rapid orbits | < 5 cm | After 12 hours |
| CODE Final orbits | < 5 cm | After 5-11 days |
| CODE Rapid clock | 20-30 ps | After 12 hours |
| CODE Final clock | 15 ps | After 5-11 days |
| IGS Ultra-rapid orbits (pred) | ~ 10 cm | Real-time |
| IGS Ultra-rapid orbits (obs) | < 5 cm | After 3 hours |
| IGS Rapid orbits | < 5 cm | After 17 hours |
| IGS Final orbits | < 5 cm | After 13 days |
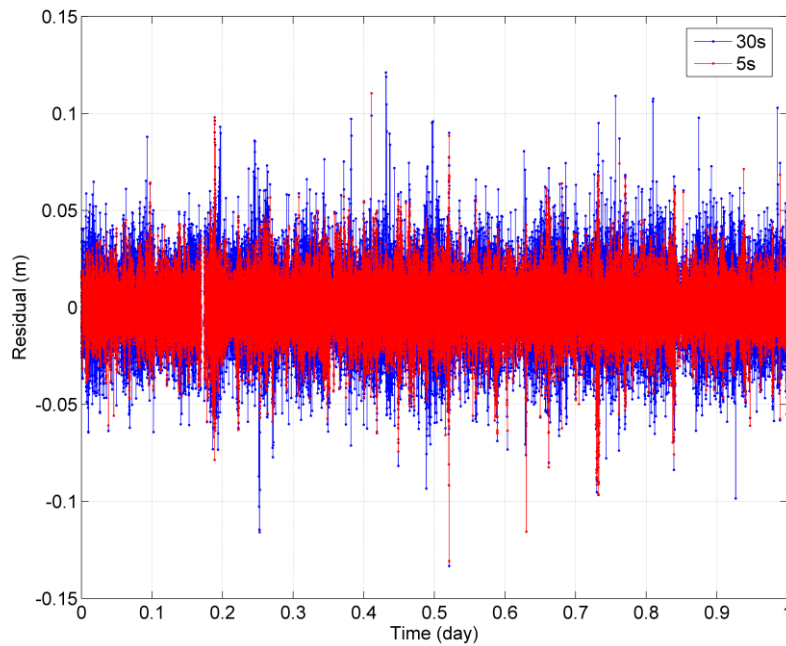
Fig. 6-2: 1-day phase residuals of FM6 using 30s (blue) and 5s (red) HRC

However, for the orbit determination of NRT LEO satellites using PPP, the precise GPS orbit and HRC products must be timely available. Since the accuracy of the NRT GPS clock correction was insufficient in IGS predicted orbit file, Bock et al. (2009b) estimated the NRT HRC by means of using IGS ultra-rapid orbit as a priori orbit. Additionally, the study also introduced the IGS ground network stations to refine the a priori orbit and simultaneously estimated the NRT HRC within a latency of less than 2-3 hours. Bock et al. (2009b) shows a significant improvement of the NRT orbit solutions, compared to the JPL orbit solution for GRACE-B solution using the NRT HRC. Therefore, the NRT HRC primarily depends on the accuracy of the GPS predicted orbit and the limitation of collecting timely the data from IGS ground network stations. Hauschild and Montenbruck (2009) estimated the NRT HRC based on Kalman filter strategy. The clock quality was assessed by estimating LEO orbit using different products from different analysis centers and also by RMS values of SISRE (Signal In Space Range Error) (Warren and Raquet 2003), postfit phase

residual and 3D position error. The above information can be helpful for the NRT

GPS-based POD for the upcoming COSMIC follow-on mission.

## 6.2 Reduced dynamic orbit determination

All perturbation in the equation of motion of a satellite in the inertial frame can

be expressed as (Dach et al. 2007)

$$\ddot{\mathbf{r}} = -GM \frac{\mathbf{r}}{r^3} + f_R(t, \mathbf{r}, \dot{\mathbf{r}}, p_1, ..., p_d) = f(t, \mathbf{r}, \dot{\mathbf{r}}, p_1, ..., p_d) \tag{6.1}$$

When determining the orbit of a satellite, we use the osculating elements of

Keplerian to define an initial state vector $\mathbf{r_0} = \mathbf{r}(a, e, i, \Omega, \omega, u_0)$ at the initial epoch

$t_0$. The parameters, $p_1...p_d$, in Eq. (6.1) are usually used to describe the

deterministically perturbing accelerometer acting on the satellite. However, those

parameters in the case of GPS satellites are usually associated with radiation pressure.

We assume that there are $n_p$ dynamic parameters, and the orbital parameterization can

be estimated by $n=6+n_p$ parameters. According to (Beutler et al. 1994), the radiation

model in Bernese can be estimated by (Dach et al. 2007)

$$\mathbf{a_{rpr}} = \mathbf{a_{ROCK}} + \mathbf{a_D} + \mathbf{a_Y} + \mathbf{a_X} \tag{6.2}$$

where $\mathbf{a_{ROCK}}$ is the radiation pressure model of ROCK 4 (GPS Block I satellites) and

ROCK42 (GPS Block II satellites). However, we only concern the $\mathbf{a_D}, \mathbf{a_Y}, \mathbf{a_X}$ terms and

they are written as below,

$$\mathbf{a_D} = (\mathbf{a_{D0}} + \mathbf{a_{DC}} \cdot \cos u + \mathbf{a_{DS}} \cdot \sin u) \cdot \mathbf{n_D} = D(u) \cdot \mathbf{n_D}$$
$$\mathbf{a_Y} = (\mathbf{a_{Y0}} + \mathbf{a_{YC}} \cdot \cos u + \mathbf{a_{YS}} \cdot \sin u) \cdot \mathbf{n_Y} = Y(u) \cdot \mathbf{n_Y} \qquad (6.3)$$
$$\mathbf{a_X} = (\mathbf{a_{Z0}} + \mathbf{a_{XC}} \cdot \cos u + \mathbf{a_{XS}} \cdot \sin u) \cdot \mathbf{n_X} = X(u) \cdot \mathbf{n_X}$$

where $\mathbf{a_{D0}}$, $\mathbf{a_{Y0}}$, $\mathbf{a_{X0}}$, $\mathbf{a_{DC}}$, $\mathbf{a_{YC}}$, $\mathbf{a_{XC}}$, $\mathbf{a_{DS}}$, $\mathbf{a_{YS}}$ and $\mathbf{a_{XS}}$, are the nine parameters of the radiation pressure model in Bernese,

$\mathbf{n_D}$ is the unit vector sun-satellite

$\mathbf{n_Y} = \dfrac{\mathbf{n_D} \times \mathbf{r}}{|\mathbf{n_D} \times \mathbf{r}|}$ is the unit vector along the spacecraft's solar panel axis

$\mathbf{n_X} = \mathbf{n_Y} \times \mathbf{n}_D$ is given by right-hand orthogonal rule

$D(u)$, $Y(u)$ and $X(u)$ are the total acceleration of radiation pressure in the direction $\mathbf{n_D}$,

$\mathbf{n_Y}$ and $\mathbf{n_X}$

$u$ is the argument of latitude at time $t$
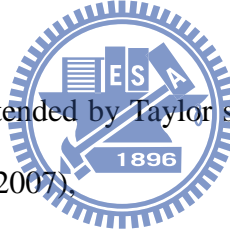
The true orbit $\mathbf{r}(t)$ can be extended by Taylor series with respect to the unknown parameters as below (Dach et al. 2007),

$$\mathbf{r}(t) = \mathbf{r_0}(t) + \sum_{i=1}^{n} \frac{\partial \mathbf{r_0}}{\partial p_i} \cdot (p_i - p_{i0}) \qquad (6.4)$$

where $\mathbf{r_0}(t)$ is a priori orbit, e.g., from code solutions, $n=6+d$ denoted the total number of orbit parameters, e.g., 6 initial state vector for position and velocity and $d$ dynamic parameters. Eq. (6.4) allows us to improve the a priori orbit using the phase solutions from second iteration instead of the code solutions and to improve the partial derivative of the a priori orbit with respect to unknown parameters (Jäggi et al. 2006). Therefore, we assume $p \in \{\mathbf{r}, \dot{\mathbf{r}}, p_1, ..., p_d\}$ as defined in Eq. (6.1) and the partial derivative of the a priori orbit with respect to the parameter $p$ is expressed by

$$\mathbf{Y_p} = \frac{\partial \mathbf{r_0}(t)}{\partial p} \qquad (6.5)$$

Eq. (6.6) is associated with the initial value problem and the variation equation. The expression can be written as

$$\ddot{\mathbf{Y}}_{\mathbf{p}} = \mathbf{A}_{3\times3} \cdot \mathbf{Y_p} + \mathbf{B}_{3\times3} \cdot \dot{\mathbf{Y}}_{\mathbf{p}} + (\frac{\partial \mathbf{f_R}}{\partial p}) \qquad (6.6)$$

where **A** and **B** are defined by

$$\mathbf{A} = \frac{\partial \mathbf{f_R}}{\partial \mathbf{r}}, \mathbf{B} = \frac{\partial \mathbf{f_R}}{\partial \dot{\mathbf{r}}} \qquad (6.7)$$

For 6 initial state vector, Eq. (6.6) is associated with the linear, homogeneous, second-order differential equation and can be solved with the initial value $\mathbf{Y_p} \neq 0$ and $\dot{\mathbf{Y}}_{\mathbf{p}} \neq 0$ using the numerical integration; for $\{p_1, ..., p_d\}$ in $\mathbf{f_R}$, Eq. (6.6) is solved with the initial value of zero due to the nonhomogeneous equation. Thus, the a priori orbit can be improved by the solution.

The dynamic approach in Bernese applies the pseudo-stochastic pulses model to absorb the non-gravitational effects on the spacecraft. The concept addresses that the use of the changes of the instantaneous velocity can be a kind of empirical parameters to improve the GPS orbit quality efficiently (Beulter et al. 1994). The pulses compensate the deficiencies from one-cycle-per-revolution, solar radiation pressure and other non-gravitational effects. Focusing on one pulse $\mathbf{v_i}$ at time $t_i$ in the predetermined direction $\mathbf{n}(t_i)$, the contribution of $p_i = \mathbf{v_i}$ in $\mathbf{f_R}$ of Eq. (6.1) may be expressed as (Jäggi et al. 2006)

$$\delta(t - t_i) \cdot \mathbf{n}(t) = \begin{cases} 1, & t = t_i \\ 0, & t \neq t_i \end{cases} \tag{6.8}$$

where $\delta(t)$ denotes Dirac's delta distribution. If $q_i$ does not explicitly depend on the velocity, the corresponding variation equation can be written as

$$\ddot{\mathbf{Y}}_{\mathbf{vi}} = \mathbf{A}_{\mathbf{3 \times 3}} \cdot \mathbf{Y}_{\mathbf{vi}} + \delta(t - t_i) \cdot \mathbf{n}(t) \tag{6.9}$$

Eq. (6.9) can be solved efficiently with the initial value of zero, but a drawback is that the improved orbit is discontinuous at time $t_i$ (Jäggi et al. 2006). Fig. 6-4 shows the difference between two dynamic orbits determined from two different force models in the along-track direction for FM1, DOY 360, 2008. One of two orbits was estimated using 12 sets of empirical parameters for one day arc and the other one was estimated using pseudo-stochastic pulses with a time resolution of 6 minutes. The difference shows the piecewise continuation resulting from the instantaneous velocity changes (pulses influence).
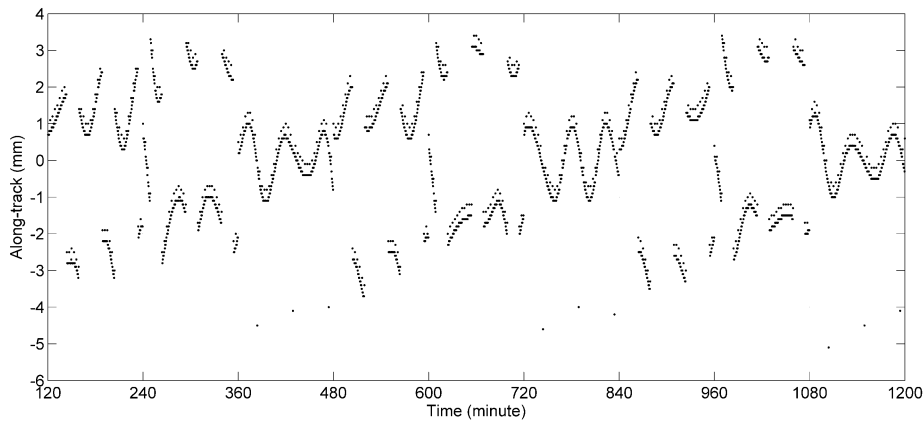


Fig. 6-3: Differences between two dynamic orbits determined from two different force modes in the along-track direction for FM1, DOY 360, 2008

In Bernese, the pseudo-stochastic pulses, characterizing instantaneous velocity changes at user-defined epoch in predetermined directions is a very powerful tool to improve the orbit quality. However, the result from the final parameter estimation leads to the discontinuity of the finial orbit (see Fig. 6-4), which may be removed by the use of Kalman filter (Dach et al. 2007). Furthermore, Jäggi et al. (2006) and Beutler et al. (2006) investigated the performance of different pseudo-stochastic parameters, such as instantaneous velocity changes (pulses), piecewise constant accelerations and continuous piecewise linear accelerations in the dynamic orbit determination. The options of pseudo-stochastic accelerations are not implemented in the official Bernese GPS software version 5.0.

All parameters of dynamic models for the satellites in Bernese are estimated in the module "GPSEST". These parameters include the 6 initial state vector, 9 solar radiation coefficients and three pseudo-stochastic pulses every 6 minutes in the radial, along-track and cross-track directions. Additionally, the other force models, such as solid, pole and ocean tides (IERS Conventions 2003), JPL planetary ephemeris DE200 and the earth gravity model GGM02S (Tapley et al., 2005), were used to integrate LEO satellite equations of motion in the module "ORBGEN".

PPP is a very efficient approach compared to that based on double-difference method requiring IGS ground stations in the GPS positioning. A large number of ambiguity parameters will be needed due to short LEO satellite arc and a large number of the very long baselines will be solved, when double-differenced carrier-phase measurements are involved (Švehla and Rothacher 2003).

## 6.3 Kinematic orbit determination

In the kinematic approach, satellite coordinates are estimated together with one GPS receiver clock parameter every epoch, as follows,

$$\mathbf{O(x)} = \mathbf{O(x^0)} + \frac{\partial \mathbf{O(x^0)}}{\partial \mathbf{x}} \mathbf{\Delta x} \qquad (6.10)$$

where $\mathbf{O}(x)$ denotes the real GPS measurement data, $\mathbf{O}(x_0)$ denotes the computed value with the initial value and $\mathbf{\Delta x}$ denotes the corrections of $\mathbf{x}$, with $\mathbf{x} = \mathbf{x^0} + \mathbf{\Delta}\mathrm{x}$. Vector $\mathbf{x}$ contains the coordinate $(x_i, y_i, z_i)$ at the epoch $t_i$ and receiver clock error $\delta t$. The solution of Eq. (6.10) can be solved by the least-squares method:

$$\mathbf{\Delta x} = \mathbf{(A^T W A)^{-1} A^T W (O(x) - O(x^0))} \qquad (6.11)$$

$$\mathbf{\Delta x} = \mathbf{(N)^{-1} A^T W (O(x) - O(x^0))} \qquad (6.12)$$
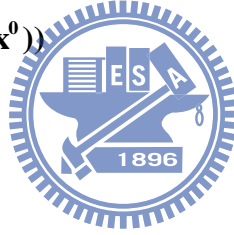
where $\mathbf{A} = \dfrac{\partial \mathbf{O(x^0)}}{\partial \mathbf{x}}$ is the design matrix and $\mathbf{W}$ denotes the weight matrix of phase observations. In general, the measured data of 24 hours exists 8640 epochs with 10-s sampling interval in a case of no data gap. Due to the fast changes of the tracked GPS geometry for LEO, the number of ambiguity parameters is about 400~500 over a 24-hour arc (see Fig. 4-15(a)). In addition to 400~500 ambiguity parameters, the epoch parameters, 3-dimension coordinates and 1 receiver clock error, are to be estimated. Therefore, the total number of parameters for the LEO kinematic positioning is about 4*8640+400=34960. With an average number of 7 observations per epoch for F3/C, the total number of GPS observations is about 7*8640=60480 (see table 4-1). Because about 35000 parameters are estimated in the normal equation

system, we can divide the estimated parameters into 2 parts, as follows. Let $\mathbf{X_1}=(x_1,x_2,\ldots\ldots x_n)$ contain the parameters of 3-dimension coordinates and 1 receiver clock error, and n=86400. Let $\mathbf{X_2}=(b_1,b_2,\ldots\ldots b_m)$ contain the ambiguity parameters, and m=400. According to Eq. (6.10), $\mathbf{A}$ can be partitioned into the partials of $\mathbf{X_1}$ and $\mathbf{X_2}$. Thus, the corresponding normal equation can be written as

$$\left(\frac{\partial \mathbf{O}}{\partial(\mathbf{X_1},\mathbf{X_2})}\right)^{\mathrm{T}}\mathbf{W}\left(\frac{\partial \mathbf{O}}{\partial(\mathbf{X_1},\mathbf{X_2})}\right)\cdot\begin{pmatrix}\Delta\mathbf{X_1}\\\Delta\mathbf{X_2}\end{pmatrix}=\left(\frac{\partial \mathbf{O}}{\partial(\mathbf{X_1},\mathbf{X_2})}\right)^{\mathrm{T}}\mathbf{W}\big(\mathbf{O}(\mathbf{X_1},\mathbf{X_2})-\mathbf{O}(\mathbf{X_1^0},\mathbf{X_2^0})\big)$$

(6.13)

where $\left(\dfrac{\partial \mathbf{O}}{\partial(\mathbf{X_1},\mathbf{X_2})}\right)$ can be replaced by $(\mathbf{A_1},\mathbf{A_2})$ and Eq. (6.13) leads to

$$\begin{pmatrix}\mathbf{A_1^T W A_1} & \mathbf{A_1^T W A_2}\\\mathbf{A_2^T W A_1} & \mathbf{A_2^T W A_2}\end{pmatrix}\cdot\begin{pmatrix}\Delta\mathbf{X_1}\\\Delta\mathbf{X_2}\end{pmatrix}=\begin{pmatrix}\mathbf{A_1^T W}(\mathbf{O}(\mathbf{X_1},\mathbf{X_2})-\mathbf{O}(\mathbf{X_1^0},\mathbf{X_2^0}))\\\mathbf{A_2^T W}(\mathbf{O}(\mathbf{X_1},\mathbf{X_2})-\mathbf{O}(\mathbf{X_1^0},\mathbf{X_2^0}))\end{pmatrix}$$

(6.14)

Using $\mathbf{N_{11}}=\mathbf{A_1^T W A_1}$, $\mathbf{N_{22}}=\mathbf{A_2^T W A_2}$, $\mathbf{l_1}=\mathbf{A_1^T W}(\mathbf{O}(\mathbf{X_1},\mathbf{X_2})-\mathbf{O}(\mathbf{X_1^0},\mathbf{X_2^0}))$ and $\mathbf{l_2}=\mathbf{A_2^T W}(\mathbf{O}(\mathbf{X_1},\mathbf{X_2})-\mathbf{O}(\mathbf{X_1^0},\mathbf{X_2^0}))$ leads to

$$\begin{pmatrix}\mathbf{N_{11}} & \mathbf{N_{12}}\\\mathbf{N_{21}} & \mathbf{N_{22}}\end{pmatrix}\cdot\begin{pmatrix}\Delta\mathbf{X_1}\\\Delta\mathbf{X_2}\end{pmatrix}=\begin{pmatrix}\mathbf{l_1}\\\mathbf{l_2}\end{pmatrix}$$

(6.15)

Since the GPS phase measurements are used, phase ambiguities are common parameters in the least-square adjustment and are estimated as common parameters. The epoch-wise parameters are pre-eliminated from the normal equation system. Pre-elimination of ambiguity parameters is a basic procedure of the normal equation

in least-squares adjustment. The sub-matrices of the inverse of the normal matrix corresponding to the partition in Eq. (6.15) can be found in Koch (1987, p. 39). As such, we have

$$\Delta\mathbf{X_1} = \mathbf{N_{11}^{-1}}(\mathbf{l_1} - \mathbf{N_{12}}\Delta\mathbf{X_2})$$ (6.16)

and $\Delta\mathbf{X_2}$ can be expressed as

$$\Delta\mathbf{X_2} = (\mathbf{N_{22}} - \mathbf{N_{21}}\mathbf{N_{11}^{-1}}\mathbf{N_{12}})^{-1}(\mathbf{l_2} - \mathbf{N_{21}}\mathbf{N_{11}^{-1}}\mathbf{l_1})$$ (6.17)

which is then backward substituted to Eq. (6.16) to obtain the solution of $\Delta\mathbf{X_1}$. Thus, the covariance of $\Delta\mathbf{X_1}$ and $\Delta\mathbf{X_2}$ are given by

$$
\begin{aligned}
\begin{pmatrix} \mathbf{N_{11}} & \mathbf{N_{12}} \\ \mathbf{N_{21}} & \mathbf{N_{22}} \end{pmatrix}^{-1} &= \begin{pmatrix} \mathbf{Q_{11}} & \mathbf{Q_{12}} \\ \mathbf{Q_{21}} & \mathbf{Q_{22}} \end{pmatrix} \\
&= \begin{pmatrix} \mathbf{N_{11}^{-1}} + \mathbf{N_{11}^{-1}}\mathbf{N_{12}}(\mathbf{N_{22}} - \mathbf{N_{21}}\mathbf{N_{11}^{-1}}\mathbf{N_{12}})^{-1}\mathbf{N_{21}}\mathbf{N_{11}^{-1}} & -\mathbf{N_{11}^{-1}}\mathbf{N_{12}}(\mathbf{N_{22}} - \mathbf{N_{21}}\mathbf{N_{11}^{-1}}\mathbf{N_{12}})^{-1} \\ -(\mathbf{N_{22}} - \mathbf{N_{21}}\mathbf{N_{11}^{-1}}\mathbf{N_{12}})^{-1}\mathbf{N_{21}}\mathbf{N_{11}^{-1}} & (\mathbf{N_{22}} - \mathbf{N_{21}}\mathbf{N_{11}^{-1}}\mathbf{N_{12}})^{-1} \end{pmatrix}
\end{aligned}
$$ (6.18)

Since the kinematic solution are determined epoch-wise, rather than using the force constrains imposed on the dynamic solution, the satellite trajectory from the kinematic solution primarily depends on the number of visible GPS satellites and therefore is less smooth than that from the dynamic solution. An orbit accuracy of 1-3 cm was demonstrated for CHAMP and GRACE satellites based on the kinematic approach (Švehla and Rothacher, 2004 and 2005a). Additionally, kinematic POD is extremely sensitive to the GPS receiver performance. In the case of missing phase

data or insufficient number of GPS measurements, the kinematic orbit may have missing epochs, gaps or spikes when the tracking geometry is poor. This is the main problem with the kinematic POD of the F3/C mission where GPS antenna FOV is considerably reduced. The F3/C POD antenna boresight vector is not zenith pointing as in the case of CHAMP and GRACE missions, but it is tilted by 75° towards the flight direction (Figs. 3-2). As a final note, for gravity application of F3/C kinematic orbits, we produce a 30-h F3/C orbit arc which is truncated to a 24-hour arc (a GPS day from 0h to 24h). More about the kinematic POD application for the gravity field determination can be found in Švehla and Rothacher (2005a) and Hwang et al. (2008).

### 6.4. Effects of PCV and COM on F3/C orbits

In this section, the effects of COM and PCV on F3/C orbits will be addressed using F3/C GPS measurements and numerical examples.
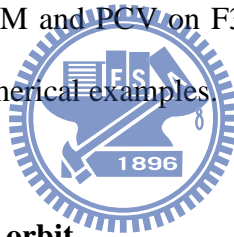
### 6.4.1 Effect of satellite COM on orbit

To inspect the impact of the satellite COM variation on the F3/C orbit determination, we applied a 2 cm bias to the satellite COM (Table 2) in the spacecraft Z direction. Table 6-2 (a) shows the RMS differences between the orbit components with and without the 2 cm bias for the cases of kinematic and dynamic orbits and satellite FM5 on Day 216, 2006. Since the spacecraft Z direction is almost aligned with the radial direction, a 2-cm bias will be theoretically propagated to the radial direction. However, this is not the case for the result given in Table 6-2 (a). Aside from the ~2-cm difference in the radial direction, there is still a ~2-cm difference in along-track direction and the difference in cross-track direction is zero as expected. Consequently, the 3-dimensional RMS differences exceed 3 cm. Apparently, the given bias (2 cm) has been amplified during the orbit determination. Possible reasons of the

amplification are: (1) the antenna of F3/C is not in the zenith direction, producing multi-path effects and other noises that are aliased into the given bias in Z, (2) GPS satellite geometry is weak, and (3) the attitude control (in this example) is not proper and subsequently affects the transformation of the given bias to the correct directions. For comparison, we applied a 1-cm bias to the COM of GRACE-B satellite (Day 233, 2003) in the spacecraft Z direction and Table 6-2 (b) shows the RMS differences between the GRACE orbits with and without such a bias. As seen in Table 6-2 (b), there is a dominant 1-cm difference in the radial direction and sub-cm (but non-zero) differences in other two directions. The three-dimensional RMS difference is about 1 cm, which is close to the given bias. This example highlights that in order not to degrade the orbit accuracy of F3/C, it is important to determine precisely the COMs for all F3/C satellites, as carried out in Section 3.2.
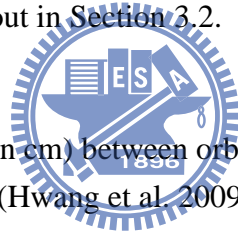
Table 6-2: RMS differences (in cm) between orbits with and without COM bias (Hwang et al. 2009)

(a) FM5 (2 cm bias in spacecraft Z)

|                | radial | Along-track | Cross-track | Total |
|----------------|--------|-------------|-------------|-------|
| Dynamic orbit  | 2.90   | 1.80        | 0.00        | 3.41  |
| Kinematic orbit| 2.12   | 2.12        | 0.00        | 3.00  |

(b) GRACE-B (1 cm bias in spacecraft Z)

|                | radial | Along-track | Cross-track | Total |
|----------------|--------|-------------|-------------|-------|
| Dynamic orbit  | 1.02   | 0.29        | 0.17        | 1.07  |
| Kinematic orbit| 1.00   | 0.30        | 0.57        | 1.12  |

## 6.4.2 Effect of PCV on orbit

PCV of a receiver antenna is a function of GPS satellite zenith angle and azimuth (Leick, 2004, p. 234) and here we show its impact on the F3/C orbit determination. Table 6-3 (a) and (b) lists the RMS overlap orbit differences (5 h) with and without PCV and the difference between kinematic orbits (with and without PCVs) and dynamic orbits (with and without PCVs), respectively, using GPS data of FM5 from Day 214 to 220, 2006. In the case of kinematic orbit, the improved accuracy due to PCV is at the sub-cm level; for dynamic orbit, that is at the sub-mm level. Thus, the improvements for dynamic and kinematic orbits due to PCV are different. In fact, the estimation of pseudo-stochastic pulses may absorb the slight PCV effect and thus, PCV effect has the smaller sensitivity in dynamic solutions. The outcome from table 6-3 shows the PCV data from the anechoic chamber test indeed have the improvements on the orbit accuracy for both dynamic and kinematic cases, and will be used for all F3/C orbit determinations.
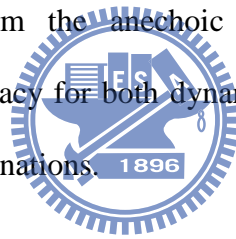
Table 6-3: RMS overlap differences of orbits (in cm) with and without PCV (FM5, Day 214 to 220, 2006 (Hwang et al. 2009)

(a)

| PCV | Kinematic orbit | Dynamic orbit |
| --- | --- | --- |
| With | 2.37/3.00/2.17[1] | 2.39/1.96/1.05 |
| Without | 2.80/3.23/2.40 | 2.43/2.02/1.12 |

[1]radial, along-track and cross-track

(b)

| PCV | Kinematic-Kinematic | Dynamic-Dynamic |
| --- | --- | --- |
| With-Without | 1.05/1.11/1.05 | 0.494/0.626/2.06 |

## 6.5 **Analysis of phase residual**

As mentioned in Chapter 4, the quality of GPS data was analyzed via code multipath, IOD and cycle slips. In this section, $L_C^3$ phase residuals associated with dynamic orbit determination were used to assess the quality of GPS data. Fig. 6-5 (a) and (b) shows the phase residuals of FM3 and GRACE-A with respect to elevation angle and azimuth from the dynamic orbit determination. The phase residuals of FM3 range from -0.2 to 0.2 m in the antenna frame and those of GRACE-A range from -0.06 to 0.04 m. In Fig. 6-5(a) and (b), the different patterns of distributions of phase residuals are due to the different antenna configurations on the F3/C and GRACE-A satellites. Due to the FOV of the F3/C GPS antenna (120°), there is a void zone of GPS signals from azimuths 120° to 240° in the antenna frame, as shown in Fig. 6-5 (a). For both FM3 and GRACE-A, relatively large phase residuals occur at low or even negative elevation angles. The RMS value of the phase residuals of FM3 is 2.71 cm, compared to 0.8 cm of GRACE-A.

(a)



(b)
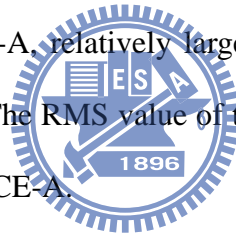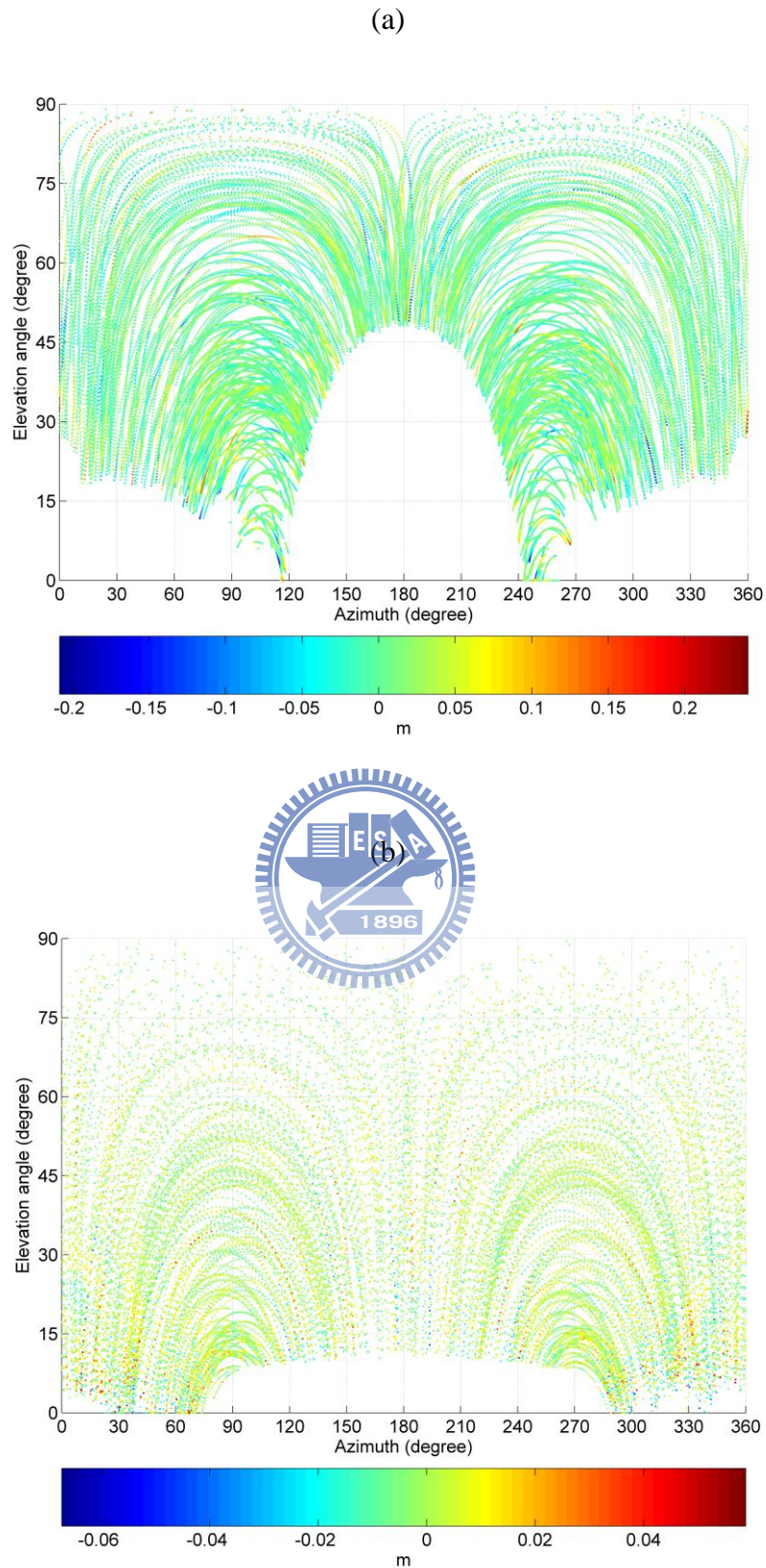


Fig. 6-4: Phase residuals (for one day) from the dynamic orbit determination for (a) FM3 and (b) GRACE-A, in different color scales

The standard error of unit weight was used to assess the overall quality phase observables for the six F3/C satellites over 300 days, starting from DOY 100, 2007. The definition of a standard error of unit weight was computed as

$$\hat{\sigma}_0 = \sqrt{\frac{\mathbf{V^T PV}}{\beta}}$$

(6.19)

where $\mathbf{V}$ denotes the phase-residual vector and $\mathbf{P}$ denotes the weight matrix of phase observables, $\beta$ is the degree of freedom in the least-squares parameter estimation associated with the orbit determination. Here we used a uniform weight (unitless) for all phase observables. Fig. 6-6 shows the distribution of the standard errors for FM1 to FM6, and Table 6-4 shows the average standard errors over 300 days. There are two possible reasons for the long data gaps in Fig. 6-6: (a) few and/or poor GPS observations exist in these gaps, and (b) poor attitude control disables POD (Hwang et al. 2009). The variations of the standard errors of FM5 and FM6 are small, in comparison to those for other satellites of F3/C. The F3/C satellites contain less observations than GRACE-A; on average, FM2 and FM4 contain about 30000 observations daily, compared to 60000 of GRACE-A. The standard error of FM3 is the largest (4.37 cm), followed by FM5 (2.41 cm). FM6 has the lowest standard error of 1.80 cm. It is not clear why the variations for FM5 and FM6 are smaller. Perhaps the GPS signal strengths and attitude controls of FM5 and FM6 were good during this period of time. The average standard error of FM1, FM2 and FM4 is about 3.00 cm. GRACE-A has the least standard error of 0.99 cm. According to Comp and Axelrad (1998), multipath effects of phases may range from few mm to few cm. If systematic errors such as clock error, ionospheric delay, and ambiguity parameter are properly modeled in the least-squares estimation of orbit parameters, the phase residuals in Eq.

(6.19) will largely come from the multipath effect of phase. Under this condition, the RMS value of multipath effect is roughly of the order of the standard error defined in Eq. (6.19). As such, F3/C's multipath effect of phase is of the order of few cm.
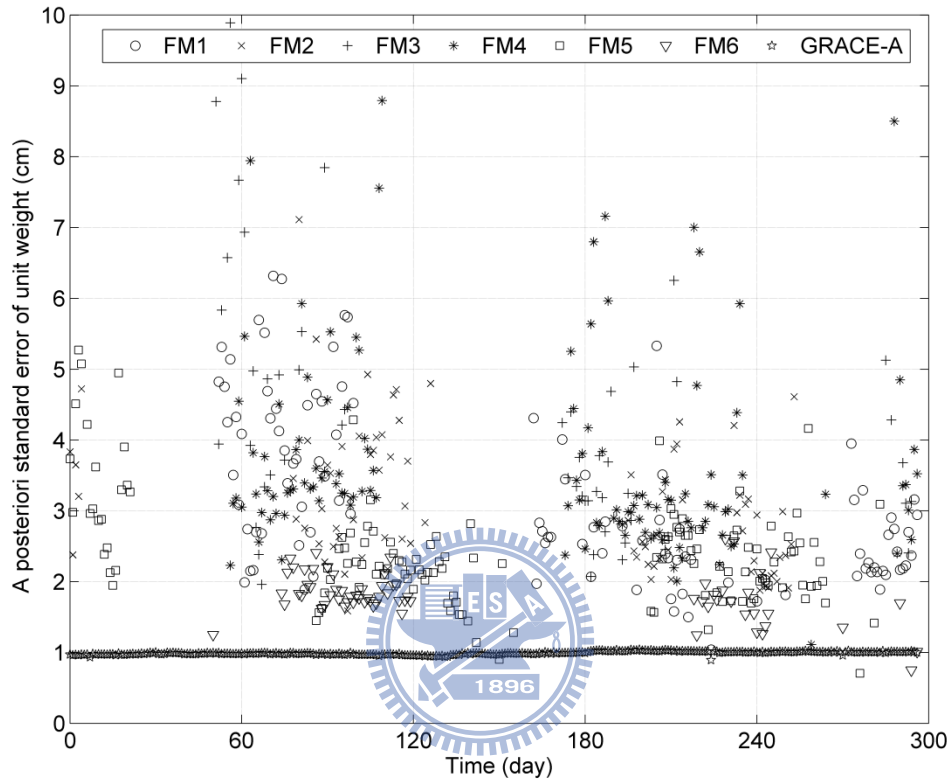


Fig. 6-5: The a posteriori standard error of unit weight for F3/C satellites, beginning from DOY 100, 2007

Table 6-4: Average daily number of GPS observations (0.1 Hz) and a posteriori standard error of unit weight (cm) for six F3/C satellites over 300 days since DOY 100, 2007

|  | FM1 | FM2 | FM3 | FM4 | FM5 | FM6 | GRACE-A |
|---|---|---|---|---|---|---|---|
| Daily number | 14860 | 30450 | 27480 | 32020 | 14260 | 25110 | 57640 |
| Standard error | 3.22 | 3.11 | 4.37 | 3.70 | 2.41 | 1.80 | 0.99 |

## 6.6 Quality assessment based on difference between dynamic and kinematic orbits

The difference between the dynamic orbit and kinematic (called dynamic–kinematic difference) orbit over the same arc can be used to evaluate the quality of GPS data. The degree of consistency between dynamic and kinematic orbits is an indirect way of checking the quality of F3/C GPS data. In addition, the dynamic orbits will be smoother than kinematic orbits. However, kinematic orbits mainly depend on the quality of GPS observations and the number of GPS observations (Bock 2004). This means that a bad kinematic orbit solution leads to a large dynamic–kinematic orbit difference. Therefore, the dynamic–kinematic orbit difference can be an indirect indicator of GPS data quality. Fig. 6-7 shows the daily RMS values of the dynamic–kinematic orbit differences in the earth-fixed system over 300 days, and Table 4 summarizes the statistics of the differences. The RMS values of dynamic–kinematic differences for F3/C and GRACE-A are about 10 cm and 2 cm, respectively. If the quality of GPS data is sufficiently good, one would expect an RMS dynamic–kinematic difference of 3 cm for F3/C, which is based on the overlapping analysis (Hwang et al. 2009). The 10 cm dynamic–kinematic difference for F3/C is significantly larger than the 3-cm overlapping difference, and this discrepancy is mainly caused by bad kinematic orbits, which are in turn due to frequent cycle slips, large multipath effects, small number of tracked GPS satellites, plus poor attitude control, antenna phase center variation and the poor geometry of tracked GPS satellites (Hwang et al. 2009). The 2 cm dynamic–kinematic difference for GRACE-A is close to the 1-cm overlapping difference. In addition, for F3/C satellites the differences in the xyz components are quite consistent, while for GRACE-A the z-component is slightly larger than the other two components.
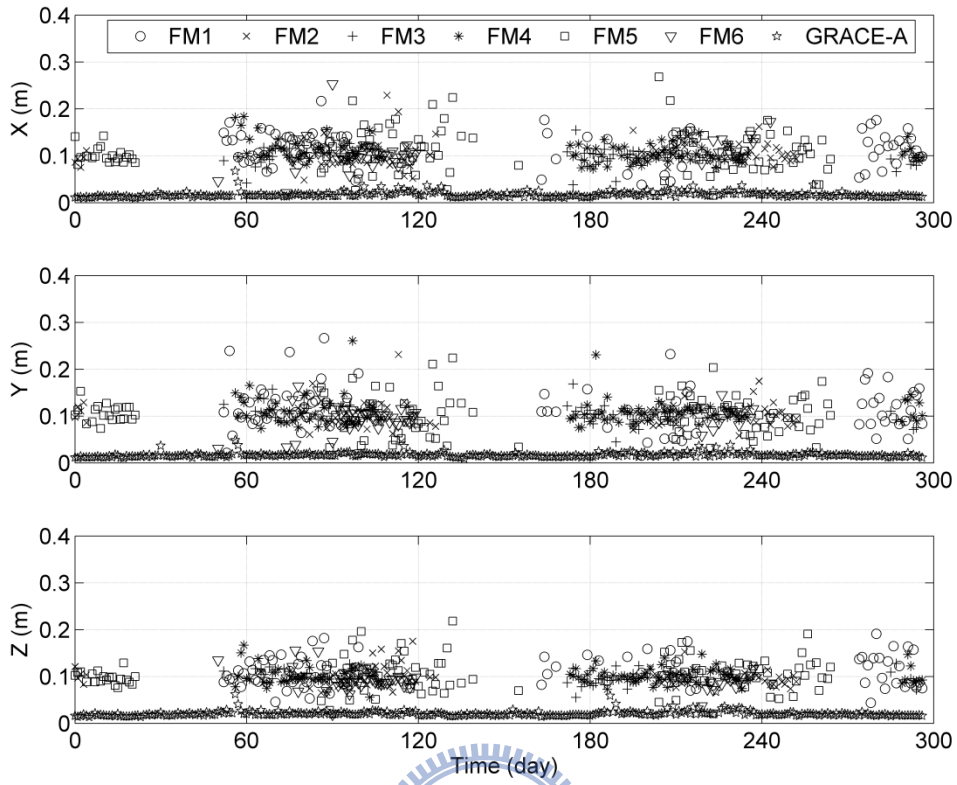
Fig. 6-6: RMS differences in the Earth-fixed system XYZ between kinematic and dynamic orbits, since DOY 100, 2007

Table 6-5: Statistics of daily RMS values (in cm) of the dynamic - kinematic orbit differences in the earth-fixed system over 300 days since DOY 100, 2007

| Satellite | X | Y | Z |
|-----------|-------|-------|-------|
| FM1 | 11.60 | 11.72 | 11.17 |
| FM2 | 10.59 | 10.34 | 9.89 |
| FM3 | 9.63 | 10.34 | 9.78 |
| FM4 | 10.83 | 10.86 | 10.11 |
| FM5 | 10.94 | 10.31 | 10.46 |
| FM6 | 10.66 | 9.55 | 9.04 |
| GRACE-A | 1.76 | 1.70 | 2.09 |

**6.7 Assessment of orbit accuracy**

**6.7.1 Assessment based on orbit overlaps**

Since F3/C satellites are not equipped with laser retro-reflector arrays or DORIS antennae for an independent orbit determination other than GPS, an external assessment of orbit accuracy is not possible. Therefore, orbit overlaps will be used to achieve the assessment of orbit accuracy. Two options would be used for the orbit overlap. One is to use the overlap epoch at the beginning and end of the 24-h arc, implying that different GPS measurements have been used for different arcs. Alternatively, a 6-h overlap of two 30-h arcs (3 h at the start and the end of an orbit arc) can be used to assess internal orbit accuracy because the same GPS measurements are used for both arcs (Kang et al., 2006). However, the overlap epoch at the end point of a 24-h arc will yield an imperfect estimation for the internal accuracy because of the edge effect (Kang et al., 2006). A 6-h overlap arc can be truncated to a 5-h arc (removing 30 minutes at the beginning and the end of the 6-h arc) to reduce the edge effect.

Tables 6-6 and 6-7 show the RMS overlap differences based on the full 6-h (with edge effect) and 5-h (without edge effect) orbit overlaps for all six F3/C satellites from the dynamic and kinematic orbits, based on data from Day 214 to 239, 2006. The original sampling interval of GPS data is 5 s. The 5-s GPS data can be decimated and filtered to a coarser sampling interval to improve GPS data quality. Normally, a coarser sampling interval than 5 s is needed in gravity recovery using orbital perturbations; e.g., CHAMP, at an altitude of 454 km, uses a 30-s sampling interval. As an example, Tables 6-6 (b) and 6-7 (b) shows the RMS overlap differences using a 30-s sampling interval (5-h overlaps), which are a few mm smaller than the 5-s overlap differences.

Table 6-6: RMS overlap differences of orbits (in cm) based on 5-h and 6-h overlaps using kinematic approach for 25 days (Hwang et al. 2009)

**(a)** 5 s sampling interval

|     | Radial | | Along-track | | Cross-track | |
| --- | --- | --- | --- | --- | --- | --- |
|     | 5 h | 6 h | 5 h | 6 h | 5 h | 6 h |
| FM1 | 2.49 | 2.70 | 2.86 | 2.99 | 2.69 | 3.13 |
| FM2 | 2.62 | 2.69 | 2.50 | 2.56 | 2.70 | 3.17 |
| FM3 | 2.96 | 3.22 | 3.73 | 3.76 | 4.18 | 4.33 |
| FM4 | 3.33 | 3.35 | 3.23 | 3.25 | 4.20 | 4.34 |
| FM5 | 2.49 | 2.58 | 2.62 | 2.77 | 3.50 | 3.86 |
| FM6 | 3.40 | 3.43 | 3.19 | 3.58 | 4.71 | 4.79 |

**(b)** 30 s sampling interval (5 h)

|     | Radial | Along-track | Cross-track |
| --- | --- | --- | --- |
| FM1 | 2.51 | 1.85 | 2.28 |
| FM2 | 2.06 | 1.89 | 2.04 |
| FM3 | 2.38 | 3.08 | 3.52 |
| FM4 | 2.59 | 2.65 | 3.51 |
| FM5 | 1.87 | 2.10 | 2.87 |
| FM6 | 2.64 | 3.08 | 4.17 |

Table 6-7: RMS overlap differences of orbits based (in cm) on 5-h and 6-h overlaps using dynamic approach for 25 days (Hwang et al. 2009)

**(a)** 5 s sampling interval

|     | Radial | | Along-track | | Cross-track (cm) | |
| --- | --- | --- | --- | --- | --- | --- |
|     | 5-h | 6-h | 5-h | 6-h | 5-h | 6-h |
| FM1 | 2.68 | 2.86 | 2.70 | 3.07 | 2.81 | 3.19 |
| FM2 | 2.37 | 2.42 | 2.29 | 2.40 | 2.05 | 2.10 |
| FM3 | 2.67 | 2.72 | 2.85 | 2.88 | 3.05 | 3.17 |
| FM4 | 2.92 | 3.00 | 3.27 | 3.32 | 3.23 | 3.29 |
| FM5 | 2.35 | 2.58 | 2.40 | 2.43 | 3.14 | 3.16 |
| FM6 | 2.65 | 2.66 | 2.51 | 2.57 | 3.35 | 3.44 |

**(b)** 30 s sampling interval (5 h)

|     | Radial | Along-track | Cross-track |
| --- | --- | --- | --- |
| FM1 | 2.62 | 2.23 | 2.74 |
| FM2 | 1.83 | 1.63 | 1.50 |
| FM3 | 2.45 | 2.45 | 2.62 |
| FM4 | 2.25 | 2.77 | 2.79 |
| FM5 | 1.98 | 2.21 | 2.99 |
| FM6 | 2.10 | 2.06 | 2.86 |

The internal accuracy assessment (Tables 6-6 and 6-7) based on orbit overlaps indicates a 2-3 cm noise level (excluding systematic errors), which is less precise than the 1-2 cm orbit consistency of kinematic and dynamic orbits for GRACE satellites obtained by Švehla and Rothacher (2005b), who used exactly the same software as in this paper. We believe that the slightly worse F3/C orbit accuracy is mainly due to the non-ideal antenna orientation on the satellite body and number of tracked GPS satellites. A noise reduction in the kinematic orbit could be achieved by means of the normal point technique or some other smoothing technique, which is particularly useful for gravity recovery. Internal orbit accuracy obtained in this paper reflects only consistency between orbit overlaps and consistency between dynamic and kinematic orbits. Any remaining systematic errors in the orbits can only be detected by a comparison with external tracking data such as SLR. For gravity field recovery based on F3/C kinematic orbits, possible systematic errors in the orbit can be reduced by a suitable mathematic model in the estimation of gravity field. For example, most orbit errors contain components at the one- or two-CPR frequency bands, which can be effectively absorbed by some empirical error models, see, e.g., Colombo (1984) and Balmino (1994).

### 6.7.2 Comparison with UCAR and WHU orbits

Two "external" comparisons were implemented to see if systematic errors existed in our POD. UCAR determines the F3/C dynamic orbits using Bernese 5.0 based on IGS Ultra-Rapid predicted GPS orbits and precise 30-s NRT HRC. As mentioned in Section 6.1, the ultra-rapid GPS orbits have an accuracy of about 10 cm, compared to the 3-4 cm accuracy of the final orbits. UCAR's mission is to support real-time atmospheric application of F3/C based on NRT orbit solutions. Wuhan University (WHU) determines the F3/C dynamic orbits using the software "PANDA"

(Liu, and Ge, 2003). PANDA uses undifferenced GPS phases (as in this paper) and the final IGS GPS ephemeris to compute the dynamic orbit which is constrained with the atmospheric drags "DTM 94" model and two empirical parameters along radial, along-track and cross-track directions are estimated every 90 minutes. Table 6-8 compares our post-processed dynamic orbits with those from UCAR (near real-time) and Wuhan University (WHU, post-processed) for FM5 from Day 216 to 218, 2006. The NCTU-UCAR and NCTU-WHU orbit differences are both at the 10 cm level per component, with the NCTU-WHU orbit differences being smaller. The larger NCTU-WHU orbit differences for the case of FM4 in Table 6-8 are due to the fact that PANDA cannot properly remove anomalous observations of FM4 (GPS observables and attitudes). (note that the NCTU-UCAR orbit differences for FM4 are normal). The fact that the NCTU-UCAR orbit differences are larger than NCTU-NCTU orbit differences (Table 6-7) highlights the importance of using precise GPS ephemerides and HRC information for orbit determination of LEO to cm accuracy. The reason of the 10-cm difference between the NCTU and WHU orbits is yet to be investigated, but we believe the major cause is the different approaches of modeling satellite perturbing forces

Table 6-8: RMS orbit differences (in cm) between NCTU and UCAR and between NCTU and WHU, Days 216 to 218, dynamic orbit

| Satellite | NCTU-UCAR | NCTU-WHU |
|-----------|-----------|----------|
| FM1 | 13.5 / 14.3 / 18.5[1] | 8.3 / 8.2/ 11.6 |
| FM2 | 9.7 / 9.0 / 6.5 | 6.6 / 6.5 / 5.5 |
| FM3 | 9.8 / 10.0 / 7.2 | 5.6/ 5.5 / 5.7 |
| FM4 | 10.7 / 11.7 / 13.2 | 14.7 / 18.2 / 8.8 |
| FM5 | 10.8 / 11.2 / 10.3 | 9.3 / 11.4 / 9.4 |
| FM6 | 9.9 / 11.5 / 9.7 | 7.5 / 7.4/ 5.8 |

[1]radial, along-track and cross-track

# Chapter 7

# Attitude control effect on orbit determination and quantification of attitude error

## 7.1 Effect of attitude error and choice of attitude data

In this section, the effect of attitude error will be experimented on the orbit determination of F3/C using observed and nominal attitude. As previously stated nominal attitudes are determined by satellite position and velocity vectors, and this capability is implemented in Bernese 5.0. As an example, Fig. 7-1 shows observed attitudes of FM5 from Day 214 to 220, 2006 and Table 7-1 shows the statistics. The yaw angles oscillate more rapidly than other two angles, ranging from -54.5° to 71.3°. There are several places where abrupt changes of attitudes occur, and this is due to the effect of the sun sensors when the satellite is entering and exiting the eclipse, as stated in Chapter 5. Because the mass of F3/C satellite is small (62 kg) compared to that of a GRACE satellite (480 kg), exertion of attitude control will produce large dynamics of the spacecraft, leading to degraded GPS observations and poor transformation between the spacecraft coordinate system and the inertial coordinate system.

Fig. 7-2 shows the differences in orbits using observed and nominal attitudes. The RMS orbit differences are 11 and 3 cm in the dynamic and kinematic orbit cases, respectively, with biases being nearly zero. The orbit differences are highly correlated with the observed attitudes (Fig. 7-1). Large differences occur when there are no observed attitudes and when the observed attitudes are anomalous. This example suggests that attitude has a great impact on the orbit accuracy.

Table 7-2 shows RMS overlap differences (5 h, see Chapter 6) using observed and nominal attitudes for FM5 orbits from Day 214 to 220, 2006. For the dynamic orbit, use of nominal attitudes leads to smaller overlap differences. For the kinematic

orbit, the observed and nominal attitudes produce virtually the same overlap differences. This result is consistent with that given by Neumayer et al. (2005), who argue that nominal attitudes are mostly free from anomalous values and can fill the gaps due to missing attitude observations.
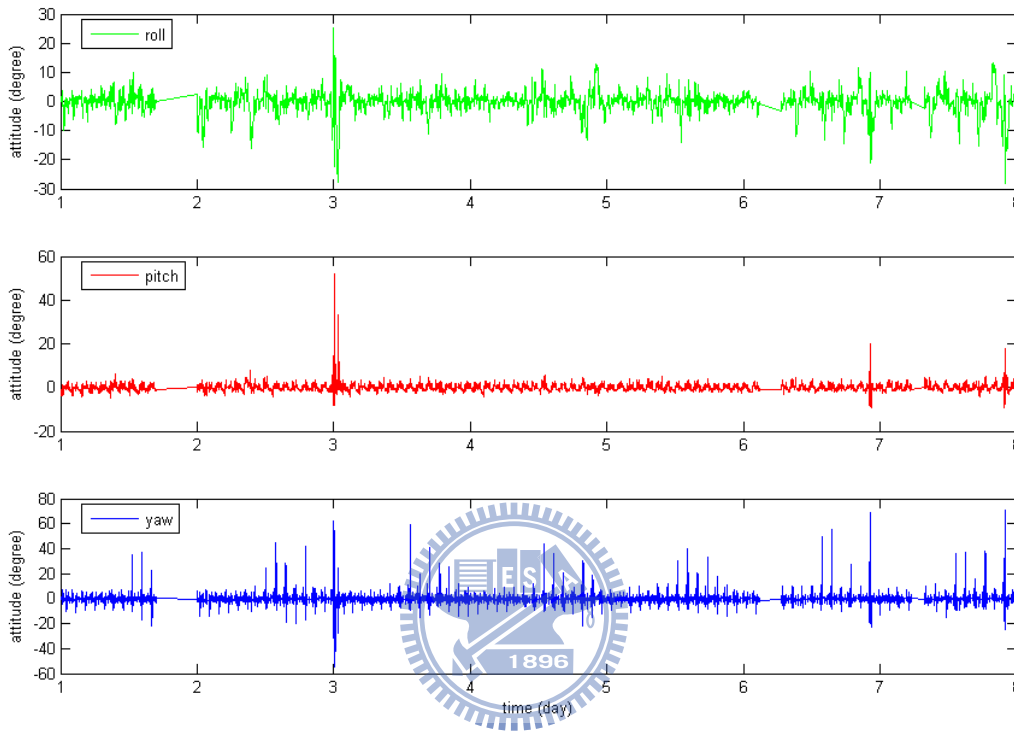


Fig. 7-1: Observed attitudes of FM5 from Day 214 to 220, 2006 (Hwang et al. 2009)

Table 7-1: Statistics of observed attitudes (in degree), FM5, Day 214 to 220, 2006 (Hwang et al. 2009)

|      | Roll | Pitch | Yaw   |
|------|------|-------|-------|
| Min  | -28  | -9.3  | -54.5 |
| Max  | 25   | 51.7  | 71.3  |
| RMS  | 3.7  | 1.7   | 4.5   |

(a)    Dynamic orbit
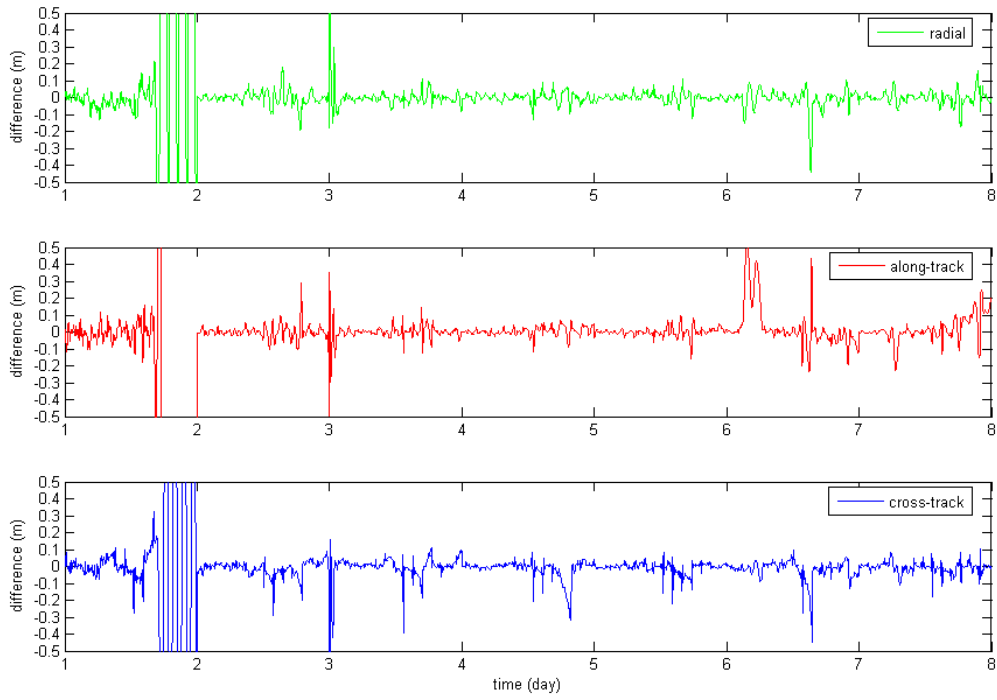


(b) Kinematic orbit
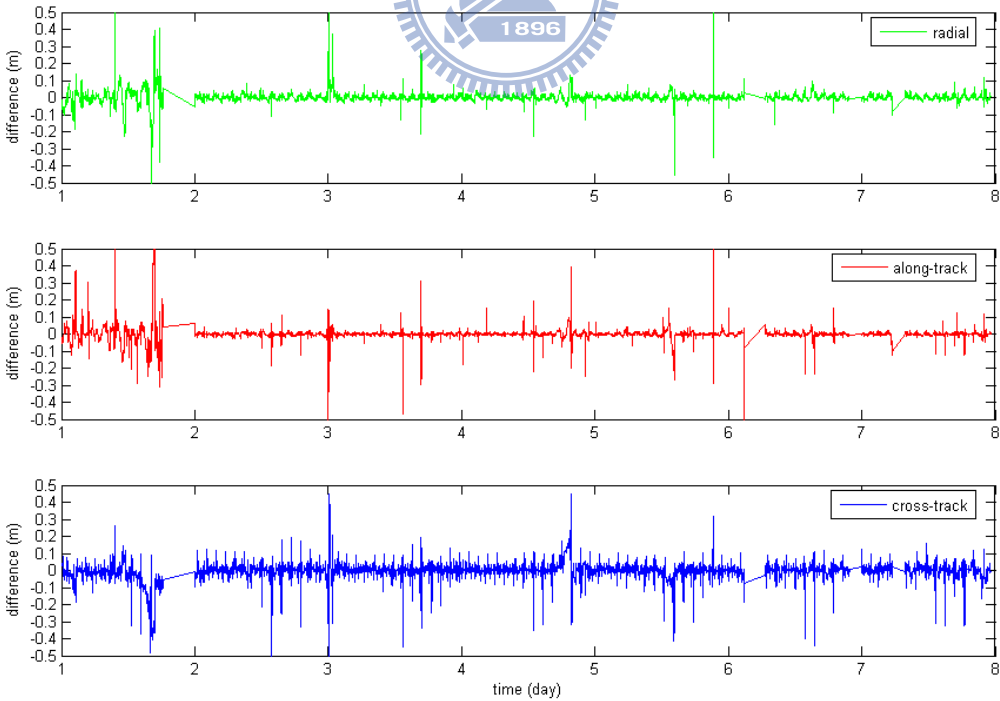


Fig. 7-2: Differences between orbits using nominal and observed attitudes, FM5,

Day 214 to 220, 2006 (Hwang et al. 2009)

107

Table 7-2: RMS overlap differences of orbits (in cm) computed with observed and
nominal attitudes, FM5, Day 214 to 220, 2006 (Hwang et al. 2009)

|  | Kinematic orbit | Dynamic orbit |
|---|---|---|
| Nominal attitude | 2.37/3.00/2.17[1] | 2.39/1.96/1.05 |
| Observed attitude | 2.35/3.00/2.17 | 3.17/2.62/1.51 |

[1]radial, along-track and cross-track

## 7.2 Data volume and β angle

As mentioned in Chapter 5, the yaw axis of F3/C varies constantly with β angle
in order to maximize the sun exposure because of the structure of the solar panel. At a
transition β angle of 0 ° the forward antenna will be rotated to backward direction
with a period of about 60 days via the yaw-fixed mode (yaw-flip). In the case of β >0
°, POD+X antenna will be the default POD antenna; for β < 0 °, the POD-X antenna
will be the default POD antenna, as shown in Fig. 7-3. Fig. 7-3 shows the data volume
of the default and non-default POD antennas for FM4 varied with β angles. Currently,
only the default antennas of both FM2 and FM4 vary with β angles but the others of
F3/C satellites always use the POD+X antenna as the default POD, regardless of β > 0
or β < 0 due to low SNR problem in POD-X antenna.
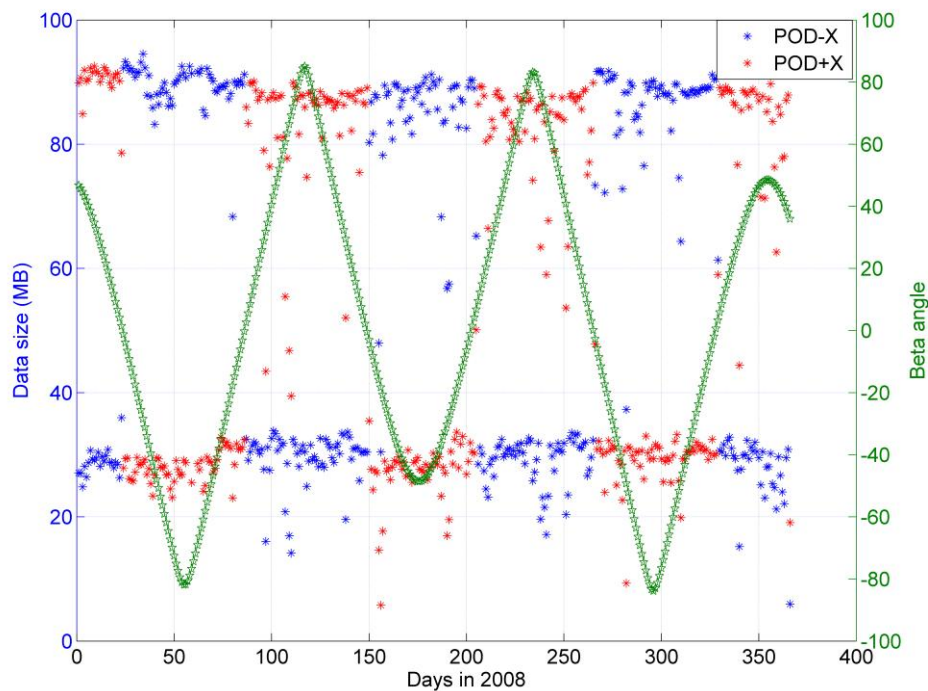
Fig. 7-3: Data volume of both POD antennas as a function of β angle for FM4

## 7.3 Phase residuals in eclipse and sun acquisition

In this section, the phase residuals in the eclipse and in the sun acquisition were assessed. The attitude is mainly measured by the magnetometer and the earth horizon sensors during the eclipsed period of about 30 minutes, and the sun sensors are involved in the attitude determination system when F3/C is off the eclipse. However, the signal from GPS is transmitted to the receiver antenna via a right-hand circular polarization (RHCP) system differing from a linear polarization system, as shown in Fig. 7-4. Thus, an effect called "phase wind-up" (Wu et al. 1993) on the carrier phase measurement will appear only if the orientation between the receiver antenna and GPS antenna is changed. An error of few centimeters in residuals caused by phase wind-up may be introduced into the position, troposphere, and clock solutions associated with the yaw error (Bar-Sever 1996), as shown in Fig. 7-5. The residuals in

the red region are associated with the variation of the yaw angle. However, such wind-up effect can be eliminated by the double-difference solution (not made in the study). Estimating receiver clock error via the least-squares adjustment can largely reduce the phase wind-up effect, but the remaining errors still exist in the residuals (see Fig. 7-5). Those outliers will be identified using the 3-sigma criterion in order to remove the attitude-error effect and will not be used in the orbit determination. If the outliers are not removed, they might destroy the final orbit solution. For the GPS orbit determination, Kouba (2009) demonstrated that the eclipsing data can be removed by the method of Bar-Sever (1996), who used a simplified yaw-attitude mode for eclipsing GPS to maintain the data continuity and improved the solution of GPS orbits.



(a)



Transmitting
direction

(b)



Transmitting
direction
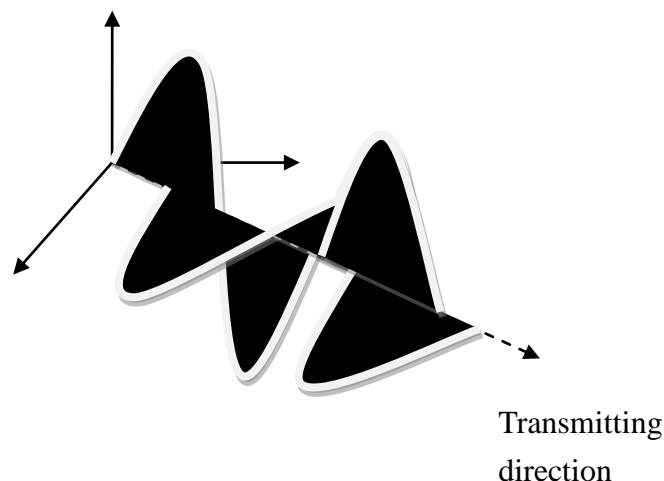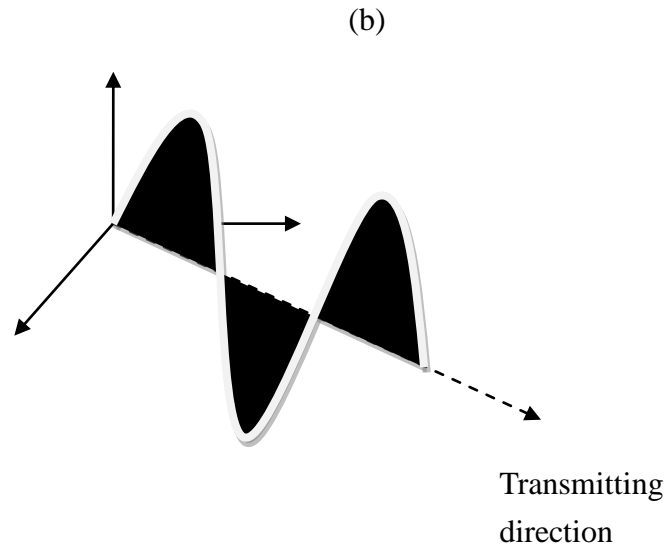
Fig. 7-4: (a) Right-hand circular polarization system and (b) linear polarization system
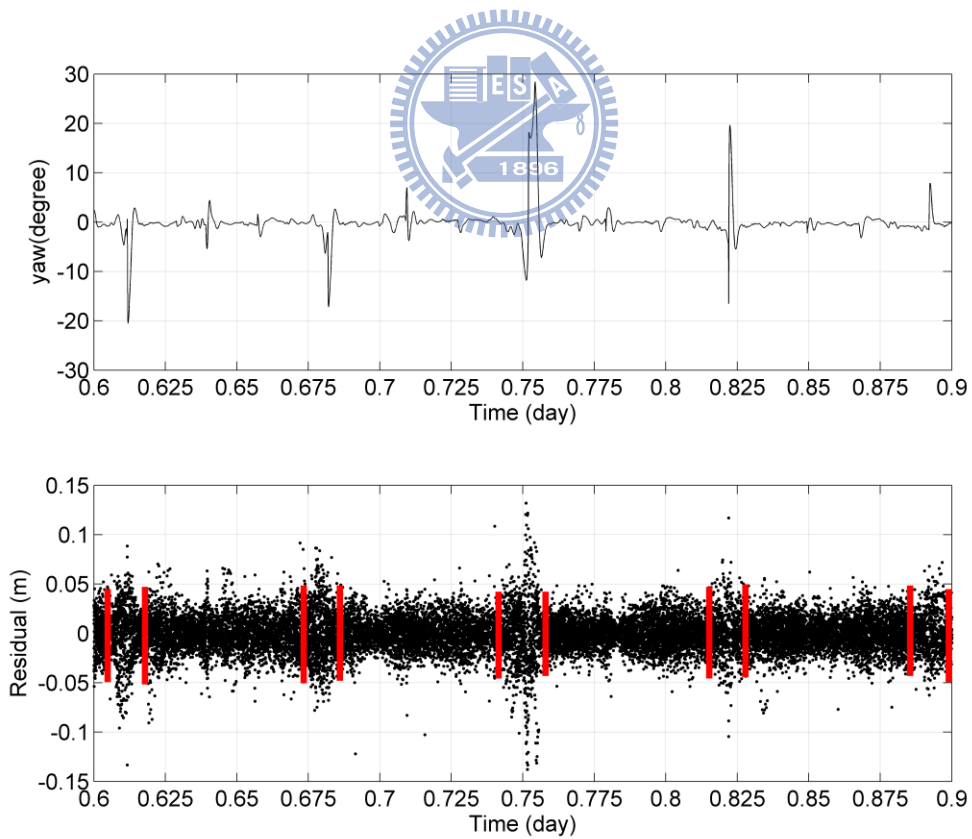


Fig. 7-5: Phase residuals associated with yaw variation for FM4 DOY 148, 2008

**7.4 Quantification of attitude error based on kinematic orbit determination**

**7.4.1 Procedure for estimating baseline between POD antenna phase center and satellite COM**

In this section, the 5-s HRC was used for the following study. Quaternion is used to transform the spacecraft coordinates from the inertial frame to satellite body frame. In Table 3-1, NSPO has determined the baseline between the POD patch antenna and the COM of F3/C to mm accuracy. In this section, we estimated the baseline length using the kinematic strategy rather than dynamic strategy due to the underlying definition of the dynamic models acting on spacecraft's COM. A procedure for estimating the baseline length is shown in Fig. 7-6. The positions in the inertial frame are estimated at both the phase center of the default antenna and the spacecraft's COM. Subsequently, the coordinate transformation from the inertial frame to the spacecraft frame was implemented using ATM (see Eq. (5.7)). Finally, the baseline vector was formed from the position difference between the antenna phase center and the spacecraft's COM. In order to assess the positioning accuracy, the estimated baseline vector was compared with that given by NSPO.

```
┌─────────────────────┐        ┌─────────────────────┐
│  PPP at default     │        │  PPP at spacecraft  │
│  antenna            │        │  COM                │
│  in inertial frame  │        │  in inertial frame  │
└─────────────────────┘        └─────────────────────┘
              ╲                    ╱
               ╲                  ╱
              ┌──────────────────┐
              │       ATM        │
              │  transformation  │
              └──────────────────┘
               ╱                  ╲
              ╱                    ╲
┌─────────────────────┐        ┌─────────────────────┐
│  Default antenna in │        │  Spacecraft COM in  │
│  spacecraft frame   │        │  spacecraft frame   │
└─────────────────────┘        └─────────────────────┘
              ╲                    ╱
               ╲                  ╱
          ┌──────────────────────────┐
          │ Difference between       │
          │ estimated-               │
          │ and given baseline       │
          │ vectors                  │
          └──────────────────────────┘
```
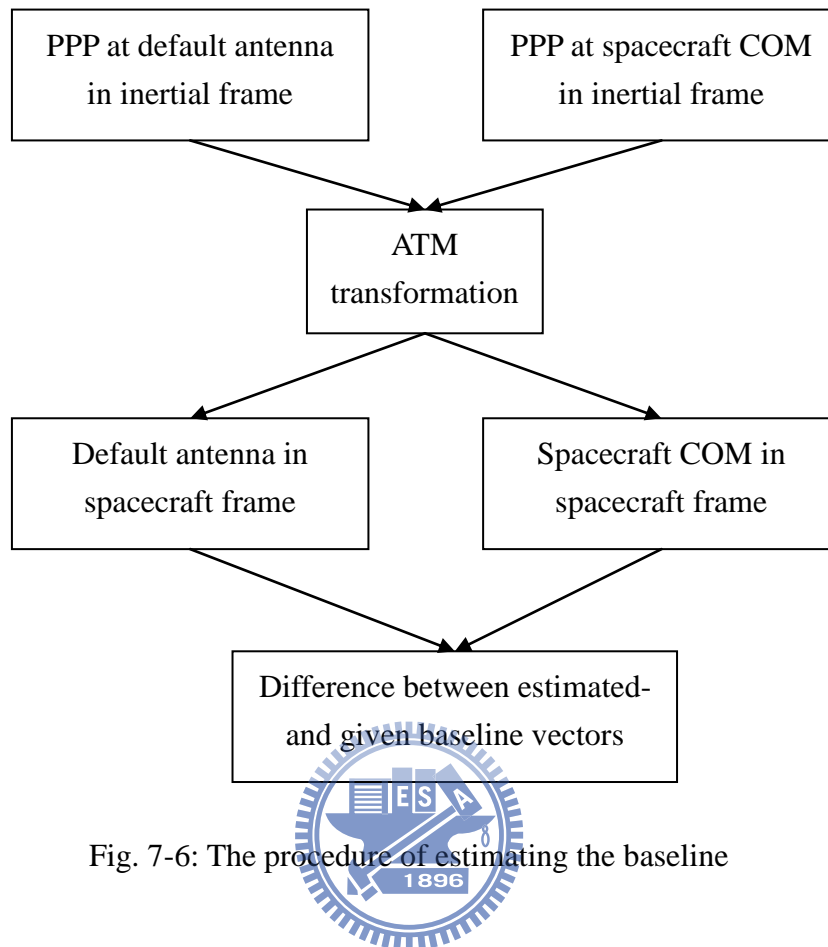
Fig. 7-6: The procedure of estimating the baseline

## 7.4.2 Quantification of attitude error

Fig. 7-7 shows the differences between estimated and given baselines in the spacecraft frame for FM3 DOY 209, 2008. Ideally, an estimated baseline should be equal to the given value, and the differences between them should approach the noise level of GPS phase measurement, which is about 1-2 mm (see the latter portion (0.4-1 day) of Fig. 7-7). If the estimated baseline is free from systematic errors, the mean value of the differences should also be zero. However, the attitude control for F3/C is not perfect due to the spacecraft weight and attitude sensor errors. As shown in 0.2 and 0.4 days in Fig. 7-7, the fluctuation of the differences is mainly associated with the inaccurate attitude determination affecting the ATM of Fig. 7-6 (also Eq. (5.7)). The means and standard deviations at different time are summarized in Table 7-3.

113

Under a stable attitude control, the standard deviations of the differences are at a few mm level and there is no significant systematic error (< 1 mm) between the estimated and given baselines for the period of 0.4-1 day. However, for the period of 0.2-0.4 day, the standard deviation values are few cm and the systematic error exceeds 1 cm, and this is due to unstable attitude control. For the period of 0.2-0.4 day, the bad attitude control may destroy the F3/C orbit accuracy because the errors are propagated into the ATM, and this is hardly observed by the orbit overlap at the same position (e.g. COM) (Hwang et al. 2009 and 2010). The ATM error is found to be about 1.5 cm in X and Y components and about 2.5 cm in Z component for FM3 DOY 209, 2008. Additionally, it is difficult to illustrate why the error in Z-component is larger than those in the other two components, as seen in Table 7-3. This might be because each coordinate axis is affected by two attitude angles from the other two axes.
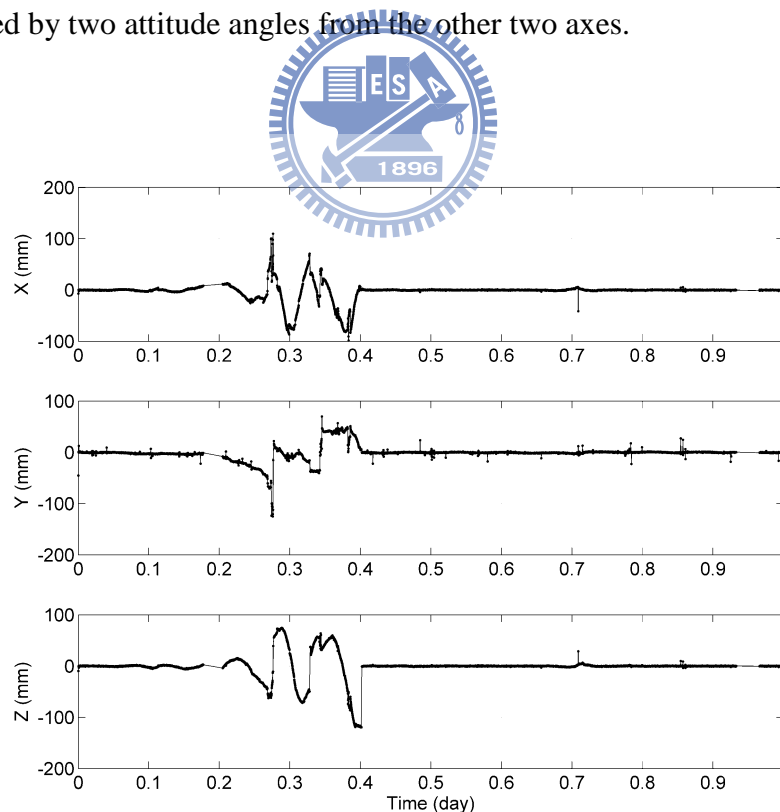


Fig. 7-7: Differences between estimated and given baselines in the spacecraft frame for FM3 DOY 209, 2008

114

Table 7-3: Mean and standard deviation (STD) of the differences between
estimated and given baseline lengths (see Fig. 7-7)

|  | 0.4-1 day (mean/STD) | 0.2-0.4 day (mean/STD) | 1 day (mean/STD) |
|---|---|---|---|
| X (mm) | -0.02/1.16 | -13.44/35.58 | -2.80/17.12 |
| Y (mm) | -0.33/1.86 | -4.62/32.10 | -1.52/14.81 |
| Z (mm) | -0.39/6.44 | -3.00/50.40 | -1.00/23.42 |

### 7.4.3 Assessment of positioning accuracy

The RMS of the differences between laboratory-determined baseline components
(by NSPO) and the estimated values can serve as an indicator of the GPS positioning
accuracy. Fig. 7-8 shows the RMS values of daily baseline difference in the spacecraft
frame for FM5 over 249 days, starting from DOY 118, 2008. The RMS values smaller
than 1 cm in each component are associated with stable attitude controls, as seen in
Fig. 5-9 (e). An internal orbit accuracy of 3 cm for F3/C satellites is reported by
Hwang et al. (2009) using the orbit-overlap approach. Based on analysis of phase
residuals and orbit overlaps, Hwang et al. (2010) reported that the quality of F3/C
GPS observations was not as good as GRACE. Therefore, the procedure in Fig. 7-6
can be used to quantify the attitude error and to assess the positioning accuracy for
F3/C satellites. A summary of the RMS values of daily baseline difference for F3/C
satellites over 249 days, since DOY 118 in 2008, is given in Table 7-4. In general, the
Y difference is larger than the X, Z differences, except for FM2. This means that the
attitudes at the roll and yaw angles are less precise or such attitude controls are less
effective, compared to the attitude at the pitch angle. From this study, the positioning

accuracy is primarily related to the attitude error, and the outcome in Table 7-4 agrees

with the accuracy assessment given in Table 5-1.
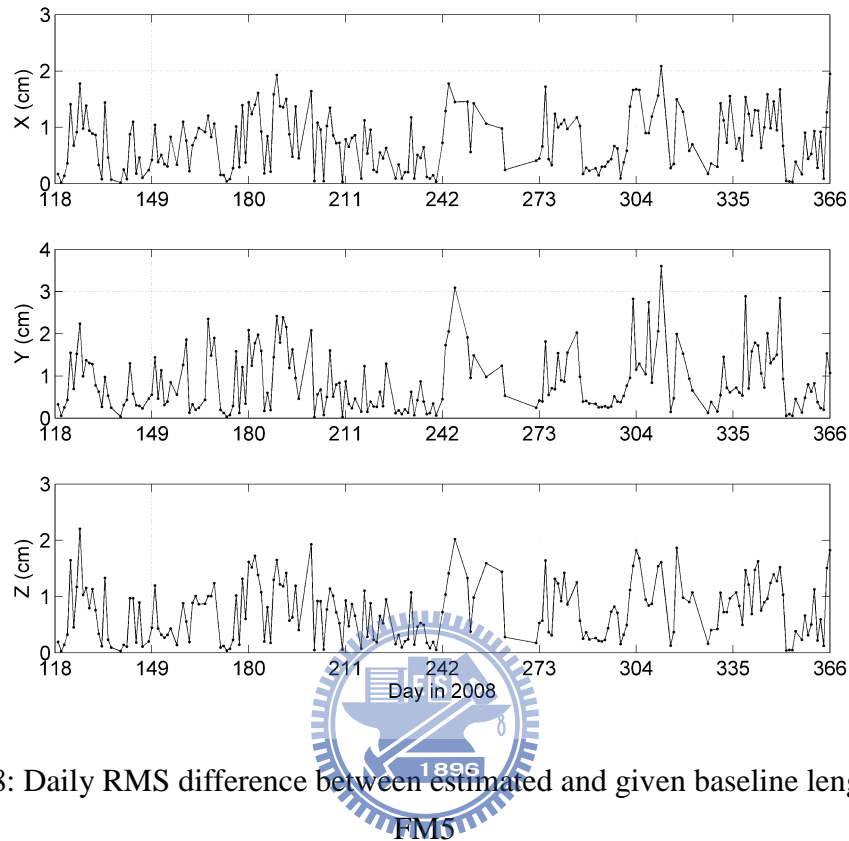


Fig. 7-8: Daily RMS difference between estimated and given baseline lengths for
FM5

Table 7-4: Average RMS difference over 249 days between estimated and given
baseline lengths

|  | X (cm) | Y (cm) | Z (cm) | Total (cm) |
| --- | --- | --- | --- | --- |
| FM1 | 1.40 | 1.83 | 1.45 | 2.72 |
| FM2 | 1.19 | 1.53 | 1.77 | 2.62 |
| FM3 | 1.31 | 1.48 | 1.30 | 2.37 |
| FM4 | 0.99 | 1.28 | 0.99 | 1.90 |
| FM5 | 0.91 | 1.12 | 0.90 | 1.70 |
| FM6 | 1.04 | 1.35 | 1.03 | 1.99 |

# Chapter 8

# Conclusions and future work

## 8.1 Conclusions

1. With selected satellites and time spans, this study analyzes the quality of GPS data from F3/C and GRACE in terms of multipath effect, the time derivative of IOD, cycle slip, phase residual, and dynamic-kinematic orbit difference. For all analyses, F3/C shows larger quality-indicator values of GPS data than GRACE, resulting in a smaller ratio of usable GPS data for POD. Large multipath effects might produce cycle slips that increase the number of estimated ambiguity parameters in the orbit determination, eventually degrading the orbit accuracy.

2. We also compared the orbit difference (dynamic–kinematic) of F3/C with GRACE in order to check the quality of F3/C GPS POD data. The kinematic orbit depends on the quality of GPS observations and the geometry of tracked GPS satellites as well as the quality of the attitude control. A good kinematic orbit may be obtained even if only 4 GPS satellites are collected by GRACE satellite, but a bad kinematic orbit may be obtained even if 5 or 6 GPS satellites are collected by F3/C.

3. The impacts of the satellite COM, attitude, and POD antenna PCV on the orbit determination was addressed using numerical examples. Because of the large amount of GPS data (6 satellites, more than two years), the numerical examples given in this study are limited, and more will be given as our computing facility improves. The orbit overlap analyses suggest that the accuracy of the reduced-dynamic and kinematic orbits is at the 2-3 cm level. It is noted that, for atmospheric occultation research using F3/C, a cm-orbit is over qualified.

4. The ATM plays an important role in the procedure of orbit determination. The

quality of ATM will affect the orbit accuracy by means of the coordinate frame transformation. For a stable attitude control, the positioning accuracy can be down to 1 or 2 mm, while for an unstable control, it can be downgraded 10 cm or more. In this study, we conclude that the orbit accuracy of F3/C satellites is governed by the attitude control and the location of POD patch antenna. Unstable attitude control is attributed to the satellite weight and the accuracy of the scientific sensors mentioned in Chapter 5.

5. F3/C's kinematic orbits can be used to enhance the GRACE-only gravity solution, especially in the low-degree gravity harmonic coefficients. The potential of F3/C GPS data for gravity research is to be explored.

6. For the orbit science in Taiwan, the main contribution of this dissertation is the accomplishment of F3/C orbit determination, the orbit assessment, and the quality check of POD data. Therefore, the best post-processing orbits of F3/C are achieved by NCTU in Taiwan.

## 8.2 Future work

1. For the improvement on the accuracy of F3/C orbits, this may be achieved by (1) combing GPS data from the two POD antennas, (2) using attitude data without outliers.

2. For the improvement on the gravity recovery using F3/C kinematic orbits, the positioning error caused by ATM cannot be involved into the algorithm of the earth gravity recovery. For this reason, the criterion of removing such error should be established.

3. The experience learnt from this analysis will help to improve the design of POD antenna in the future COSMIC-2 mission, which is under planning. For example, for COSMIC-2, it is suggested that the POD antenna should point to the zenith

direction, and the solar panels, the POD antenna and the GPS reception should be so designed that multipath effects and cycle slips are minimized.

4. For the payloads of COSMIC-2, the study suggests COSMIC-2 have to be equipped with a star camera and the weight of COSMIC-2 has to increase in order to resist the air-drag disturbance, e.g. GRACE weight.

5. For the NRT POD of COSMIC-2 using PPP, we have to overcome some problems that the limitation of collecting timely the data from IGS ground stations and a procedure of producing NRT HRC.

6. For COSMIC-2 POD, it is suggested to increase the FOV in order to enhance the GPS geometry and the channels allocated to the default antenna in the receiver should be increase.

# References

Balmino G (1994) Orbit choice and the theory of radial orbit error for altimetry. In: Sansó F and Rummel R (eds) Satellite Altimetry in Geodesy and Oceanography. Lecture Notes in earth sciences, Vol. 50, Springer, Berlin, pp. 244-317

Bar-Server YE (1996) A new model for GPS yaw-attitude. *J Geod* 70: 714-723

Beutler G, Brockmann E, Gurtner W, Hugentobler U, Mervart L, Rothacher M, Verdun A (1994) Extended orbit modeling techniques at the CODE processing center of the international GPS service for geodynamics (IGS): theory and initial results. *Manuscr Geod* 19: 367-386

Beutler G, Jäggi A, Hugentobler U, Mervart L (2006) Efficient satellite orbit modeling using pseudo-stochastic parameters. *J Geod* 80: 353-372, doi 10.1007/s00190-006-0072-6

Bock H (2003) Efficient Methods for Determining Precise Orbits of Low Earth Orbiters Using the Global Positioning System. Geodätisch-geophysikalische Arbeiten in der Schweiz, Band 65, Schweizerische Geodätische Kommission, Institut für Geodäsie und Photogrammetrie, Eidg. Technische Hochschule Zürich, Zürich

Bock H, Dach R, Hugentobler U, Schaer S, Beutler G (2004) CODE High-rate GPS Satellite Clock Corrections. IGS Workshop, Bern, Switzerland, March 1-5

Bock H, Dach R, Jäggi A, Beutler G (2009a) High-rate GPS clock correction from CODE: support of 1Hz applications. *J Geod*, doi 10.1007/s00190-009-0326-1

Bock H, Dach R, Yoon Y, Montenbruck O (2009b) GPS clock correction estimation for near real-time orbit determination applications. *Aerosp Sci Technol* 13: 415-422, doi: 10.1016/j.ast.2009.08.003

Bock H, Hugentobler U, Springer TA, Beulter G (2002) Efficient precise orbit

determination of LEO satellites using GPS. *Adv Space Res* 30:295-300, doi: 10.1016/S0273-1177(02)00298-3

Bock H, Jäggi A, Švehla D, Beutler G, Hugentobler U, Visser P (2007) Precise orbit determination for the GOCE satellite using GPS. *Adv Space Res*, doi:10.1016/j.asr.2007.02.053

Chao BF, Pavlis EC, Hwang C, Liu CC, Shum CK, Tseng CL, Yang M (2000) COSMIC: geodetic applications in improving earth's gravity model. *Terr Atm Ocean Sci* 11: 365-378

Coker C, Dymond KF, Budzien SA, (2002) Using the Tiny Ionospheric Photometer (TIP) on the COSMIC Satellites to Characterize the Ionosphere. American Geophysical Union, Fall Meeting, abstract #SA52A-0389

Colombo O (1984) Altimetry, Orbits and Tides. NASA TM 86180, Greenbelt, Maryland

Comp CJ, Axelrad P (1998) Adaptive SNR-Based Carrier Phase Multipath Mitigation Technique. *IEEE Trans. Aerosp Electron Syst* 34: 264-276

Dach R, Hugentobler U, Fridez P, Meindl M (2007) Bernese GPS Software - Version 5.0. Astronomical Institute. University of Bern, Switzerland

Dickman J, Zhu Z, Bartone C (2009) Carrier phase multipath error characterization and reduction in signal aircraft relative positioning. *GPS Solut* 14: 141-152, doi: 10.1007/s10291-009-0126-3

Ditmar P, Kuznetsov V, van der Sluijs AAV, Schrama E, Klees R (2006) DEOS_CHAMP-01C_70: a model of the Earth's gravity field computed from accelerations of the CHAMP satellite. *J Geod* 79: 586-601

Estey LH, Meerten CM (1999) TEQC: the multi-purpose toolkit for GPS/GLONASS data. *GPS Solut* 3(1): 42-49

Fong CJ, Yang SK, Chu CH, Huang CY, Yeh JJ, Lin CT, Kuo TC, Liu TY, Yen NL,

Chen SS, Kuo YH, Liou YA, Chi S (2008) FORMOSAT-3/COSMIC Constellation Spacecraft System Performance: After One Year in Orbit. *IEEE Trans Geosci Remote Sens* 46: 3380-3394

Gerlach Ch, Földvary L, Švehla D, Gruber Th, Wermuth M, Sneeuw N, Frommknecht B, Oberndorfer H, Peters Th, Rothacher M, Rummel R, Steigenberger P (2003) A CHAMP-only gravity field model from kinematic orbits using the energy integral. *Geophys. Res. Lett.* 30 (20) 10.1029/2003GL018025.

Gurtner W, (1994) RINEX: The receiver-independent exchange format. *GPS World* 4: 48-52

Hauschild A, Montenbruck O (2009) Kalman-filter-based GPS clock estimation for near real-time positioning. *GPS Solut* 13: 173-182, doi: 10.1007/s10291-008-0110-3

Hofmann-Wellenhof B, Lichtenegger H, Collins J (2001) Global Positioning System: Theory and Practice. Springer Wien New York, ISBN 3-211-83472-9

Hughes PC (1986) Spacecraft attitude dynamics. John Wiley & Sons, Singapore

Hwang C (2001) Gravity recovery using COSMIC GPS data: application of orbital perturbation theory. *J Geod* 75:117-136

Hwang C, Lin TJ, Tseng TP, Chao BF (2008) Modeling orbit dynamics of FORMOSAT-3/COSMIC satellites for recovery of temporal gravity variations. *IEEE Trans. Geosci Remote Sens* 46: 3412-3423

Hwang C, Tseng TP, Lin T, Švehla D, Schreiner B (2009) Precise orbit determination for the FORMOSAT-3/COSMIC satellite mission GPS. *J Geod* 83: 477-489, DOI 10.1007/s00190-008-0256-3

Hwang C, Tseng TP, Lin T, Švehla D, Hugentobler U, Chao BF (2010) Quality assessment of FORMOSAT-3/COSMIC and GRACE GPS observables: analysis of multipath, ionospheric delay and phase residual in orbit determination. *GPS*

*Solut* 14 (1): 121-131, doi 10.1007/s10291-009-0145-0

IGSCB (2004) IGS products; URL http://igscb.jpl.nasa.gov/components/prods.html

Jäggi A, Dach R, Montenbruck O, Hugentobler U, Bock H, Beulter G (2009) Phase center modeling for LEO GPS receiver antenna and its impact on preceise orbit determination. *J Geod* 83:1145-1162, doi 10.1007/s00190-009-0333-2

Jäggi A, Hugentobler U, Beutler G (2006) Pseudo-stochastic orbit modeling techniques for low Earth orbiters. *J Geod* 80: 47-60, DOI 10.1007/s00190-006-0029-9

Jäggi A, Hugentobler U, Bock H, Beutler G (2007) Precise orbit determination for GRACE using undifference or doubly differenced GPS data. *Adv Space Res* 39 (10): 1612-1619, doi 10.1016/j.asr.2007.03.012

Jan YW (2003) Attitude Determination and Control System Design for Micro/Small Satellite. Ph.D. dissertation for Department of Electrical and Control Engineering, National Chiao Tung University, Taiwan

Jan YW, Tsai JR (2005) Active control for initial attitude acquisition using magnetic torquers. *Acta Astronaut* 57: 754-759, doi: 10.1016/j.actaastro.2005.03.067

Kang Z, Tapley B, Bettadpur S, Ries J, Nagel P, Pastor R, (2006) Precise orbit determination for the GRACE mission using only GPS data, *J Geod* 80: 322–331, DOI 10.1007/s00190-006-0073-5

König R, Michalak G, Neymayer KH, Zhu SY (2006) Remarks on CHAMP orbit products. In: Flury J, Rummel R, Reigber C, Rothacher M, Boedecker G, Schreiber U (eds), Observation of the Earth System From Space, pp. 17-26, Springer, Berlin

Koch KR (1987) Parameter Estimation and Hypothesis testing in Linear Models, Springer, Berlin

Kouba J (2002) A guide to using international GPS service (IGS) products. URL

http://igscb.jpl.nasa.gov/components/IGSProducts_user_v17.pdf

Kouba J (2009) A simplified yaw-attitude model for eclipsing GPS satellites, *GPS Solut* 13:1-12, doi 10.1007/s10291-008-0092-1

Lee LC, Rocken C, and Kursinki ER (2000) Special issue for applications of the Constellation Observing System for Meterology, Ionosphere and Climate (COSMIC). *Terr Atmos Ocean Sci* 11 (1)

Leick A, (2004) GPS satellite surveying. Third edition, John Wiley & Sons, Inc., Hoboken, New Jersey

Liu JN, Ge MR (2003) PANDA software and its preliminary result for positioning and orbit determination. The fourth international symposium on GPS/GNSS, Nov. 6-8, 2002, WHU, P.R. China

Long AC, Cappellari JO, Velex CE, Fuchs AJ (eds) (1989) Goddard Trajectory Determination System Mathematical Theory, Revision 1, FDD/552-89/001

Mayer-Gürr, T, Ilk, KH, Eicker, A, Feuchtinger, M (2005) ITG-CHAMP01: A CHAMP Gravity Field Model from Short Kinematical Arcs of a One-Year Observation Period, *J Geod* 78: 462-480, Springer-Verlag

Montenbruck O, Garcia-Fernandez M, Williams J (2006) Performance comparison of semicodeless GPS receivers for LEO satellites. *GPS Solut* 10: 249–261,doi 10.1007/s10291-006-0025-9

Montenbruck O, Garcia-Fernandez M, Yoon Y, Schön S, Jäggi A (2009) Antenna phase center calibration for precise positioning of LEO satellites. *GPS Solut* 13:23-34, doi 10.1007/s10291-008-0094-z

Montenbruck O, Gill E, Kroes R (2005) Rapid orbit determination of LEO satellites using IGS clock and ephemeris products. *GPS Solut* 9: 226-235, doi 10.1007/s10291-005-0131-0

Montenbruck O, Kroes R (2003) In-flight performance analysis of the CHAMP

BlackJack GPS Receiver. *GPS Solut* 7: 74-86, doi: 10.1007/s10291-003-0055-5

Neumayer K-H, Michalak G, König R (2005) On calibrating the CHAMP on-board accelerometer and attitude quaternion processing - In: Reigber Ch, Lühr H, Schwintzer P, Wickert J, (Eds.), Earth observation with CHAMP: Results from Three Years in Orbit, pp. 71-76, Springer, Germany

Ogaja C, Hedfors J, (2007) TEQC multipath metrics in MATLAB. *GPS Solut* 11: 215-222, DOI 10.1007/s10291-006-0052-6

Reigber C, Bock R, Förste C, Grunwaldt L, Jakowski N, Lühr H, Schwintzer P, Tilgner C (1996) CHAMP phase B-executive summary; Scientific technical report STR96/13, GeoForschungsZentrum Potsdam

Reubelt T, Austen G, Grafarend EW (2004) Harmonic analysis of the Earth's gravitational field by means of semi-continuous ephemerides of a low Earth orbiting GPS-tracked satellite. Case study: CHAMP. *J Geod* 77(5-6), 257-278, DOI10.1007/s00190-003-0322-9

Schmid R, Rothacher M, Thaller D, Steigenberger P (2005) Absolute phase center corrections of satellite and receiver antennas impact on global GPS solutions and estimation of azimuthal phase center variations of the satellite antenna. *GPS Solut* 9(4):283–293, doi: 10.1007/s10291-005-0134-x

Schmid R, Steigenberger P, Gendt G, Ge M, Rothacher M (2007) generation of a consistent absolute phase center correction model for GPS receiver and satellite antennas. *J Geod* 81(12):781–798, doi: 10.1007/s00190-007-0148-y

Schreiner B, (2005) COSMIC GPS POD and Limb Antenna Test Report. Internal report of UCAR

Schreiner W, Rocken C, Sokolovskiy S, Hunt D (2010) Quality assessment of COSMIC/FORMOSAT-3 GPS radio occultation data derived from single- and double-differnece atmospheric excess phase processing. *GPS Solut* 14 (1): 13-

22, doi: 10.1007/s10291-009-0132-5

Seeber G (2003) Satellite Geodesy. 2nd ed, de Gruyter, Berlin

Švehla D, Rothacher M (2005a) Kinematic Precise Orbit Determination for Gravity Field Determination.  IUGG General Assembly 2003, June 30 – July 11 2003, Sapporo, Japan. The Proceedings of the International Association of Geodesy: A Window on the Future of Geodesy. Eds. F. Sanso. Spriger Verlag, IAG Vol 128. pp 181-188

Švehla D, Rothacher M (2005b) Kinematic positioning of LEO and GPS satellites and IGS stations on the ground. *Adv Space Res* 36: 376-381. doi:10.1016/j.asr.2005.04.066

Švehla D, Rothacher M (2006) Can the reference system be defined based on the LEO/GPS bi-constellation? Paper presented at the 36th COSPAR Scientific Assembly, 16-23 July 2006, Beijing, China

Švehla D, Rothacher M, (2004) CHAMP and GRACE in Tandem: POD with GPS and K-Band Measurements. Joint CHAMP/GRACE Science Meeting, 6–8 July 2004, GeoForschungsCentrum Potsdam, Germany

Švehla D, Rothacher M (2003) Kinematic and Reduced–Dynamic Precise Orbit Determination of Low Earth Orbiters. *Adv Geosci* 1: 47-56

Syndergaard S, Schreiner WS, Rocken C, Hunt DC, Dymond KF, (2006) Preparing for COSMIC: Inversion and Analysis of Ionospheric Data Products. Atmosphere and Climate, doi 10.1007/3-540-34121-8_12

Tapley B, Ries J, Bettapur S, Chamber D, Cheng M, Condi F, Guenter B, Kang Z, Nagel P, Pastor R, Pekker T, Poole, Wang F (2005) GGM02-An improved Earth gravity field model from GRACE. *J Geod* 79:467-478

Visser PNAM, Van den IJssel J (2000) GPS-based precise orbit determination for the very low Earth-orbiting gravity mission GOCE. *J Geod* 74: 590-602

Warren DLM, Raquet JF (2003) Broadcast vs. Precise GPS ephemerides: a historical perspective. *GPS Solut* 7: 151-156, doi:10.1007/s10291-003-0065-3

Wertz JR (1991) Spacecraft Determination and Control. Kluwer Academic Publishers, Boston

Wu BH, Fu CL, Liou YA, Chen WJ, Pan HP (2005) Quantitative analysis of the errors associated with orbit uncertainty for FORMOSAT-3. Proc. of Int. Sym Remote Sensing (ISRS), October 12-14, 2005, Korea, pp. 87-90

Wu JT, Wu SC, Hajj GA, Bertiger WI, Lichten SM (1993) Effect of antenna orientation on GPS carrier phase. *Manuscr Geod* 18: 91-98

Zumberge, JF, Gendt G (2001), The demise of selective availability and implications for the International GPS Service. *Phys Chem Earth Part A* 26(6–8): 637–644

# Curriculum Vitae

**Position:**

Department of Civil Engineering

National Chiao Tung University

1001 Ta Hsueh Road, Hsinchu 300

Taiwan

Phone: +886-3-5712121 ext 54990

Fax: +886-3-5716257

E-Mail: tzupang.cv95g@g2.nctu.edu.tw

WWW: http://space.cv.nctu.edu.tw


**Date of Birth:** December 27, 1980
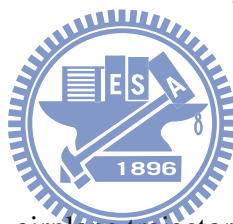
**Place of Birth:** Tainan county, Taiwan


**Education:**

BS, Dept of Surveying Engineering, National Cheng Kung University, June 2004.

MS, Dept of Civil Engineering, National Chiao Tung University, July 2006.


**Research Topic:**

- Satellite Geodesy
- GPS Data Processing
- Kinematic Positioning(e.g. airplane trajectory & ship trajectory)
- Precise orbit determination for LEO


**Experience:**

My visit to TUM (Technical University of Munich) in 2005 and 2008 for FORMOSAT-3/COSMIC satellite mission

My visit to OSU (The Ohio State University) in 2009 for FORMOSAT-3/COSMIC satellite mission


**Publication:**

**Journal papers**

Hwang C, Tseng TP, Lin TJ, Fu CL, Švehla D (2006) Precise orbit determination for FORMOSAT-3/COSMIC and gravity application. Chinese Journal of Physics 28(6): 924-933 (in Chinese)

Hwang C, Lin TJ, Tseng TP, Chao BF (2008) Modeling orbit dynamics of FORMOSAT-3/COSMIC satellites for recovery of temporal gravity variations. IEEE Transaction on Geoscience and Remote Sensing 46: 3412-3423

Hwang C, Tseng TP, Lin T, Švehla D, Schreiner B (2009) Precise orbit determination for the FORMOSAT-3/COSMIC satellite mission GPS. Journal of Geodesy 83: 477-489, DOI 10.1007/s00190-008-0256-3

Hwang C, Tseng TP, Lin T, Švehla D, Hugentobler U, Chao BF (2010) Quality assessment of FORMOSAT-3/COSMIC and GRACE GPS observables: analysis of multipath, ionospheric delay and phase residual in orbit determination. GPS Solutions 14: 121-131, DOI 10.1007/s10291-009-0145-0

**Conference papers**

1. Hwang C, Tseng TP, Lin TJ, Fu CL, Švehla D (2006) Precise Orbit Determination For FORMOSAT-3/COSMIC And Gravity Application, Fall Meeting, American Geophysical Union, San Francisco, December 11-15

2. Hwang C, Lin TL, Tseng TP (2007) Recovery and analysis of earth's gravity field using FORMOSAT-3/COSMIC GPS data, IUGG XXIV General Assembly, Perugia, Italy, July 2- July 13

3. Tseng TP, Hwang C (2007) Precise GPS baseline solutions for the tandem satellites of FORMOSAT-3/COSMIC, Fall Meeting, American Geophysical Union, San Francisco, December 10-14

4. Tseng TP, Hwang C, Lin T, Švehla D, Hugentobler U, Chao BF (2009) Precise orbit determination and quality assessment of GPS observables for FORMOSAT-3/COSMIC and GRACE missions, FORMOSAT-3/COSMIC workshop, Boulder Colorado, October 27-29

5. Lin TJ, Hwang C, Tseng TP (2006) Temporal gravity field recovery using FORMOSAT-3/COSMIC kinematic orbit data. Workshop 2006, Taipei

6. Tseng TP, Hwang C (2006) Orbit determination of FORMOSAT-3/COSMIC: analysis of orbit accuracy and problem. Proceedings of the 25th Conference on Surveying, Taiwan

**Technical report**

Hwang C, Lin TJ, Tseng TP, Tangdamrongsub N (2008-2010) Precise orbit determination and analysis of Earth's gravity field using COSMIC GPS data, Report of GPS Science and Application Research Center 3-year Program